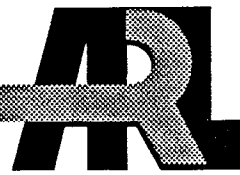
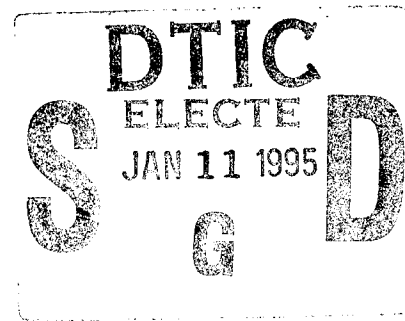


ARMY RESEARCH LABORATORY



# An Optoelectronic Attenuator for the High-Speed Control of Microwave Integrated Circuits

by Stephen E. Saddow  
*Army Research Laboratory*  
and  
Chi H. Lee  
*University of Maryland*



ARL-TR-387

November 1994

19950109 004

Approved for public release; distribution unlimited.

The findings in this report are not to be construed as an official Department of the Army position unless so designated by other authorized documents.

Citation of manufacturer's or trade names does not constitute an official endorsement or approval of the use thereof.

Destroy this report when it is no longer needed. Do not return it to the originator.

REPORT DOCUMENTATION PAGE			Form Approved OMB No. 0704-0188
<p>Public reporting burden for this collection of information is estimated to average 1 hour per response, including the time for reviewing instructions, searching existing data sources, gathering and maintaining the data needed, and completing and reviewing the collection of information. Send comments regarding this burden estimate or any other aspect of this collection of information, including suggestions for reducing this burden, to Washington Headquarters Services, Directorate for Information Operations and Reports, 1215 Jefferson Davis Highway, Suite 1204, Arlington, VA 22202-4302, and to the Office of Management and Budget, Paperwork Reduction Project (0704-0188), Washington, DC 20503.</p>			
1. AGENCY USE ONLY (Leave blank)	2. REPORT DATE	3. REPORT TYPE AND DATES COVERED	
	November 1994	Final, Nov 90 to Dec 93	
4. TITLE AND SUBTITLE  An Optoelectronic Attenuator for the High-Speed Control of Microwave Integrated Circuits			5. FUNDING NUMBERS  PE: 61102
6. AUTHOR(S)  Stephen E. Saddow (ARL) and Chi H. Lee (UMCP)			
7. PERFORMING ORGANIZATION NAME(S) AND ADDRESS(ES)  U.S. Army Research Laboratory Attn: AMSRL-WT-NF 2800 Powder Mill Road Adelphi, MD 20783-1197			8. PERFORMING ORGANIZATION REPORT NUMBER  ARL-TR-387
9. SPONSORING/MONITORING AGENCY NAME(S) AND ADDRESS(ES)  U.S. Army Research Laboratory Attn: AMSRL-WT-NA 2800 Powder Mill Road Adelphi, MD 20783-1197			10. SPONSORING/MONITORING AGENCY REPORT NUMBER
11. SUPPLEMENTARY NOTES  AMS code: 611102.H440011 ARL Proj: 4AE125			
12a. DISTRIBUTION/AVAILABILITY STATEMENT  Approved for public release; distribution unlimited.		12b. DISTRIBUTION CODE	
13. ABSTRACT (Maximum 200 words)  An optoelectronic attenuator suitable for the optical control of microwave integrated circuits is presented. High-speed photoconductive switches are embedded in planar microwave transmission lines, and semiconductor laser diodes (LDs) are used to control the microwave signal level on these high-speed lines. With a silicon coplanar waveguide-photoconductive switch (Si:CPW-PCS), up to 45 dB of microwave attenuation has been achieved with a fiber-pigtailed laser diode having 144 mW of optical power. Measurements made using a vector network analyzer show that the attenuator performance can be explained by a classical plasma absorption argument, whereby the microwave signal is attenuated by the optically induced solid-state plasma.			
<p>Edge-coupled Fabry-Perot aluminum-gallium-arsenide/gallium-arsenide (AlGaAs/GaAs) semiconductor LDs, as well as both silicon and gallium-arsenide (GaAs) CPW-PCSs, were developed for the optoelectronic attenuator. When conventional gain-switching techniques are used, LD peak output powers greater than 1 W have been demonstrated, and when an optical Q-switching scheme is used, 6 W of peak power has been achieved in tens of picoseconds.</p>			
14. SUBJECT TERMS  Attenuator, optoelectronic, high-speed photo-conductive switch			15. NUMBER OF PAGES 83
			16. PRICE CODE
17. SECURITY CLASSIFICATION OF REPORT Unclassified	18. SECURITY CLASSIFICATION OF THIS PAGE Unclassified	19. SECURITY CLASSIFICATION OF ABSTRACT Unclassified	20. LIMITATION OF ABSTRACT UL

# Contents

<b>1. Introduction .....</b>	<b>7</b>
1.1 <i>Overview .....</i>	<i>7</i>
1.2 <i>Objectives of the Research .....</i>	<i>9</i>
<b>2. Microwave Optoelectronic Attenuator Scheme .....</b>	<b>11</b>
2.1 <i>Optoelectronic Attenuator Motivation .....</i>	<i>12</i>
2.2 <i>Reflective Optoelectronic Attenuator Scheme .....</i>	<i>15</i>
2.3 <i>Absorptive Optoelectronic Attenuator Scheme .....</i>	<i>19</i>
2.4 <i>Summary .....</i>	<i>24</i>
<b>3. Laser Diode Development .....</b>	<b>26</b>
3.1 <i>Multi-Section Quantum-Well Laser Diodes .....</i>	<i>27</i>
3.2 <i>Laser Diode Design, Fabrication, and Performance .....</i>	<i>32</i>
3.3 <i>Optically Q-Switched Two-Section Laser Diode Experiment .....</i>	<i>36</i>
3.4 <i>Laser Diode Microwave Impedance-Matching Transformer .....</i>	<i>40</i>
3.5 <i>Summary .....</i>	<i>43</i>
<b>4. Photoconductive Switches .....</b>	<b>44</b>
4.1 <i>Photoconductive Switch Physics .....</i>	<i>44</i>
4.2 <i>Planar Microwave Transmission Lines .....</i>	<i>47</i>
4.3 <i>CPW-PCS Design, Fabrication, and Evaluation .....</i>	<i>49</i>
4.4 <i>CPW-PCS Electrical and Optical Characterization .....</i>	<i>50</i>
4.5 <i>Summary .....</i>	<i>51</i>
<b>5. Optoelectronic Attenuator Experiments .....</b>	<b>54</b>
5.1 <i>Nd:Glass Laser Measurements .....</i>	<i>55</i>
5.2 <i>Broad-Area Laser Diode Measurements .....</i>	<i>57</i>
5.3 <i>Fiber-Pigtailed LD Experiments—rf Voltage Measurements .....</i>	<i>60</i>
5.4 <i>Fiber-Pigtailed LD Experiments—VNA Measurements .....</i>	<i>63</i>
5.5 <i>Summary .....</i>	<i>67</i>
<b>6. Summary and Conclusions .....</b>	<b>68</b>
<b>Acknowledgements .....</b>	<b>70</b>
<b>References .....</b>	<b>71</b>
<b>Distribution .....</b>	<b>81</b>

# Figures

1. Diagram of proposed hybrid optoelectronic attenuator scheme .....	10
2. Hybrid reflective optoelectronic attenuator schematic .....	17
3. Two-port model of loss-less transmission line with embedded shunt resistance ..	17
4. Reflective optoelectronic attenuator theoretical prediction for attenuation .....	18
5. Hybrid “absorptive” optoelectronic attenuator .....	20

6. Theoretical prediction for attenuation, $S_{21}$ , versus solid-state plasma density .....	23
7. Theoretical prediction for attenuation, $S_{21}$ , versus laser diode power .....	24
8. GRINSCH LD device material structure .....	28
9. LD performance as function of quantum well number .....	29
10. LD device fabricated using material structure of figure 8 .....	30
11. Two-section LD geometry .....	31
12. Theoretical two-section LD $L/I$ curve .....	32
13. Cleaved bar showing four 150- $\mu\text{m}$ -stripe one-section broad-area LDs .....	33
14. Cleaved bar showing two ridge-waveguide LDs .....	33
15. One-section 500- $\mu\text{m}$ broad-area pulsed $L/I$ curve. LD operation is in pulsed mode .....	33
16. Corresponding spectral output of figure 15 .....	34
17. $L/I$ curve of two-section 300- $\mu\text{m}$ -stripe LD versus $V_2$ .....	34
18. Image of 150- $\mu\text{m}$ -wide broad-area LD output on front facet showing fairly uniform lateral optical emission with some lateral mode structure .....	35
19. Photograph of mounted 500- $\mu\text{m}$ broad-area LD .....	35
20. Optical Q-switching experimental setup .....	37
21. Type A broad-area laser experimental and theoretical Q-switched pulse output .....	38
22. Type B broad-area laser experimental and theoretical Q-switched pulse output .....	38
23. LDMT electrical schematic generated by Academy .....	41
24. LDMT microstrip layout generated by Academy .....	41
25. Academy prediction of reflected power .....	41
26. Measured $S_{11}$ of LDMT and 50- $\Omega$ reference line terminated with broad-area LD .....	42
27. Measured $L/I$ curve using LDMT and 50- $\Omega$ reference line to drive same LD .....	43
28. Comparison between microstrip line and CPW .....	48
29. Schematic view of Si:CPW-PCS .....	50
30. Mounted GaAs and Si:CPW-PCS devices .....	50
31. Measured dark $S_{21}$ of Si:CPW-PCs .....	51
32. Experimental setup used to measure CPW-PCS PC carrier lifetime .....	52
33. Measured PC carrier lifetime .....	52
34. Nd:glass laser experimental setup used to measure $S_{21}$ of hybrid optoelectronic attenuator .....	56
35. Optoelectronic attenuator data taken with Nd:glass laser system .....	56
36. Optoelectronic attenuator data with 300- $\mu\text{m}$ broad-area LD .....	57
37. Measured attenuation versus incident LD power using 300- $\mu\text{m}$ broad-area LD .....	58
38. 1-cm LD array optoelectronic attenuator data showing 500-MHz signal envelope during laser activation .....	59
39. Measured attenuation versus incident LD power using 1-cm LD array .....	59
40. Measured attenuation versus rf power using 1-cm LD array .....	60

41. Fiber-pigtailed LD experimental setup used to measure $S_{21}$ of hybrid optoelectronic attenuator.....	61
42. Measured attenuation versus incident LD power with fiber-pigtailed LD .....	61
43. Theoretical and experimental comparison for reflective attenuation mechanism .....	63
44. VNA optoelectronic attenuator data with fiber-pigtailed LD (cw mode). $A_{spot} = 10 \mu\text{m} \times 10 \mu\text{m}$ .....	64
45. VNA optoelectronic attenuator data with fiber-pigtailed LD (cw mode). Measure of reflected power is $S_{11}$ .....	64
46. VNA measured attenuation at 500 MHz versus incident LD power with fiber-pigtailed LD .....	65
47. VNA optoelectronic attenuator data with fiber-pigtailed LD (cw mode). $A_{spot} = 10 \mu\text{m} \times 2.5 \text{ mm}$ .....	65
48. VNA optoelectronic attenuator data with fiber-pigtailed LD (cw mode). $A_{spot} = 10 \mu\text{m} \times 3.5 \text{ mm}$ .....	66
49. VNA optoelectronic attenuator data with fiber-pigtailed LD (cw mode). $A_{spot} = 10 \mu\text{m} \times 3.5 \text{ mm}$ , LD power = 143 mW .....	66

## Table

1. MBE 330 SQW GRINSCH laser structure .....	28
--	----

Accesion For	
NTIS CRA&I	<input checked="" type="checkbox"/>
DTIC TAB	<input type="checkbox"/>
Unannounced	<input type="checkbox"/>
Justification _____	
By _____	
Distribution / _____	
Availability Codes	
Dist	Avail and / or Special
A-1	



# 1. Introduction

## 1.1 Overview

Since the discovery of picosecond photoconductivity by Jayaraman and Lee in 1972 [1], the combination of microwave and ultra-fast optical technologies has advanced significantly [2,3]. Optoelectronic integrated circuits (OEICs) continue to make impressive strides [4,5], while the development of monolithic microwave integrated circuits (MMICs) [6] has now progressed to the point that MMICs are being placed into both commercial and military systems [7,8]. The integration of these two technologies to perform high-speed microwave systems functions is seen by some to represent the next generation of electronic integrated circuits [9]. In fact, a new integrated circuit device nomenclature for such a technology has been suggested by Simons [10]; Simons refers to these circuits with combined MMIC and OEIC components as optical monolithic microwave integrated circuits (OMMICs).

The advantages of MMICs for microwave systems use are numerous, especially at millimeter-wave (MMW) frequencies, where traditional microwave techniques are impractical. For example, the large-scale integration of microwave subsystems using MMICs allows the MMIC to be placed directly on the antenna substrate, thus reducing the need for intervening connections and thereby reducing system complexity and cost. For less ambitious systems, such as automobile collision avoidance sensors [11], MMICs can provide much higher reliability at a greatly reduced cost, since all components are monolithically integrated onto a single substrate and the problems associated with wiring together discrete components are eliminated.

MMIC fabrication uses the same technology that is used to fabricate high-speed OEICs. For example, aluminum-gallium-arsenide/gallium arsenide (AlGaAs/GaAs) heterostructures are employed to make active microwave devices, such as high-electron mobility transistors (HEMTs) [12–14] and heterostructure bipolar transistors (HBTs) [15]; in OEICs, AlGaAs/GaAs quantum wells are employed to form the active regions of laser diodes, optical waveguides, and photodetectors [16]. Thus, OEIC and MMIC circuit topologies can, in principle, be made together on the same substrate to form very-high-speed circuits. Even the basic building block of most MMIC designs, the metal semiconductor field-effect transistor (MESFET), has been controlled optically [17], as has the Gunn diode [18]. This technology has made some modest success in recent years and all indications are that even higher levels of system integration will be achieved in the near future [19].

As further evidence of the microwave potential of optoelectronic devices, laser diodes with relaxation frequencies up to 30 GHz [20], photodetectors with bandwidths on the order of 100 GHz [21], and electro-optic intensity modulators with bandwidths of 6 GHz [22] and even 20 GHz [23], have been reported. Thus, not only can OEICs be fabricated with MMIC devices to form OMMICs, there are inherent advantages (high speed, large bandwidth, light weight, high reliability, infinite isolation, etc) to such an integration that are attractive to the system designer.

However, improvements in MMIC control techniques, especially for systems composed of multiple MMICs, such as phased-array radar, are needed if MMICs are to become commercially viable. This is especially true for MMICs operating in noisy environments where use of an optical control signal can provide more reliable control due to the inherent immunity of optical fibers to rf interference [24]. In addition, MMICs that operate at remote sites from a central station, or that are placed onto surfaces with limited access (such as sensors placed on the skin of aircraft [25]), are difficult to control with all-electrical/microwave signals due to the high signal loss and large size of the control components [26]. Obviously, this is again a situation where optical control of microwave systems has a major advantage over traditional techniques. Now that we have discussed the need to control microwave circuits, and why optical techniques are preferable over traditional methods for certain applications, a review of the various control circuits frequently used is in order.

There are several ways to control microwave circuits. Phase shifters are often applied to shape antenna beam patterns [27], perform interferometry [28], and provide isolation between various microwave ports [29]. All of these are important microwave control functions that are typically performed using all-electronic or microwave techniques [30]. However, there are other techniques that are frequently employed, such as microwave switches [31] and attenuators [32,33].

Although traditional techniques are widely used due to their adequate performance and ease of fabrication or system insertion, they all suffer from one of the aforementioned drawbacks. In particular, with all of these techniques there is little or no isolation between the control signal and the microwave signal to be controlled. This can represent a serious problem for systems where multiple MMICs are to be controlled [34], such as in large (or even modest-sized) phased-array antennas. In such systems the number of radiating elements and, hence, MMICs, can approach tens of thousands [10].

An additional difficulty with all-electronic or microwave control is the routing of the control signal to the MMIC module. This requires either bulky wires, in the case of electrical control signals, or waveguiding components, in the case where microwave signals perform the control function. A third drawback has to do with timing errors, or, more commonly, timing jitter. This is a problem when a high degree of microwave control accuracy is required. All electrical systems can typically provide control with timing jitter in the nanosecond regime; optoelectronic techniques can provide similar control with picosecond jitter [3].

As discussed earlier, MMICs and OEICs are usually fabricated with the same material structure. It therefore seems reasonable that an attenuator for MMIC applications using OEIC techniques is feasible from a fabrication point of view. However, this is only true provided that the attenuator requirements of fast turn-on speed and laser diode activation are met.

## 1.2 Objectives of the Research

The three principal advantages of the optical control of microwave circuits just discussed were the high degree of isolation, noise immunity, and high-speed control. These three main points formed the basis of this research, namely, to demonstrate an optoelectronic attenuator suitable for controlling MMICs. This attenuator should be controllable with sub-nanosecond precision and provide greater than 30 dB of microwave attenuation. The attenuator must be all solid state (i.e., based on semiconductor components only) to permit eventual MMIC insertion, and must require reasonable optical power levels to achieve well-controlled attenuation levels. In addition, the attenuation must be achieved for time scales on the order of a nanosecond or greater; therefore, attenuation levels that can only be sustained for picosecond time frames are unacceptable (this design consideration helps to reduce the laser power requirement). Therefore, materials with carrier recombination lifetimes on the order of 1 ns or longer were considered.

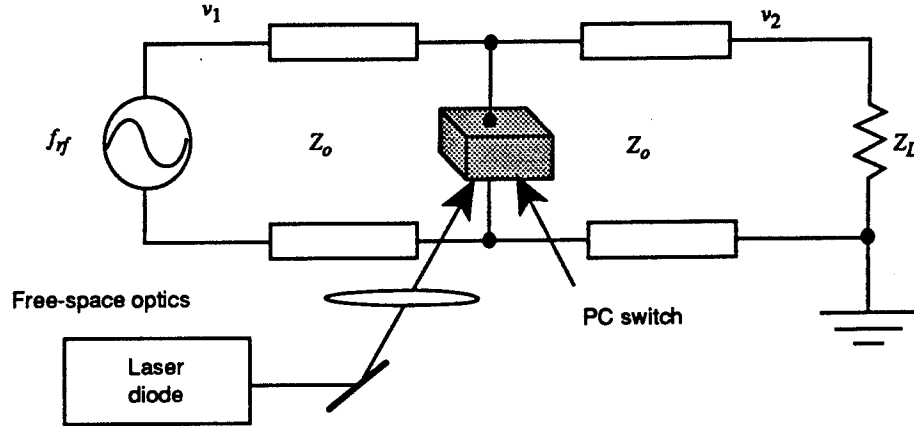
In addition to development of a suitable attenuation element, either the optical driver (i.e., laser diode) must be developed to do the job, or existing laser diode technology must be assessed and a suitable candidate device selected. Finally, new materials that might greatly improve the performance of the optoelectronic attenuator must be investigated; these new materials might also help reduce the cost of the attenuator by permitting device miniaturization, improving device handling and fabrication, or permitting the optoelectronic attenuator to properly function in harsh environmental conditions,

such as those at remote microwave sites. Any new materials must be adequately characterized, both electronically and optically, so that recommendations for future development can be intelligently made.

Finally, the optoelectronic attenuator must work; while it is important to perform detailed and thorough research, it is eventually the success of this project that will encourage MMIC designers to employ this technique on working MMIC systems.

As a preview of the next section, figure 1 shows the proposed hybrid optoelectronic attenuator. An embedded photoconductive (PC) switch resides within a high-speed microwave transmission line and is the attenuating element. A semiconductor laser diode (LD) is used both to activate the attenuator and to control the attenuation level. Either free-space optics or fiber optics (not shown in figure) may be used to deliver the optical power to the PC switch.

**Figure 1. Diagram of proposed hybrid optoelectronic attenuator scheme.  $Z_o = Z_L$ , which is equal to transmission line characteristic impedance.**



## 2. Microwave Optoelectronic Attenuator Scheme

With the motivation for this research discussed in section 1, we now develop the basis for the optoelectronic attenuator. The advantages of our scheme are as stated previously: high-speed control, a high degree of isolation between the control and microwave signals, and virtually jitter-free operation. In section 2.1 of this report, we present a general review of microwave attenuators, with an emphasis on MMIC attenuator circuits. This is followed by a discussion of how an optically controlled attenuator works.

Attenuators are usually classified in one of two categories: reflective attenuators and absorptive attenuators. This classification is also relevant to the optically controlled attenuator, and we will see that there are two related physical interpretations of how such a device might attenuate a microwave signal. In fact, how we classify the attenuator depends on how we interpret the interaction of the optical and microwave energy; we can postulate that the optoelectronic attenuator might function in either a reflection or an absorption mode. Since either mode of operation may be valid, experiments are necessary to determine the correct interpretation; these experiments are presented in section 4.

Photoconductivity in a semiconductor media is the basis for the optoelectronic attenuator, as well a host of other useful devices, and has been thoroughly studied by Lee [35]. For example, bulk GaAs photoconductive switches can be fabricated with dynamic resistances of less than 1 [36]. Also, the turn-on time of these devices is equal to the rise time of the optical trigger, a laser pulse of suitable power and wavelength.

Simply stated, optical photons impinging on a semiconductor substrate are converted to electron-hole pairs, which in turn constitute an electron-hole (i.e., solid-state) plasma [36]. How this solid-state plasma—which, for both optoelectronic attenuator schemes is generated within the semiconductor substrate of a high-speed PC switch—affects the propagation of a microwave signal is what differentiates the two attenuation schemes.

First, if we view the solid-state plasma/microwave signal interaction from a circuit analysis standpoint, then the plasma is seen as altering the local complex impedance of the microwave transmission line at the spatial location where it is induced. This impedance mismatch will, in turn, alter the propagation of the microwave signal by inducing a partial reflection of the microwave signal back toward the signal source. In addition to this partial reflection, some

energy will be absorbed by the real component of the impedance mismatch (i.e., due to resistive losses). Thus, upon introduction of an optically induced impedance mismatch, the transmission line load experiences a decrease in signal strength, which appears to be an attenuation to the load. For clarity, we will refer to an attenuator that operates in this fashion as a “reflective attenuator,” even though a small portion of the microwave power is also absorbed.

We can also view the optically induced plasma/microwave interaction using a more rigorous electromagnetic approach, whereby Maxwell's equations are solved directly. In this case, the physics of the plasma is directly accounted for as a change in the material properties of the microwave media, namely, as a change in the material's conductivity (and hence, permittivity). In this case, the plasma acts to increase the material's loss tangent, which, in turn, acts to absorb the microwave signal. As was the case for the reflective attenuator, there may also be an increase in signal reflection from the lossy media due to any optically induced impedance variations; however, the fraction of power that is reflected is normally much less than that absorbed. Therefore, we refer to the decrease in signal strength resulting from the direct interaction of the solid-state plasma with the microwave signal as an absorptive attenuation mechanism, and to optoelectronic attenuators that operate on this principle as “absorptive attenuators.”

In section 5, we describe optoelectronic attenuator experiments and determine the actual attenuation mechanism responsible for the optoelectronic attenuator (which turns out to be absorptive). However, both interpretations had to be explored not only to develop the optoelectronic attenuator, but to properly understand how it works. Therefore, the basis for both schemes is discussed in detail and their respective performances estimated. To put this work into proper perspective, MMIC attenuator techniques are now briefly reviewed and contrasted to optically controlled attenuators.

## 2.1 Optoelectronic Attenuator Motivation

In the introduction to this section, we briefly mentioned two microwave attenuation schemes, whereby the attenuation may be caused by either an absorption of the microwave signal by a solid-state plasma or by a reflection of the microwave signal from an optically induced impedance mismatch. Before we discuss how the optoelectronic attenuator will be implemented, a brief overview of microwave attenuators is in order. Since an excellent review of the relevant MMIC attenuation techniques has been presented by Bahl and

Bhartia [37], we point out the common features of all attenuators and contrast these with the key features of the optoelectronic attenuator.

For a microwave attenuator to be useful to the system designer, it must function with a minimum of reflected power being redirected back to the microwave source. This is important since high levels of reflected power may result in a change of the source characteristics, such as frequency "load pulling" [38], and, in extreme cases, since large reflected power levels may cause damage to the source active element(s). Thus, useful attenuators can provide adequate attenuation sufficient to meet the system application, while minimizing the amount of reflected power seen by the source. This would imply that an absorptive attenuator would be an "ideal" candidate for all MMIC applications, especially for low-level signal operation. However, attenuation of high-level signals can pose difficulties due to thermal heating in the absorptive attenuator which, in turn, alters its characteristic impedance and thus increases the reflected power back toward the source.

In principle, any arbitrary impedance may be matched to another if an impedance transformer, which is ideally many wavelengths long [39], is used. Thus, as the attenuation in an absorptive attenuator increases, the impedance may also change and a matching network might be used to minimize reflections. However, even if the wavelength of the microwave signal in the transmission line is in the millimeter-wave range, this still implies that rather long matching networks may be necessary. Therefore, absorptive attenuators, and especially those relying on impedance matching networks to reduce power reflections, are less desirable for MMIC integration due to the limited amount of MMIC real estate. In addition, absorptive attenuators dissipate considerable microwave power, and the need to dissipate the resulting thermal energy away from temperature-sensitive active devices is obvious.

Reflective attenuators, such as the type discussed by Weber [40], can be used to circumvent these problems; with these, the reflected microwave power is redirected to a matched load with the aid of a non-reciprocal transmission line element, such as a circulator [41] or transmit and receive (T/R) module [42]. Thus, the matched load can be either off-chip or on-chip at a convenient location that is far away from any temperature-sensitive components. However, the principal disadvantage of this approach is the need for a microwave circulator (or T/R switch), which is normally comprised of a three-port (or higher order) transmission line structure and a non-reciprocal element, typically a ferrite resonator, which permits power flow in

only one direction (either from port 1 to port 2, or port 2 to port 3, etc). Although considerable progress has been made recently to synthesize circulators using active elements for MMICs [42], these devices do not have sufficient isolation to prevent some of the reflected power from reaching the microwave source. For some low-power applications, this is acceptable, but for high-power applications, this non-ideal performance is cause for concern.

Simply stated, for low-power applications where microwave signals are to be attenuated, use of existing attenuator schemes (either absorptive or reflective) is acceptable. However, when high-power levels are involved, such as with high-power radars and sensors [43], these traditional approaches have serious drawbacks. More importantly, they cannot be activated remotely without significant control timing jitter; thus, their suitability for simultaneous control of multiple microwave circuits is in question. Although other optical control schemes have proven their relative worth for some applications [17,18,34], these are all fairly complicated schemes that require either additional device fabrication steps or specialized device topologies. In addition, these techniques may be slow, implying that high-speed control may not be possible [44].

Since every microwave system—in fact, every MMIC—contains transmission lines, controlling the relative attenuation by optical injection of a solid-state plasma within these pre-existing transmission lines appears to be a convenient technique. The optical power levels that are required to achieve useful attenuation values are below the threshold levels for non-linear fiber-optic effects [45]. (We see in sect. 5.4 that less than 150 mW of laser power results in 45 dB of attenuation at 1.7 GHz.) Therefore, a single laser source can be used to optically control the attenuation of multiple MMIC transmission lines using standard fiber-optic techniques. Therefore, the control signal “timing error” associated with this approach is equal to the error in cleaving the individual fibers to the correct length, and to differences in the thermal expansion of the individual fibers. Since both of these errors in timing can be on the order of a few picoseconds (a 1-cm discrepancy in fiber length yields a 33-ps timing error), timing errors of less than a few picoseconds are easy to achieve. Now that we have explained the motivation for developing an optoelectronic attenuator, we discuss in further detail the two possible optoelectronic attenuator schemes mentioned earlier, starting with the reflective attenuator scheme.

## 2.2 Reflective Optoelectronic Attenuator Scheme

The reflective attenuator scheme is based on the fundamental electromagnetic circuit principle of partial wave reflection from an impedance discontinuity. If a microwave signal is propagating on a transmission line of characteristic impedance  $Z_o$ , and encounters a different characteristic impedance  $Z$ , where  $Z = Z_o \pm \Delta Z$ , and  $\Delta Z$  is the deviation in impedance from  $Z_o$ , the microwave signal will be partially reflected by, and absorbed in, this transmission line discontinuity. The voltage reflection coefficient,  $\Gamma$ , may be used to represent this situation and is defined as

$$\Gamma \equiv \frac{Z - Z_o}{Z + Z_o} . \quad (1)$$

Therefore, if  $Z = Z_o$ , then  $\Gamma = 0$  and there is no voltage (i.e., signal) reflection. When  $Z = 0$  (i.e., short-circuited transmission line case) then  $\Gamma = -1$ , implying that the voltage traveling wave is reflected with a  $180^\circ$  phase shift (note that for the current traveling wave,  $\Gamma = +1$ , and no phase shift is incurred). If  $\Gamma$  is between these two extremes, such as when  $Z \neq Z_o$ , then a fraction of the microwave signal will also be absorbed due to the real (i.e., resistive) component of the complex discontinuity impedance,  $Z$ , where  $Z = [(R + j\omega L)/(G + j\omega C)]^{1/2}$ , and  $R$ ,  $L$ ,  $G$ , and  $C$  are the transmission line distributed resistance, inductance, conductance, and capacitance, respectively. Thus, from the point of view of the transmission line load, the microwave signal amplitude has decreased due to the partial reflection and, hence, an effective attenuation has been realized. For clarity, we refer to this attenuation scheme as a "reflective attenuator," even though a small fraction of the microwave signal is also absorbed. Later we see that for the reflective attenuator scheme to work well, a majority of the signal must be reflected, thus further justifying our choice of this terminology.

We constructed the reflective optoelectronic attenuator by fabricating a microwave transmission line on a PC substrate. PC materials convert light (i.e., photons) into electrical charge (i.e., electron-hole pairs). We refer to this photo-induced charge as an electron-hole, or solid-state, plasma. The induced plasma density  $N_e$  alters the material's conductivity  $\sigma$ , since  $\sigma$  is proportional to  $N_e$  by the simple relation  $\sigma = e\mu N_e$ , where  $e$  is the electronic charge and  $\mu$  is the sum of the electron and hole mobilities. Thus, illumination of the PC substrate with the appropriate light source alters the substrate conductivity at the illumination point, which in turn alters the electrical resistance of the photoconductor at this spatial location. Since this is the substrate of a planar microwave transmission line, this resistance

change alters the local characteristic impedance of the transmission line at the point of illumination. Therefore a shunt resistance change is induced at the point of illumination, and the laser beam power and profile can be used to accurately control this localized impedance change.

Thus, all that is required to turn on the reflective attenuator is to create the photo-induced solid-state plasma between the center conductor and ground plane of the high-speed transmission line. Two of the most commonly used PC materials are silicon (Si) and GaAs (the development of high-speed PC switches using these materials is outlined in sect. 4). Bulk GaAs PC switches can be fabricated with off-state (i.e., dark) resistances on the order of a few megaohms, with dynamic on-state resistance values of less than  $1 \Omega$  [35]. For these devices, the turn-on time is equal to the rise time of the optical trigger, namely, a laser pulse of suitable power and wavelength. Recent work on high-speed LDs indicates that these devices can be modulated well beyond 10 GHz [46] and could thus serve as the high-speed trigger mechanism for the reflective attenuator. Therefore, it seems plausible that a reflective optoelectronic attenuator can be suitably constructed.

The basic concept for the reflective attenuator is illustrated in figure 2. Here we show ideal transmission line and lumped circuit elements. In the reflective attenuator off-state, a microwave signal propagates down the transmission line and is absorbed by the matched load,  $Z_L$ , where  $Z_L = Z_0$  ( $Z_0$  is the transmission line characteristic impedance). When the microwave signal is to be attenuated, a trigger signal is sent to the LD. The LD, responding in tens of picoseconds to the trigger signal [47], activates the embedded PC switch, which then changes the shunt impedance of the transmission line at the point of LD illumination. Since the value of shunt on-state resistance,  $R_{on}$ , is proportional to the LD peak output power and beam profile, the degree of microwave attenuation can be accurately controlled. In the limit that the shunt impedance goes to zero, all the microwave power is reflected back to the source with no absorption taking place in the shunt impedance. The switch conducts for a time equal to the laser pulselength, and opens in a time equal to the PC carrier recombination lifetime,  $\tau$ , [46]. Hence, the photo-induced shunt impedance will be maintained for at least the duration of the laser pulse, and therefore is fully controllable.

The reflective attenuator performance can be predicted using standard transmission-line theory. The most straightforward approach is to use two-port theory, and therefore  $ABCD$  matrices, to model this circuit. Assume that a variable resistance is placed in shunt across an

ideal loss-less transmission line, as shown in figure 3. We can now calculate the resulting attenuation at port 2 induced by this shunt resistance from elementary transmission-line theory. The characteristic equations for this (and any general) two-port network are

$$\begin{aligned} v_1 &= A \cdot v_2 + B \cdot i_2 \\ i_1 &= C \cdot v_2 + D \cdot i_2 \end{aligned} \quad (2)$$

Therefore, once the  $ABCD$  matrix elements are known for each of the components in the two-port network, the overall transfer function of the network can be determined. The  $ABCD$  matrix of a shunt admittance,  $Y$ , is easily calculated and yields  $A = 1$ ,  $B = 0$ ,  $C = Y$ , and  $D = 0$ , where the shunt admittance is the reciprocal of the shunt on-state resistance,  $Y = 1/R_{on}$ . The corresponding  $ABCD$  matrix elements of a loss-less transmission line of length  $l$  are  $A = \cos\theta$ ,  $B = jZ_0\sin\theta$ ,  $C = jY_0\sin\theta$ , and  $D = \cos\theta$ , where  $\theta = 2\pi l/\lambda$  is the electrical length of the loss-less transmission line and  $\lambda$  is the wavelength of the propagating mode.

**Figure 2. Hybrid reflective optoelectronic attenuator schematic, detailing all principal attenuator components:  $Z_o = Z_L = 50 \Omega$ .  $S_{21} = 20\log_{10}(v_t/v_i)$ .**

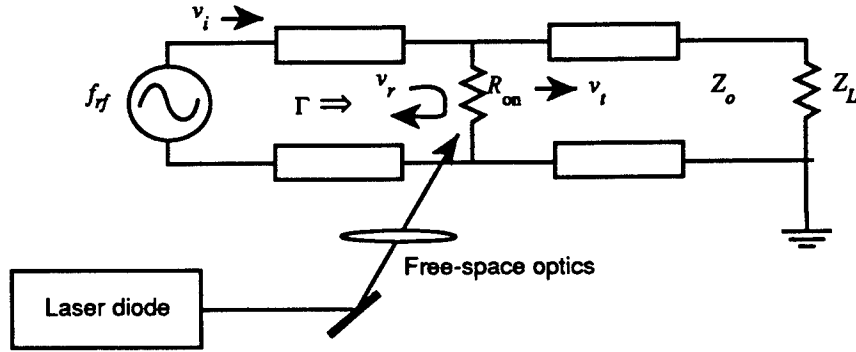
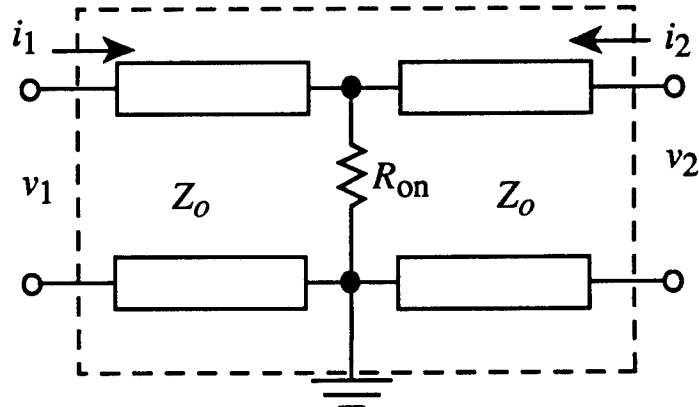


**Figure 3. Two-port model of loss-less transmission line with embedded shunt resistance,  $R_{on} = 1/Y$ . Two-port boundary is denoted by dashed box.**



For the reflective optoelectronic attenuator model, we assume a purely resistive shunt resistance, denoted by  $R_{\text{on}}$ . Assuming a 50- $\Omega$  transmission system, the microwave scattering parameters for the circuit shown in figure 3, for which the  $ABCD$  matrix elements were just described, can be computed as follows [39].

The voltage reflection coefficient,  $\Gamma$ , is defined as  $\Gamma \equiv v_r/v_i$ , where  $v_r$  and  $v_i$  are the reflected and incident voltages, respectively.  $S_{11}$ , the scattering coefficient that describes the amount of voltage reflected from a given microwave circuit element, is defined as  $S_{11} \equiv \Gamma$ .

The insertion loss in a microwave circuit is usually represented by the voltage scattering coefficient element  $S_{21}$ , which is the ratio of the voltage at port 2 to port 1 (hence the subscript "21"). More precisely, when  $\Gamma_{\text{load}} = 0$ ,  $S_{21} \equiv v_t/v_i$ , where  $v_t$  and  $v_i$  are the two-port through (i.e., output) and incident voltages, respectively. We can represent  $S_{21}$  in terms of power, in decibels, and therefore define the attenuation in the two-port network as

$$S_{21}(\text{dB}) = 20\log_{10} \left\{ \frac{v_t}{v_i} \right\}. \quad (3)$$

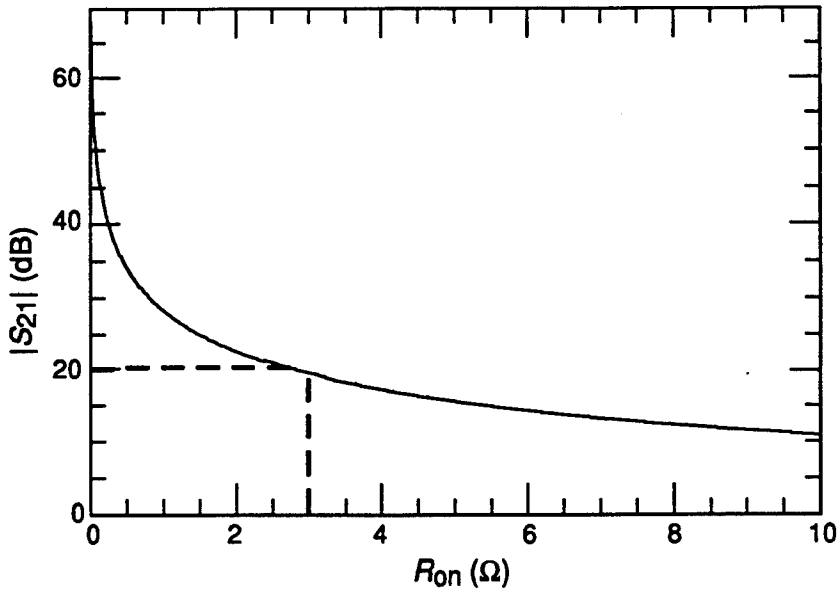
Now all that needs to be done is to derive  $S_{21}$  in terms of the  $ABCD$  matrix for a shunt element embedded in a loss-less transmission line; then we can calculate the expected circuit attenuation for a given shunt resistance,  $R_{\text{on}}$ . This is a simple exercise, and the result is  $S_{21} = 2/(2 + Z_0 Y)$  [39]; therefore,  $S_{21}$  for the reflective attenuator is

$$S_{21}(\text{dB}) = 20\log_{10} \left\{ \frac{2}{2 + Z_0 Y} \right\}, \quad (4)$$

where  $Y = 1/R_{\text{on}}$ , and  $R_{\text{on}}$  is the PC switch on-state resistance.

For reference,  $|S_{21}|$  is plotted versus  $R_{\text{on}}$  in figure 4. Clearly,  $R_{\text{on}} \approx 3 \Omega$  should result in an attenuation of  $\approx 20$  dB; this "20-dB design goal" is indicated in the figure by the dashed lines. We therefore see from this prediction what is required for the reflective attenuator to reach the 20-dB design goal:  $R_{\text{on}} \approx 3 \Omega$ . In section 4 we discuss a detailed series of experiments using a high-speed GaAs PC switch to determine if an LD can reduce the shunt resistance of a GaAs high-speed PC switch from  $\approx 1 \text{ M}\Omega$  to  $\approx 3 \Omega$ .

**Figure 4. Reflective optoelectronic attenuator theoretical prediction for attenuation,  $|S_{21}|$ , versus shunt on-state resistance,  $R_{on}$ , due to reflection coefficient  $\Gamma$ .  $Z_0 = 50 \Omega$ .**



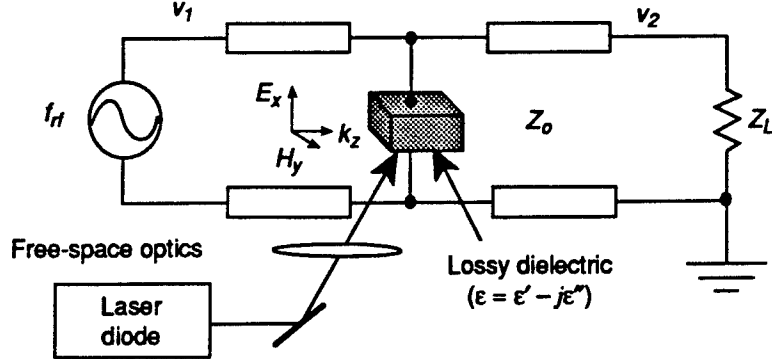
### 2.3 Absorptive Optoelectronic Attenuator Scheme

As mentioned at the beginning of this section, the attenuation mechanism for the optoelectronic attenuator may be due to plasma absorption in the microwave PC switch. The basic principles behind this mode of attenuation have been studied rather extensively in the literature [36,48]. In this section we explore the physics behind this mode of operation and, as for the reflective attenuator in figure 4, we estimate the performance one can expect from the absorptive optoelectronic attenuator scheme.

If we assume that a TEM (transverse electromagnetic) wave is propagating through a dielectric medium of permittivity,  $\epsilon_b$ , where  $b$  indicates that the permittivity is due to bound electrical charges (i.e., electrons and holes for a semiconductor), the introduction of additional charge into the semiconductor will alter the material's dielectric properties. Hence, a correct expression for the effective permittivity,  $\epsilon$ , due to the contribution of both bound charges,  $\epsilon_b$ , and free charges in the solid-state plasma,  $\epsilon_p$ , must be derived. An excellent treatment of the classic problem of TEM wave propagation through lossy metals is presented by Ramo et al [48] and, since the present situation (i.e., wave propagation through a lossy dielectric) is analogous to this treatment, it suffices to cover only the important features of this theory in this section.

The present situation is shown in figure 5. We see that a TEM wave is incident on a dielectric slab of finite conductivity,  $\sigma$ , where the most general case of a complex conductivity is considered;  $\sigma = \sigma' - j\sigma''$ . Since the effective permittivity,  $\epsilon$ , is related to  $\sigma$  by Ohm's Law

**Figure 5. Hybrid “absorptive” optoelectronic attenuator.**  $E_x$  and  $H_y$  are complex field amplitudes, and  $\epsilon = \epsilon' - j\epsilon''$  is lossy dielectric's effective permittivity.



$(\sigma = j\omega\epsilon)$ , it, too, is complex. We first discuss TEM wave propagation through a simple linear isotropic dielectric media of permittivity  $\epsilon$ .

Assuming that the TEM wave is time-harmonic, we can immediately write down the following relations for the TEM wave:

$$\begin{aligned} \mathbf{E} &= E_x e^{jkz} \hat{x}, \\ \mathbf{H} &= H_y e^{-jkz} \hat{y}, \text{ and} \\ jk &= (\alpha + j\beta) \hat{z}, \end{aligned} \quad (5)$$

where  $E_x$  and  $H_y$  are the electric and magnetic field vector amplitudes, respectively,  $k$  is the complex propagation constant (also a vector quantity, as denoted by the bold type face), and  $\alpha$  and  $\beta$  are the propagation constant in radians per meter and attenuation coefficient in nepers per meter, respectively. Substitution of  $k$  into the harmonic field equations of equation (5) yields, for example,  $\mathbf{E} = E_x \exp\{-\alpha z - j\beta z\}$ , where clearly the wave experiences an attenuation due to the decaying exponential factor  $\exp\{-\alpha z\}$ , and propagates harmonically as  $\exp\{-j\beta z\}$ .

This is the case for most simple lossy dielectric media. We see later in this report that for lossy dielectrics, such as for a solid-state plasma in a typical semiconductor, some interesting effects occur. To model the solid-state plasma, we start by describing the motion of an electron in the semiconductor material. The well-known equation of motion for the electron is as follows:

$$m^* \frac{dv}{dt} = -eE - m^*vv, \quad (6)$$

where  $m^*$  is the effective electron mass in the semiconductor, which is  $1.08m_0$  for silicon [49], where  $m_0$  is the electron rest mass ( $9.1 \times 10^{-31}$  kg),  $v$  is the electron drift velocity due to applied electric field  $E$ ,  $e$  is the electron charge ( $1.6 \times 10^{-19}$  C), and  $v$  is the electron colli-

sion frequency in the plasma (essentially, the electron motion is harmonic with  $E$  except for the damping term  $m^*vv$ ).

Using equations (5) and (6), and Maxwell's equations, we derive the contribution of the solid-state plasma to the overall semiconductor permittivity. From equation (6), the electron velocity  $v$  can be determined if we assume that the velocity is time harmonic (i.e.,  $\exp(-j\omega t)$  dependence):

$$v = \frac{-eE}{m^*(v + j\omega)} . \quad (7)$$

Since the current flow associated with this electron motion is primarily due to conduction current, then  $J = eN_e v$ , where a new term,  $N_e$ , has been introduced to describe the solid-state plasma electron density, where the units of  $N_e$  are  $\text{cm}^{-3}$ . Substitution of equation (7) into  $J$  yields

$$J = \frac{N_e e^2 E}{m^*(v + j\omega)} = \sigma E , \quad (8)$$

where we see that the conductivity,  $\sigma$ , is indeed complex. Substitution of equation (8) into Maxwell's equations gives

$$\nabla \times H = \frac{N_e e^2 E}{m^*(v + j\omega)} + \epsilon_b \frac{\partial E}{\partial t} . \quad (9)$$

From equation (9), we can now derive the effective permittivity of a semiconductor containing a solid-state plasma. For a time-harmonic TEM wave, manipulation of equation (9) directly results in the well-known complex permittivity of a lossy dielectric media:

$$\begin{aligned} \epsilon' &= \epsilon_b \left[ 1 - \frac{\omega_p^2}{v^2 + \omega^2} \right] , \\ \epsilon'' &= \epsilon_b \frac{\omega_p^2 v}{\omega(v^2 + \omega^2)} , \end{aligned} \quad (10)$$

where  $\epsilon = \epsilon' - j\epsilon''$  and a new term,  $\omega_p$ , the plasma frequency, has been introduced;  $\omega_p^2 = N_e e^2 / (m^* \epsilon_0)$ . The general form of the complex propagation constant is  $jk = \alpha + j\beta$ , where  $k^2 = \omega^2 \mu(\epsilon' - j\epsilon'')$ ,  $\mu = \mu_0 = 4\pi \times 10^{-7} \text{ H/m}$  is the permeability of free space, and  $c = (\mu_0 \epsilon_0)^{-1/2}$  is the speed of light in vacuum. Therefore the propagation constant,

which describes the propagation of an electromagnetic wave through a solid-state plasma, is

$$k = \omega \sqrt{\mu_b \epsilon_b} \sqrt{1 - \left( \frac{\omega_p^2}{v^2 + \omega^2} \right) - j \left( \frac{\omega_p^2 v^2}{\omega(v^2 + \omega^2)} \right)}. \quad (11)$$

There are many types of plasmas [50]; therefore, the limits of equation (11) are of interest to us since this will simplify the analysis considerably. For a solid-state plasma, we can assume that the collision frequency  $v = v_{th}/l_c$ , where  $v_{th} \approx 10^7$  cm/s is the thermal carrier velocity and  $l_c \approx 100$  Å is the thermal mean-free scattering length, respectively.  $\epsilon_b = \epsilon_0$ , which is the permittivity of free space. Since  $jk = \alpha + j\beta$ ,  $\alpha$  and  $\beta$  can now be written using equation (11)

$$\alpha = \omega \sqrt{\frac{\mu \epsilon'}{2}} \sqrt{1 + \left( \frac{\epsilon''}{\epsilon'} \right)^2 - 1} \quad (12)$$

$$\beta = \omega \sqrt{\frac{\mu \epsilon'}{2}} \sqrt{1 + \left( \frac{\epsilon''}{\epsilon'} \right)^2 + 1}$$

where  $\alpha$  and  $\beta$  are the electromagnetic wave attenuation and propagation coefficients within the solid-state plasma, respectively.  $\alpha$  represents the total losses experienced by the propagating electromagnetic wave [48] and, for the case of the solid-state plasma, we assume that the dominant loss mechanism is plasma absorption.

Using equation (10) to describe the solid-state plasma permittivity and equation (12) to describe the wave propagation, we can estimate the power loss experienced by the wave within the solid-state plasma. Using the Poynting vector,  $S = E \times H$ , to compute the actual power loss through the plasma, we find that  $S = E_x^2/2\eta_r \exp(-2\alpha z)$ , where  $\eta_r = (\mu_r/\epsilon_r)^{-1/2}$  is the characteristic impedance of the medium. Thus, for a propagation length of  $z = 1$  cm, the wave is attenuated by an amount equal to the exponential factor  $\exp(-2\alpha)$ . Expressing the power loss in terms of the microwave scattering parameters,  $S_{ij}$ , where  $i$  and  $j$  refer to the measurement port for a two-port network as described in the last section, the attenuation from port 1 to port 2, per centimeter, is given by

$$S_{21}(\text{dB/cm}) = 10 \log_{10} \left\{ \exp \left[ \omega \sqrt{\frac{\mu \epsilon'}{2}} \sqrt{1 + \left( \frac{\epsilon''}{\epsilon'} \right)^2 - 1} \right] \right\}. \quad (13)$$

We can now plot the anticipated attenuation of the microwave signal propagating through the absorptive optoelectronic attenuator as a function of the plasma density,  $N_e$  (and hence as a function of the plasma frequency,  $\omega_p$ ); this result is shown in figure 6 for the design frequency,  $f = 3$  GHz ( $\omega = 2\pi f$ ). Note that attenuation values of 20 dB are predicted for plasma densities on the order of  $9 \times 10^{16} \text{ cm}^{-3}$ .

Plasma densities of this magnitude are readily achievable using optical illumination with laser diodes [35], and a simple analysis can be employed to predict the required laser peak power to achieve the attenuation values shown in figure 6. This analysis is straightforward and is basically a matter of counting the number of photons absorbed by a 1-cm-thick semiconductor slab and estimating the percentage converted into electron-hole pairs:

$$P_{LD} = \frac{N_e \cdot h\nu \cdot A_{spot}}{\eta(1-R) \cdot \tau_r} , \quad (14)$$

where  $P_{LD}$  and  $A_{spot}$  are the required laser diode peak power and spot size, respectively,  $R$  is the reflectivity of the laser beam at the semiconductor surface,  $\eta$  is the internal quantum efficiency of the material [51], which is an estimate of the conversion efficiency of absorbed photons into electron-hole pairs,  $h\nu$  is the photon energy, and  $\tau_r$  is the PC carrier recombination lifetime of the photo-induced carriers.

For silicon,  $R$  is approximately 0.3. Assuming  $A_{spot} = 10 \times 100 \mu\text{m}$  and  $\eta = 0.1$ , which is reasonable for an indirect band-gap material [52]; the laser power required to induce the attenuation values of figure 6 was computed and is shown in figure 7.

The analysis described in this section predicts attenuation values of  $\approx 20$  dB for plasma densities that are on the order of  $9 \times 10^{16} \text{ cm}^{-3}$ ,

**Figure 6. Theoretical prediction for attenuation,  $S_{21}$ , versus solid-state plasma density,  $N_e$ , due to plasma absorption.  $f = 3$  GHz.**

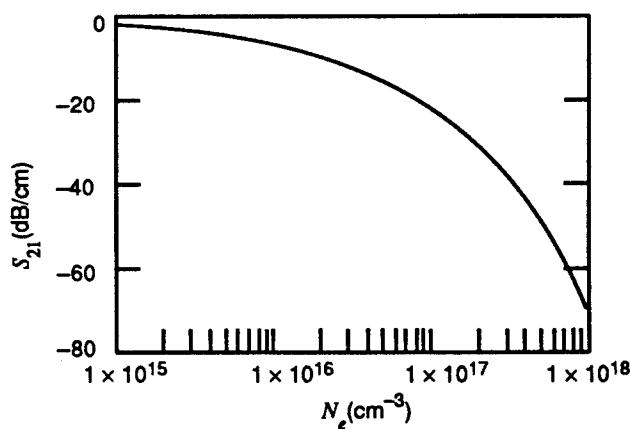
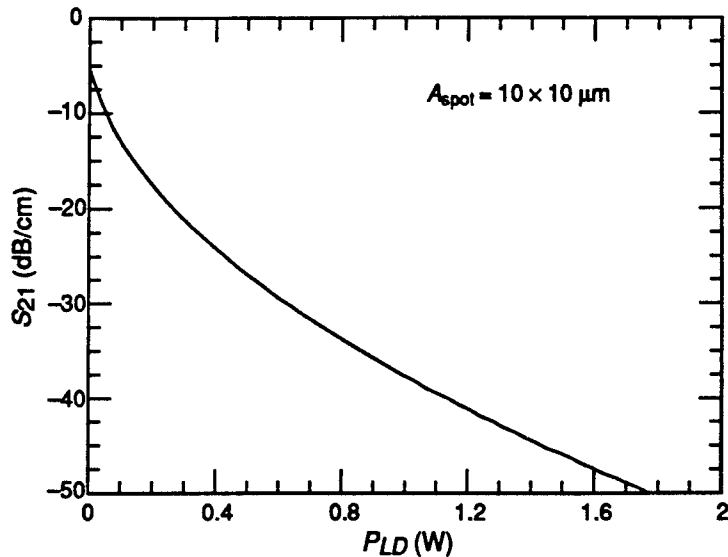


**Figure 7. Theoretical prediction for attenuation,  $S_{21}$ , versus laser diode power,  $P_{LD}$ , for plasma density shown in figure 6.**



and it has been shown that the predicted LD power requirement of 750 mW to achieve these values is reasonable. It should be noted that for a plasma density of  $10^{15} \text{ cm}^{-3}$ , the corresponding plasma frequency is  $1.8 \times 10^{13} \text{ rad/s}$  (or  $f_p = 2.86 \text{ THz}$ ). The design frequency is 3 GHz; thus the necessary condition for plasma absorption ( $\omega_p \geq \omega$ ) is met [48].

## 2.4 Summary

We have presented the basis for two hybrid optoelectronic attenuator schemes. Two optically induced absorption mechanisms, a reflection from an impedance discontinuity and an absorption in a solid-state plasma, have been presented, as well as the projected performance from each scheme. It was observed that the reflective attenuator predicts 20 dB of attenuation for an optically induced shunt resistance in the microwave transmission line of  $3 \Omega$ . The absorptive attenuator prediction is that 20 dB/cm of attenuation can be achieved for plasma densities of approximately  $10^{17} \text{ cm}^{-3}$ , and that the anticipated LD power requirement for such a plasma density is approximately 750 mW.

We have contrasted optically controlled microwave devices with all-electrical versions, and have pointed out the situations where optical control is preferable. In order for the optoelectronic attenuator to be realized, laser diode sources must not only be available to provide the necessary output power, but must be capable of high-speed modulation so that the optoelectronic attenuator can provide high-speed microwave control.

Since the laser diode is therefore a critical element to both optoelectronic attenuator schemes, considerable research was performed to ensure that a suitable laser was available for this application. The laser diode research and development conducted as part of this work is presented in the next section.

### 3. Laser Diode Development

Implementation of the optically controlled attenuator requires that two principal semiconductor devices be developed. One is the high-speed PC switch, which is the attenuating element. The other is the semiconductor LD, which is the control device for the attenuator. In the ideal situation, a single LD would emit sufficient optical power to create an electron-hole plasma within the high-speed PC switch to attenuate propagating microwave signals. In addition, the laser output would have sufficient optical power to achieve the attenuation values that meet the microwave system design specifications. Lastly, the LD would be easy to turn on and would require a low level of input electrical power to operate.

Much work has been done to develop high-speed LDs for the telecommunications industry [53]. Some of these devices consist of two LD contact regions—the first provides gain, while the second is reverse biased and modulated with the information signal [54,55]. To date, gigahertz data rates have been achieved with this approach [56], indicating that sub-nanosecond LD turn-on times are feasible. However, these are typically low-power devices ( $\approx 100$  mW), which are made by the formation of an optical ridge waveguide on the LD surface; this waveguide decreases the modulator section capacitance (by reducing the contact area), thus achieving high-speed performance (the ridge mainly serves as a light-confining region to ensure single-mode laser operation).

Conversely, very-high-power LDs have been developed (in the laboratory at the University of Maryland and by others), that use a “broad-area” LD geometry. For example, we have measured peak optical powers in excess of 1 W at  $\lambda = 840$  nm. In addition, we have Q-switched two-section broad-area LDs with estimated peak powers of greater than 6 W and pulsedwidths of  $< 30$  ps [57].

In section 4 we discuss in detail the relationship between the PC switch material and the corresponding LD emission wavelength. The band-gap energy is 1.1 eV for Si and 1.41 eV for GaAs, corresponding to characteristic wavelengths,  $\lambda$ 's, of 1.13 and 0.88  $\mu\text{m}$ , respectively. Thus, GaAs/AlGaAs LDs with  $\lambda$ 's as low as 780 nm should allow intrinsic photon absorption to occur at the surface of an Si PC switch. For the GaAs PC switch, the LD wavelength must be tailored to meet the intrinsic absorption condition; fortunately, this can be accomplished with standard LD quantum-well design techniques.

In summary, the critical LD parameters for proper operation of the microwave attenuator are the following: (1)  $\lambda$  must be matched for both Si and GaAs attenuators, (2) the optical intensity must be sufficient to achieve useful plasma densities, and (3) turn-on times must be at sub-nanosecond speeds so that high modulation rates can be achieved. These requirements are quite stringent and may not be fully realizable with traditional LD triggering schemes. As a consequence, several LD schemes were studied and are presented in this section. Before discussing the various LD types, a brief description of the physics of both multi-section and quantum-well lasers is presented. Then several LD implementation schemes are discussed. Finally, research undertaken to improve the overall efficiency of high-power broad-area LDs is presented: a 37-percent increase in laser diode efficiency has been demonstrated.

### 3.1 Multi-Section Quantum-Well Laser Diodes

During this research, several types of edge-coupled, Fabry-Perot, quantum-well laser diodes were developed for the optoelectronic attenuator because of their relatively high quantum efficiency [58] and ease of fabrication. Since excellent treatments of the various types of LDs are available in the literature [59,60], only the basic structure of quantum-well lasers is discussed here.

The basic LD structure consists of a p-n junction, a Fabry Perot cavity that is formed by cleaving the semiconductor crystal and ohmic contacts, which are necessary for electrical connection. LDs are current-controlled devices that may be operated in either a continuous wave (cw) or pulsed mode, where thermal dissipation dictates the possible mode of operation. Sandwiched between the p-n junction is the active layer, where the recombination of electrons and holes results in the generation of photons. The active region may be composed of either a single quantum well (SQW) or multiple quantum well (MQW) structure. The material surrounding the active region serves as an optical waveguide, and this waveguide can consist of either a graded index region or an abrupt index region, known respectively as GRINSCH (graded-index separate confined hetero-structure) or STINSCH (step-index separate confined hetero-structure) optical structures.

Figure 8 is a schematic diagram of the gain medium of a GRINSCH SQW laser structure used to fabricate LDs during this research. Table 1 lists the actual material profile of this GRINSCH LD structure, and indicates for each layer the corresponding thickness, molar fraction of Al present, and purpose. In this case, the active region consists of a 100-Å-wide SQW, and the optical intensity is guided by

**Figure 8. GRINSCH LD device material structure. Active area is SQW 80 to 100 Å wide. Al concentration (x) and layer thicknesses are shown in table 1.**

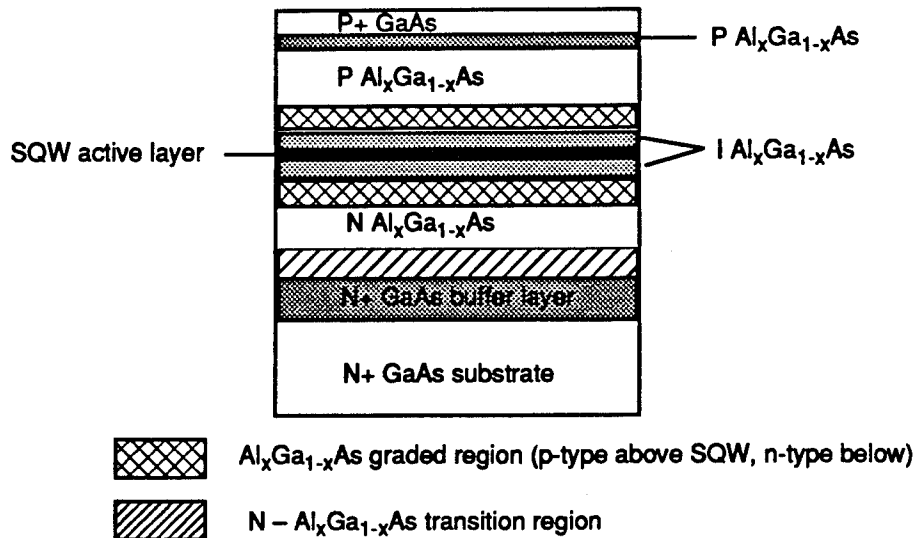


**Table 1. MBE 330 SQW GRINSCH laser structure.**

Layer	Thickness (Å)	Composition Al <sub>x</sub> Ga <sub>1-x</sub> As	Graded x1→x2	Doping <sup>1</sup>	Concentration (×10 <sup>17</sup> cm <sup>-3</sup> )
Contact	2,000	0.0	—	Be	~500
Grade	1,500	0→0.7	yes	Be	50
Clad-p	10,000	0.7	—	Be	10
Grin-p	1,500	0.7→0.3	yes	—	—
Step	80	0.3	—	—	—
Q-Well	80–100	0.0	—	—	—
Step	80	0.3	—	—	—
Grin-n	1,500	0.3→0.7	yes	—	—
Clad-n	8,000	0.7	—	Si	5
Transition	1,500	0→0.7	yes	Si	5
Buffer	2,000	0.0	—	Si	30
Substrate	>100 μm	0.0	—	Si	30

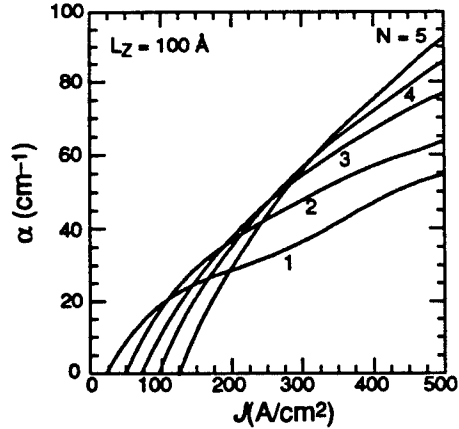
<sup>1</sup>n-type dopant = Si; p-type dopant = Be.

the AlGaAs cladding layers, as shown. An MQW laser typically differs from the SQW laser shown in figure 8 in that the SQW active region is replaced with an MQW. Otherwise, a GRINSCH MQW laser is identical to the SQW structure shown in figure 8. The basic physics of both SQW and MQW structures are well treated in the literature [59,61], with an excellent comparison between the two types given in figure 9 [61]. Basically, the difference between the two types of quantum-well lasers can be summarized with the following three approximate relations [61]:

$$g_{MQW} \equiv N \cdot g_{SQW} \quad (15)$$

$$f_r \propto \sqrt{\alpha \cdot \frac{P_o}{\tau_p}} \quad (16)$$

**Figure 9. LD performance as function of quantum well number,  $N$ , from Arakawa and Yariv [61]. Modal gain,  $\alpha$ , versus current density,  $J$ , for quantum well  $L_Z = 100 \text{ \AA}$  wide.**



$$J_{th, MQW} \equiv N \cdot J_{th, SQW} , \quad (17)$$

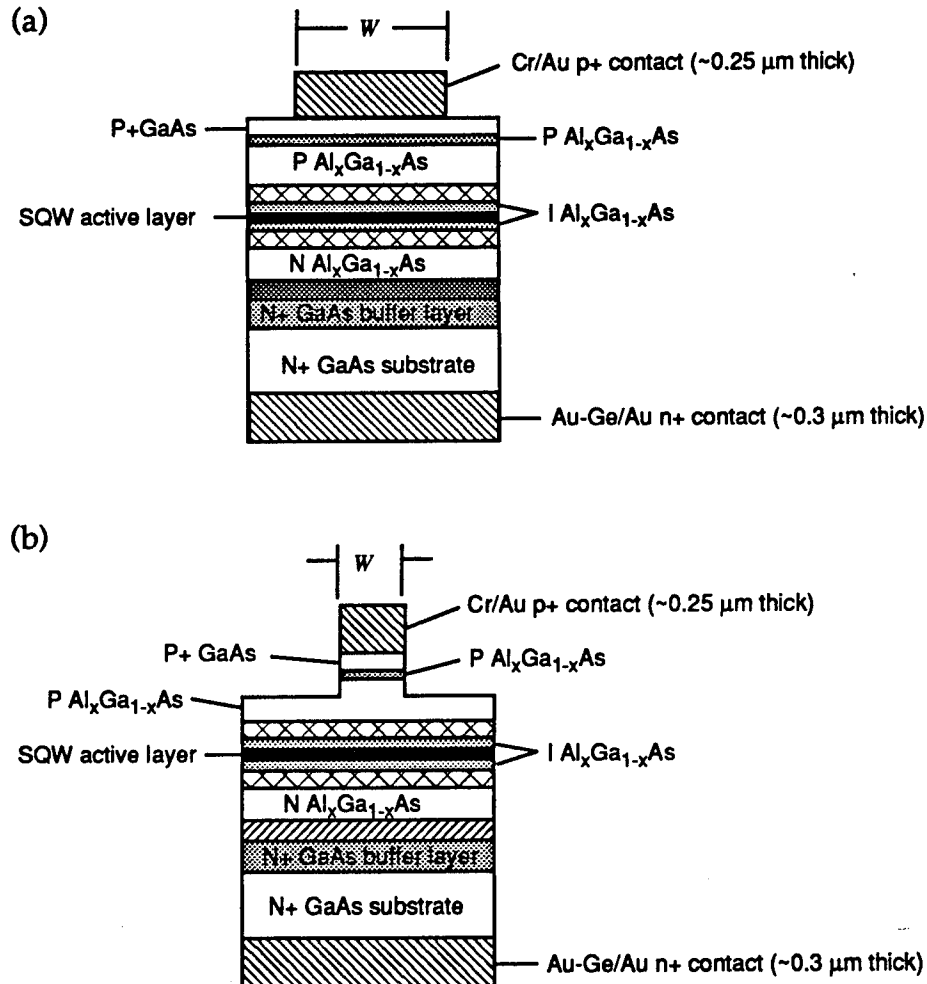
where  $g_{SQW}$  and  $g_{MQW}$  are the SQW and MQW modal gains, respectively.  $f_r$  is the relaxation oscillation frequency,  $\alpha$  is the differential gain  $\equiv \partial g / \partial n$  (where  $n$  is the carrier density in the laser active region),  $P_o$  is the photon density, and  $\tau_p$  is the photon lifetime.  $J_{th, MQW}$  and  $J_{th, SQW}$  are the threshold current densities for the MQW and SQW lasers, respectively, and  $N$  is the number of wells.

Note that equation (15) shows that MQW lasers can operate with gain factors that are approximately  $N$  times that of a similar SQW device, which is evident in figure 9; for  $N = 5$  and a current density  $J$  of  $500 \text{ A/cm}^2$ , we see that the modal gain of this MQW is approximately 68 percent greater than for the SQW ( $N = 1$ ) case. Equation (16) indicates that  $f_r$  is maximized when the differential gain  $\alpha$  is maximum; this is important for applications requiring short pulsedwidths and is an instance of an MQW structure being preferable to an SQW structure. The penalty one pays for using an MQW LD is shown in equation (17) and again evident in figure 9; the MQW ( $N = 5$ ) threshold current density is five times greater than that for a comparable SQW ( $N = 1$ ) device. Thus, to realize the 68-percent modal gain increase of a five-well MQW LD, one must tolerate a fivefold increase in the threshold current density over an SQW LD.

Thus, the basic difference between SQW and MQW LDs is simple: for high-power and high-speed applications, MQW devices are preferred, and the penalty one pays for such a choice is a higher threshold current. During this research project we used both types of gain media to ensure that the optimum LD would be available for the optoelectronic attenuator experiments (discussed in sect. 5).

In addition to the choice of gain media, there is a choice of LD contact geometries for discrete devices: ridge waveguide and broad-area types are commonly used (shown in fig. 10). The essential difference between the two device geometries is as follows. In the ridge waveguide laser, a mesa is formed on the p-side of the wafer by etching a ridge, typically 0.7  $\mu\text{m}$  deep and 5 to 10  $\mu\text{m}$  wide. This ridge provides an index-guiding structure in the lateral direction; with proper design, only a single lateral mode can be supported in such a structure. The ridge also reduces the electrical capacitance of the contact to permit high-speed modulation. Unfortunately, since the LD gain volume is also reduced, this limits the amount of laser power from these devices. On the other hand, because broad-area lasers have a wide-stripe geometry (typically  $\geq 50 \mu\text{m}$ ), they can emit higher powers because of their relatively large gain volumes. However, multiple lateral modes result from the broad-stripe contact geometry, so that these lasers are of little interest to the communications industry (besides the highly astigmatic output beam, broad-area lasers lack modal purity for wavelength division multiplexing applications). Thus, ridge waveguide lasers are most useful for

**Figure 10. LD device fabricated using material structure of figure 8: (a) Broad-area structure. Broad-area stripe width,  $W$ , is as indicated. (b) Ridge-waveguide structure. Ridge width,  $W$ , is as indicated (typically 5 to 10  $\mu\text{m}$ ). Note that the ridge has been etched  $\sim 0.7 \mu\text{m}$  into the cladding layer.**



applications such as fiber-optic communications; but if high optical power levels are required, broad-area lasers are most useful.

Since our application requires high power levels and does not depend on modal purity for its operation, we chose to investigate broad-area lasers. Single discrete broad-area LDs were fabricated in our laboratory with pulsed output powers in excess of 1 W (for drive currents of 10 to 12 A). The device contact geometry can be segmented in such a way as to offset the higher capacitance associated with the broad contact geometry. In this case, the broad-area contact is divided into smaller sections that are electrically isolated. To illustrate, a two-section device is shown in figure 11. In this case, the gain section is electrically driven in the same way as a single-section device. However, if the second section is reverse biased with a dc voltage, then this section acts as a saturable absorber, which can be used to rapidly modulate the laser diode output. If a modulation signal is applied to the absorber section, it bleaches this section and leads to a modulated output (we show in sect. 3.3 that we can use this approach to Q-switch these devices). It is theoretically possible to achieve gigahertz modulation rates with this two-section LD scheme [54,62].

Using a numerical simulation code developed by Thedrez and Yang in the laboratory at the University of Maryland [57,58,63], we can predict the theoretical  $L/I$  curve for this type of device, as shown in figure 12. For this simulation, the stripe width was 300  $\mu\text{m}$ , with modulator and overall device lengths of 200  $\mu\text{m}$  and 1 mm, respectively. The modulator bias is 0, -4, and -8 V, as shown. Notice that increasing the second section bias simply shifts the  $L/I$  curve to higher current values (i.e., the threshold current is increased). This is caused by the increased intracavity loss introduced by the reverse bias on the second section. In the next section we show that this is an

Figure 11. Two-section LD geometry.

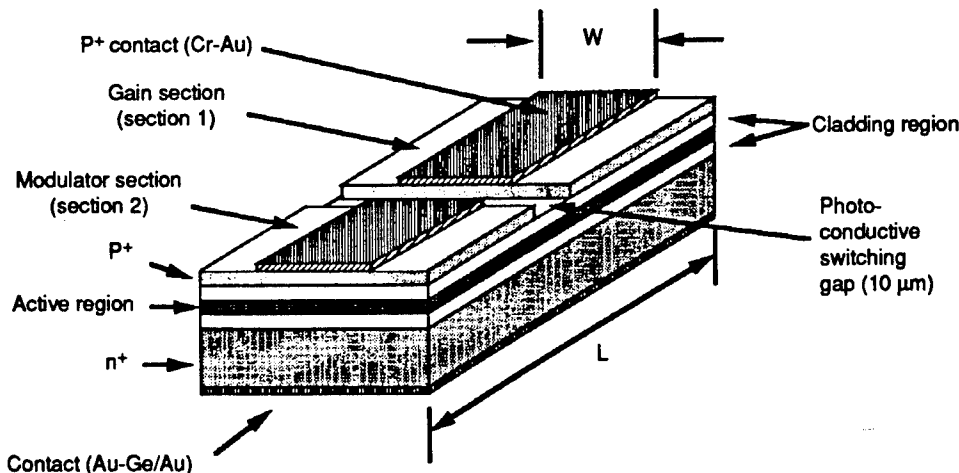
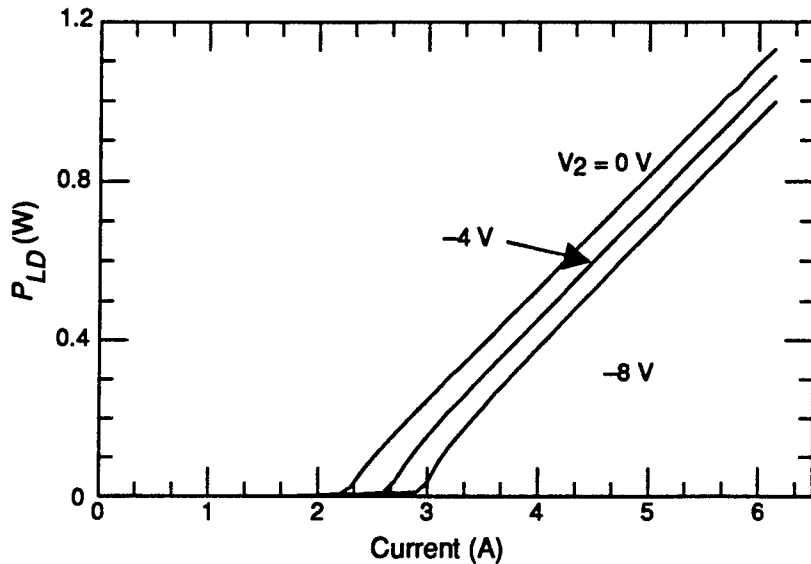


**Figure 12. Theoretical two-section LD  $L/I$  curve.**



accurate prediction of the measured performance of a two-section device of the same dimensions.

### 3.2 Laser Diode Design, Fabrication, and Performance

In support of the optically controlled attenuator project, many LDs were fabricated and tested at the University of Maryland. The material was grown at the Laboratory for Physical Sciences (LPS) under the Joint Program for Advanced Electronic Materials. Both SQW and MQW lasers, of the broad-area and ridge waveguide geometry types, were fabricated. In addition, one-, two-, and three-section devices were investigated, with the two-section broad-area LD used as the primary research tool for the photoconductive switching experiments discussed in later sections. Figure 13 is a photograph showing a cleaved broad-area LD bar. The stripe is 150  $\mu\text{m}$  wide and the bar was cleaved to achieve a cavity length of 450  $\mu\text{m}$ . Figure 14 is a photograph of a cleaved bar of laser devices showing two ridge waveguide devices; the device on the left is a three-section device, and the one on the right is a one-section device.

A typical optical power versus drive current plot ("L/I curve") is shown in figure 15 for a one-section SQW broad-area LD. The device was cleaved to form a 1-mm-long Fabry-Perot cavity with a contact width of 500  $\mu\text{m}$ . Figure 16 shows the spectral output of this device; its spectral peak is at 879.5 nm with a full-width half-maximum (FWHM) linewidth of less than 1 nm.

To achieve high-speed attenuator trigger rates, the modulation capabilities of a two-section device were assessed. Figure 17 shows the L/I curve of a two-section device as a function of the applied reverse

**Figure 13. Cleaved bar showing four 150- $\mu\text{m}$ -stripe one-section broad-area LDs.**

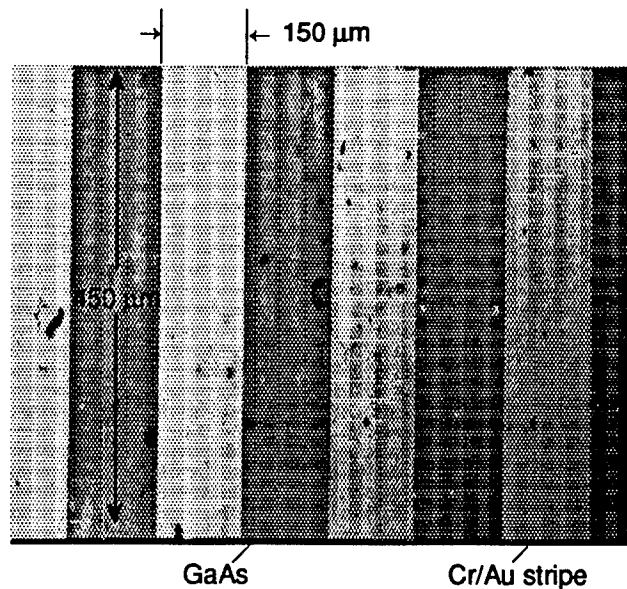


**Figure 14. Cleaved bar showing two ridge-waveguide LDs: three-section device (left) and one-section device (right).**

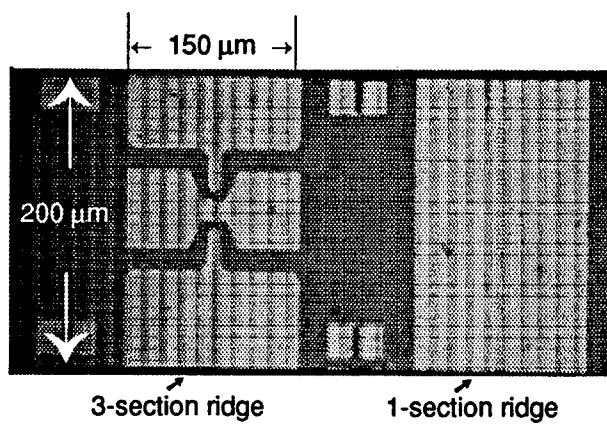


**Figure 15. One-section 500- $\mu\text{m}$  broad-area pulsed L/I curve. LD operation is in pulsed mode.**

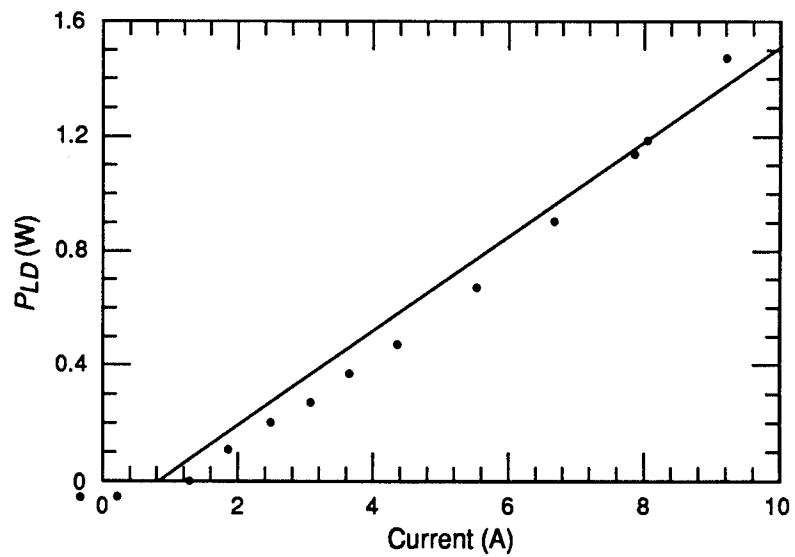


**Figure 16.**  
Corresponding  
spectral output of  
figure 15. LD is  
biased just above  
threshold.

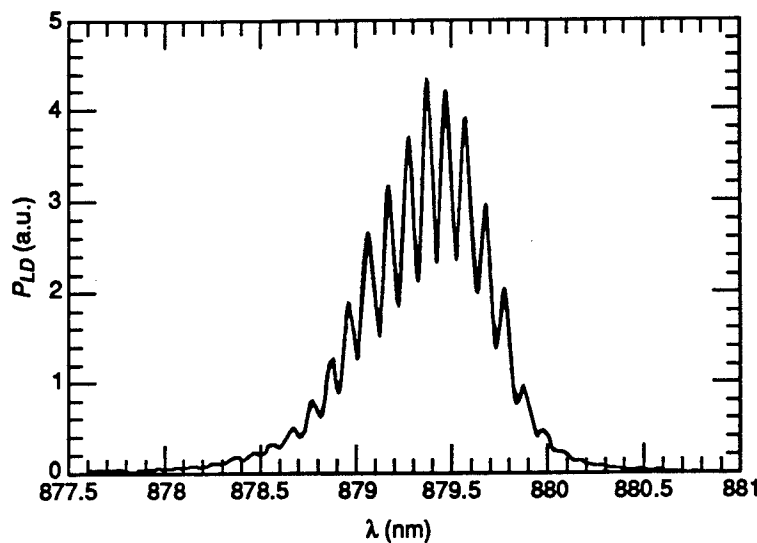
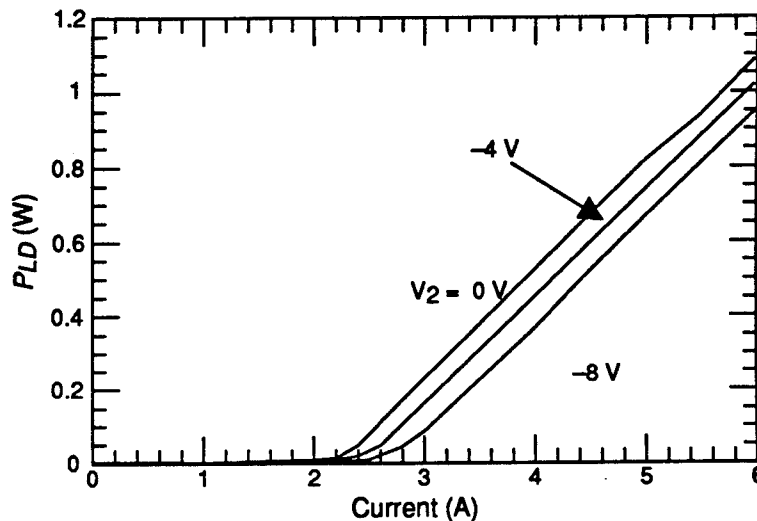


**Figure 17.** *L/I* curve of  
two-section 300- $\mu$ m-  
stripe LD versus  $V_2$ .  
Device length =  
1 mm.



bias on the absorber section. The stripe width is 300  $\mu$ m with a 200- $\mu$ m absorber section length. The overall device length is 1 mm. Because of the quantum-confined Stark effect [64], an increase of the modulator section voltage results in an increase in the device threshold current while the slope of the *L/I* curve is unaffected [65]. The amount of optical power that can be modulated (assuming a 100-percent modulation depth) is evident from figure 17: for a current of 3 A, the modulated optical output for  $V_2 = -8$  V is approximately 200 mW.

To investigate the turn-on speed of the two-section LD, we performed a simple timing experiment. The current pulse used to bias the gain section was synchronized with a shorter pulse, which can be used to forward-bias the otherwise reverse-biased second section. We then measured the time delay between the pulse used to

forward-bias the second section and the LD optical output pulse. With this scheme we measured a time delay of less than 500 ps, which indicates that two-section broad-area LDs can have sub-nanosecond turn-on times.

The near-field image of a 150- $\mu\text{m}$  broad-area laser output is shown in figure 18. Note that there are many lateral spatial modes evident in this image, as is expected from a broad-area laser of this size. Figure 19 is a photograph of a 300- $\mu\text{m}$ -stripe LD that was fabricated and packaged in our laboratory. The two SMA connectors are electrically connected to either the gain or modulator sections via gold-coated alumina contact pads and gold wire bonds. The LD is mounted by indium solder to a Au-plated OFHC Cu heat sink for improved ther-

**Figure 18. Image of 150- $\mu\text{m}$ -wide broad-area LD output on front facet showing fairly uniform lateral optical emission with some lateral mode structure.**

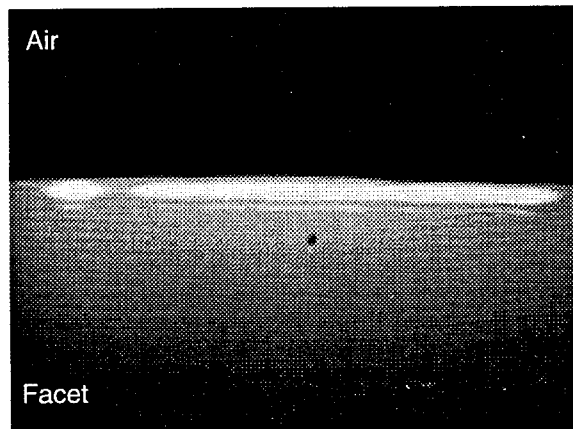
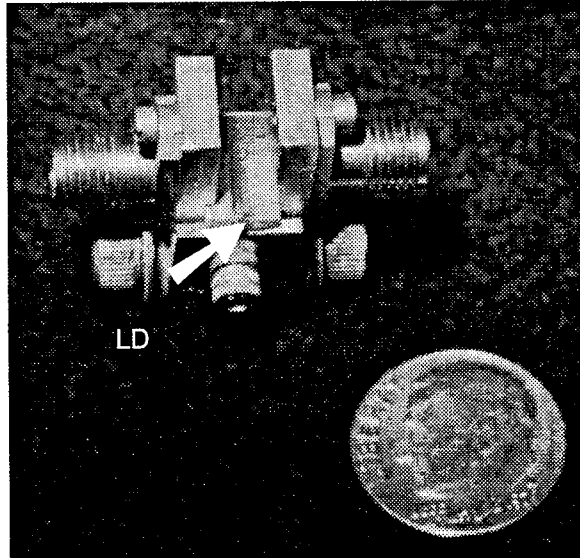


**Figure 19. Photograph of mounted 500- $\mu\text{m}$  broad-area LD.**



mal conductivity (front of mount shown in fig. 19). The laser mount is then placed on a thermo-electric (TE) cooler to provide temperature control for both wavelength tuning and to extend the device lifetime.

### 3.3 Optically Q-Switched Two-Section Laser Diode Experiment

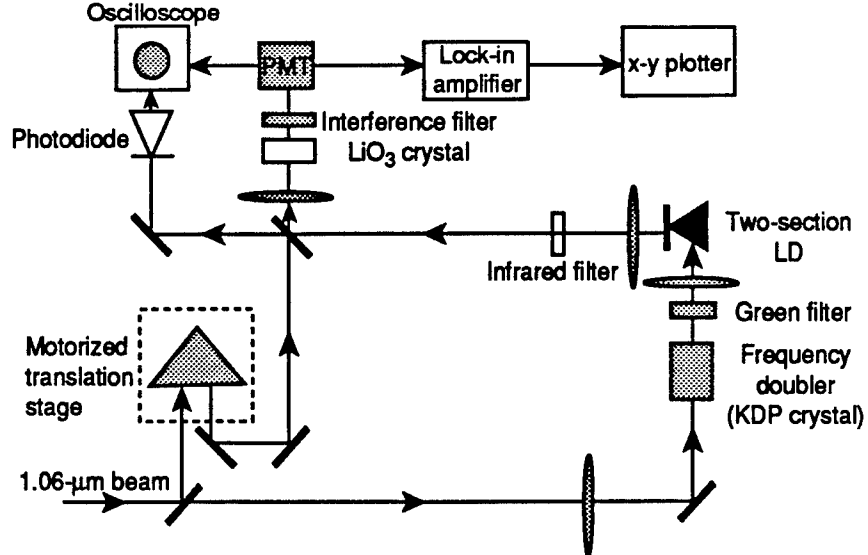
In section 3.2 it was noted that a two-section device can permit rapid LD turn-on times provided that a fast electrical signal is used to modulate the absorber section. The fundamental limit of this scheme is basically related to the difficulty in generating a fast (i.e., picosecond) electrical pulse to modulate the absorber section [66-68]. Using a high-power, mode-locked Nd:glass laser system [69], we assessed the fundamental dynamics of two-section broad-area LDs [57,58]. Using this experimental technique, we generated Q-switched pulses with greater than 6 W of peak power and pulsedwidths less than 30 ps from monolithic two-section lasers. For reference, with conventional gain-switching techniques these same devices produced less than 1 W of peak power in tens of nanoseconds.

Two broad-area LDs, devices *A* and *B*, were investigated. We used a lift-off technique to pattern the two electrodes and wet etched the cap layer to achieve electrical isolation (see fig. 10). The etched gap was 10  $\mu\text{m}$  for both devices. The stripe width for device *A* was 100  $\mu\text{m}$ , with a total length of 775  $\mu\text{m}$ . The length of the modulator section was 175  $\mu\text{m}$ . The active region was composed of a single 100  $\text{\AA}$  GaAs quantum well, separated from a 1000-nm  $\text{Al}_{0.4}\text{Ga}_{0.6}\text{As}$  cladding layer by a 150-nm graded region. The stripe width for device *B* was 300  $\mu\text{m}$ , with a 1-mm total length and a 200- $\mu\text{m}$  modulator section. An MQW active region was used, consisting of five 60- $\text{\AA}$  GaAs quantum wells separated by 80- $\text{\AA}$   $\text{Al}_{0.2}\text{Ga}_{0.8}\text{As}$  barriers, with a graded region of 200 nm and a cladding layer of 1000 nm.

The second section of the LD was reverse-biased and used as an optical modulator [55], while the first section provided gain. The gain section was pulsed with 100-ns-wide electrical pulses at a repetition rate of 500 Hz. We modulated the loss in the second (i.e., modulator) section by using the gap between the electrodes as a photoconductive switch [57,70].

Figure 20 shows a schematic diagram of the optically Q-switched LD experiment. Illuminating the gap with 527-nm light creates photocarriers that electrically short the two electrodes together. Since the gain section has a low impedance (typically a few ohms) in

**Figure 20. Optical Q-switching experimental setup.**



comparison with the reverse-biased modulator section, the creation of this near short circuit results in a drastic electrical change occurring mainly in the modulator section, which changes from a high to low absorption state in a time comparable to the illuminating pulsedwidth.

The light source for the switching pulse was a mode-locked Nd:glass laser coupled to a regenerative amplifier [69]. Pulses 10 ps wide were generated at a repetition rate of 500 Hz and could be compressed to 1 ps with a pair of gratings. The 1.054- $\mu$ m beam was doubled into the green and focused onto the switching gap. An average power of 32  $\mu$ W was available for switching with the 10-ps green pulse, with 25  $\mu$ W available from the 1-ps green pulse.

We measured the Q-switched pulsedwidth by mixing the diode and Nd:glass beams in a LiIO<sub>3</sub> crystal. When the 1-ps switching pulse is used, the cross-correlation of the two beams allows one to record the actual shape of the diode laser pulse directly [71], while a deconvolution step must be performed when the 10-ps pulse is used.

Results from the cross-correlation measurements are shown in figure 21(a) for device *A*, and figure 22(a) for device *B*. The modulator sections were reverse biased to the point where the LD output was quenched. For each value of applied voltage, the diode gain section was biased to just below threshold, since this arrangement proved to yield the best results. As can be seen from these figures, two different Q-switching behaviors were observed. Pulses from the type *B* laser show a train of pulses separated by the cavity round-trip time,  $\tau_{rt}$ . A large asymmetry (a fast-rising edge with a relatively slow decay time) was observed in all cases. Peak Q-switched power with

**Figure 21. Type A broad-area laser**  
**(a) experimental and**  
**(b) theoretical Q-**  
**switched pulse**  
**output. Bias current**  
**is 400 mA, and**  
**modulator section**  
**voltage is -5 V.**

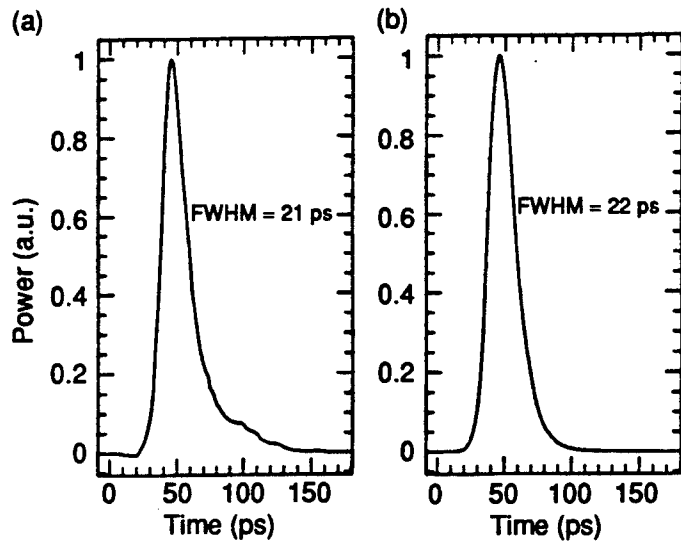
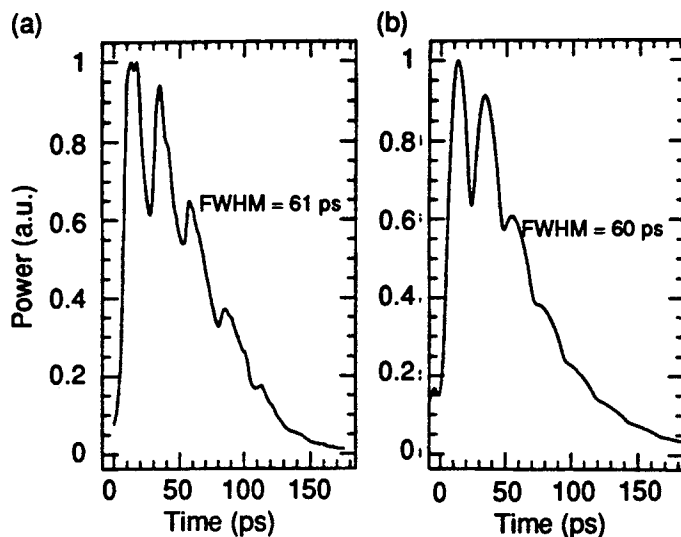


**Figure 22. Type B**  
**broad-area laser**  
**(a) experimental and**  
**(b) theoretical Q-**  
**switched pulse**  
**output. Bias current is**  
**3000 mA, and**  
**modulator section**  
**voltage is 0 V.**



the 10-ps switching pulse, which was deduced from average power measurements, was as high as 6 W.

The type A laser did not exhibit a distinct pulse train. Single-lobe pulses with FWHM values as low as 21 ps were measured. This is, to our knowledge, the shortest pulselength generated to date by a broad-area laser. Taking into account the pulselength of the 1.054- $\mu$ m pulse in the interpretation of the cross-correlation traces, we found that no noticeable reduction in pulselength was recorded during Q-switching with either the 10-ps or the 1-ps green pulse (this was also the case with the type B laser). Peak powers deduced from average power measurements were also as high as 6 W for measured pulselengths between 20 and 30 ps (for a device bias of 380 mA). To our knowledge, our method has achieved the largest pulse energy measured from a monolithic device in such a time scale.

A theoretical model that accurately predicts the Q-switched LD performance has been developed in our laboratory by Thedrez [57] and Yang [58]. Since we are interested in knowing if our results check with theoretical models, we present a comparison of theory with experiment, but do not give the details of the theory here. Figure 21(b) shows the theoretical Q-switched output pulse for the type A laser, and comparison with figure 21(a) shows excellent agreement. For the type B laser, the theoretical result is shown in figure 22(b), where again excellent theoretical agreement is demonstrated. What is novel about this theoretical curve is the fact that diode features that are on the order of  $\tau_{rt}$  have been accurately modeled. One can accurately model such features by using a set of traveling wave equations for the optical intensity and a rate equation for the gain, whereas in previous modeling techniques, a distributed loss approximation was assumed that our results have proven to be invalid for our experiment [57].

The features evident with the type B laser can be qualitatively explained as follows. When the optically Q-switched pulse is excited in the LD cavity, it oscillates in the cavity with a period equal to  $\tau_{rt}$ . If, after one round trip, the cavity gain is depleted, then the Q-switched pulse structure is similar to that displayed by the type A laser: a simple pulse shape without any additional features. However, if the Q-switched pulse has insufficient intensity to completely deplete the gain in the LD cavity, then additional pulses will experience gain and, upon being amplified by this gain, be observed at the LD output as features on the Q-switched pulse. As an illustration, the cavity length for the type B laser is 1 mm, which corresponds to a  $\tau_{rt}$  of  $\approx 12$  ps. As figure 22 shows, this value is in qualitative agreement with the observed periodicity of the Q-switched pulse features.

We have demonstrated operation at high powers (up to 6 W) and short pulsedwidths (as short as 21 ps) from discrete broad-area LDs. These results are important for the optoelectronic attenuator since this is a potential means for activating the attenuator with high-power optical pulses from a laser diode; the short pulsedwidth indicates that this can be done at a high repetition rate (the repetition rate is limited by the CPW-PCS PC carrier decay time and not the laser driver). We are continuing our research to demonstrate similar performance using gain switching, which differs from the Q-switching technique in that an electrical pulse is used to rapidly bias the gain section without the need for the optical switching pulse.

### 3.4 Laser Diode Microwave Impedance-Matching Transformer

In the last section we demonstrated that optically  $Q$ -switching a single two-section LD can be used to drastically increase the laser output power and reduce the pulselength. Obviously, this is a complicated method and if it is possible to improve the output power of LDs by more traditional techniques, then this should be tried. One of the biggest factors leading to poor LD efficiency is the simple fact that  $50\text{-}\Omega$  electrical drivers are typically used to activate the lasers, and these lasers generally have on-state impedances of 1 to  $5\ \Omega$ . Clearly, most of the electrical drive power is reflected from the LD by this large impedance mismatch and therefore wasted. The power transfer to a low-impedance device can be improved by the use of microwave matching techniques that are well covered in the literature [72]. Recently, similar techniques have been employed to match LDs to high-frequency drivers so that high-frequency modulation can be efficiently achieved [73,74]. These are traditionally narrow-bandwidth techniques, where the matched bandwidth is typically  $\leq 10$  percent of the modulation frequency (e.g., 1-GHz signals matched over 100-MHz bandwidth).

Fast-risetime current pulses on the order of 1 ns, with pulselengths of 50 to 100 ns, are used to turn on our LDs (the Fourier frequency content of these pulses is  $\leq 1$  GHz). In order to improve the overall efficiency of high-power LDs, we must match the gain section impedance over a broad bandwidth ( $\sim 1$  GHz), and this bandwidth covers frequencies from dc to 1 GHz. Therefore, we undertook to match the LD gain section from 300 MHz to 1 GHz using commercially available microwave design tools (Academy [75]). In our design, we assumed a resistive diode on-state impedance of  $5\ \Omega$  and permitted an in-band ripple of 0.5 dB. The impedance transformer design selected was a quarter-wave transformer, since this typically yields broad-band matching [72].

The LD microwave transformer (LDMT) electrical circuit schematic generated by Academy is shown in figure 23. Since we wanted to match low-frequency components, we used discrete lumped capacitors ( $C_1$  to  $C_4$  in the figure) to reduce the overall electrical length to 3.7 cm. The built-in Academy optimization routine was used to optimize the design, and the final microwave layout was generated (fig. 24). Figure 25 shows the calculated value of  $S_{11}$  for the LDMT and a reference  $50\text{-}\Omega$  microstrip line. Note that Academy predicts that we can improve the matching of a  $5\text{-}\Omega$  real impedance with the LDMT over a bandwidth of approximately 1 GHz, which is quite impressive, considering that this includes frequency components as low as 200 MHz.

**Figure 23. LDMT electrical schematic generated by Academy [75]. Lumped capacitors  $C_1$  (0.6 pF),  $C_2$  (12 pF),  $C_3$  (12 pF), and  $C_4$  (7.5 pF) reduce LDMT length from 5 to 3.7 cm. 5- $\Omega$  real impedance was assumed.**

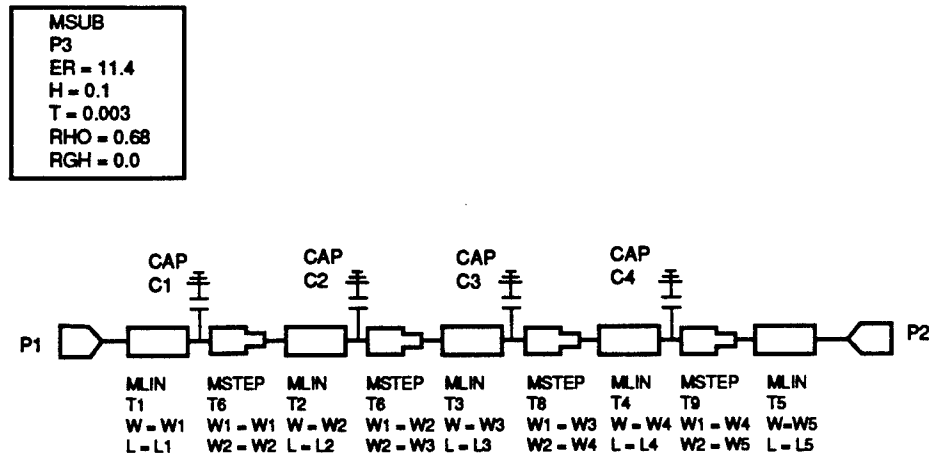


**Figure 24. LDMT microstrip layout generated by Academy [75]. Lumped capacitors,  $C_1$  to  $C_4$ , were soldered to ground where indicated. LD was wire-bonded to P2.**

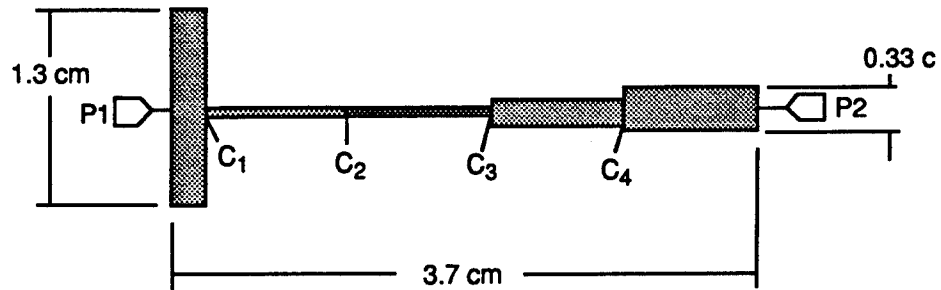
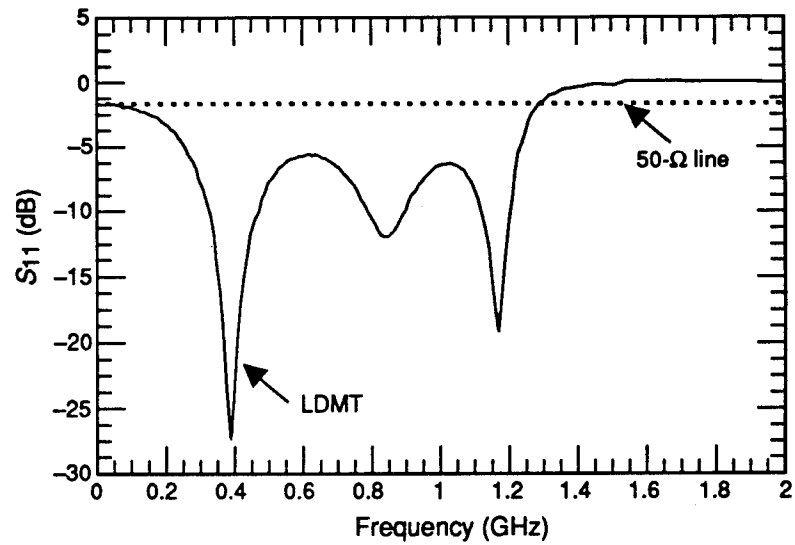


**Figure 25. Academy [75] prediction of reflected power,  $S_{11}$ , of LDMT and 50- $\Omega$  reference line, assuming 5- $\Omega$  real load impedance. Note that 1-GHz matched bandwidth is predicted.**



The LDMT was realized with microstrip line and fabricated on copper-clad Duroid 6010 [76]; a reference 50- $\Omega$  microstrip line was fabricated as well. A 100- $\mu\text{m}$ -stripe broad-area LD was then used in measuring the performance of both circuits. The laser was mounted on a suitable heat sink and then wire bonded to each of the circuits. Figure 26 shows the value of  $S_{11}$  measured on a scalar network analyzer (SNA). Note that the SNA data show that the LDMT improves the matching to the LD over a bandwidth of  $\approx 500$  MHz.

The discrepancy between the measured and calculated values is most likely due to two factors: the LD wire-bonds are highly inductive, and the real LD impedance is highly reactive (i.e., capacitive). To simplify our design, and since no data were available concerning the actual LD on-state impedance, we chose a 5- $\Omega$  real diode impedance as a first try. If the LD model can be adjusted to account for these two factors, an improvement over a 500-MHz bandwidth is expected.

Ultimately, to determine whether the LDMT can improve the diode performance, one must compare the  $L/I$  curves for the same laser being driven by both circuits. Figure 27 shows the measured result from such an experiment. Note that at a drive current of 175 mA, a 37-percent increase in the optical intensity has been achieved with the LDMT. This certainly proves that low-frequency, broad-bandwidth matching of LDs is a possible technique for improving overall LD efficiency.

One of the research goals outlined in the previous chapter was the need to develop an all-semiconductor-based optoelectronic attenuator that could be operated with minimum electrical power. If the  $L/I$

**Figure 26. Measured  $S_{11}$  of LDMT and 50- $\Omega$  reference line terminated with broad-area LD. Note that LD matching has been improved over 500-MHz bandwidth. Sharp peak on 50- $\Omega$  data is due to packaging resonance.**

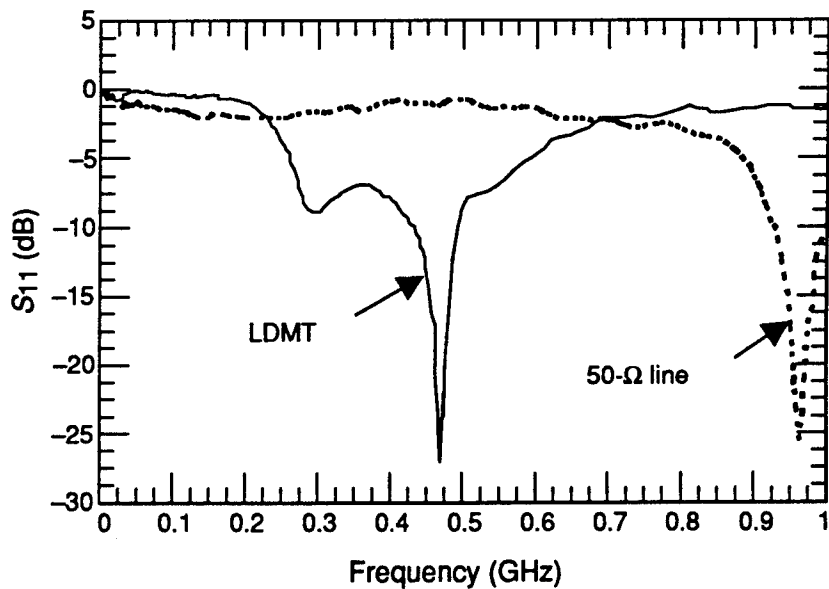
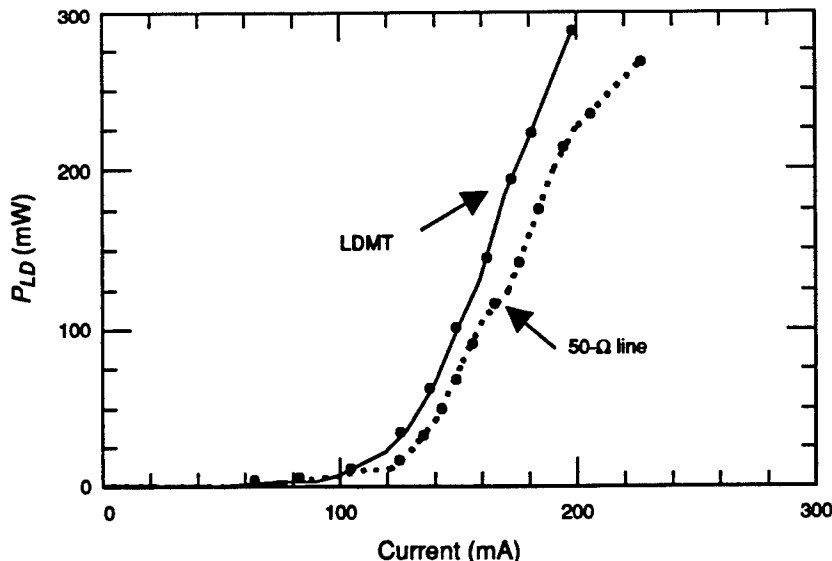


**Figure 27. Measured L/I curve using LDMT and 50- $\Omega$  reference line to drive same LD. Note: an increase of 37% in optical power, at 175 mA, has been achieved with LDMT. 100-ns pulses at 1-kHz pulse repetition frequency were used to drive laser.**



curve is improved by 37 percent for a fixed bias level, then the current required to achieve a given optical power level should therefore be reduced by this amount. Thus, this portion of the LD development effort is of extreme importance for the optoelectronic attenuator; the LDMT permits the use of MQW LDs since we can take advantage of the high gain (and therefore high output power) of these LDs while simultaneously reducing the electrical driver requirements to acceptable levels.

### 3.5 Summary

Several LD types (i.e. ridge waveguide, broad area, multiple section, SQW, MQW, etc) were fabricated and evaluated for use as the light source for the optically controlled attenuator. We have fabricated discrete broad-area LDs with peak optical powers on the order of 1 W, and Q-switched these same devices to increase the power to 6 W. In addition, these Q-switched results are believed to be the highest energy and shortest pulsedwidth results from discrete devices to date. We have demonstrated a microwave impedance matching transformer, the LDMT, and shown that the overall LD efficiency can be improved by as much as 37 percent for a fixed bias level.

Now that the optoelectronic attenuator control device, namely the semiconductor LD, has been developed, we will now describe the design, fabrication, and evaluation of the attenuation element.

## 4. Photoconductive Switches

Perhaps one of the simplest semiconductor devices is the bulk PC switch, which is made up of two metallic contacts placed on a PC substrate, such as a semiconductor wafer. Light then illuminates the intervening semiconductor material and is absorbed and converted into electron-hole pairs. Photoconductors can thus be used to convert optical energy into electrical signals.

These PC devices are commonly referred to as PC switches; applications for and the development of PC switches have been well covered in the literature by Lee [3,36]. When these devices are fabricated in such a way as to support high-speed signal generation, modulation, and propagation, then these types of PC switches can be used in microwave systems. Many examples of such high-speed PC devices and systems applications may be found in the literature [3]. In particular, the fabrication of planar microwave transmission-line structures onto PC substrate materials yields high-speed PC switches that are embedded in the microwave structure [77].

Since a treatment of the basic physics of PC switches is essential to the optimization of the optoelectronic attenuator, we present the relevant physics of PC switches at the beginning of this section. Next, we review planar microwave transmission-line structures and discuss their potential usefulness with regard to the optoelectronic attenuator. Finally, we describe the actual design, fabrication, and characterization of GaAs and silicon coplanar waveguide-PC switches (CPW-PCSs) that will be used for constructing the hybrid optoelectronic attenuator.

### 4.1 Photoconductive Switch Physics

The theory describing the dynamic PC switch resistance was developed by C. H. Lee [35]. The PC switch on-state resistance,  $R_{on}$ , of a device whose operation is based on an optically induced conductivity change (i.e., "conductive mode" of operation) is given by

$$R_{on} = l_{gap}^2 / q\mu N , \quad (18)$$

where  $l_{gap}$  is the PC switch electrode spacing,  $N$  is the total number of photo-induced electrons generated by the optical pulse,  $q$  is the electronic charge, and  $\mu$  is the electron mobility. The electron mobility of bulk GaAs at room temperature is  $\approx 8800 \text{ cm}^2/\text{V}\cdot\text{s}$ , while the surface mobility can be as low as  $1000 \text{ cm}^2/\text{V}\cdot\text{s}$ . Therefore, the path taken by the photocurrent is an important PC switch consideration.

Work by Funk and others [36] has shown that PC switches can handle large currents and be triggered in picoseconds. The question is, can this be done with a conventional (or new) laser diode design? The laser radiation has a wavelength,  $\lambda$ , corresponding to a photon energy ( $E = h\nu = hc/\lambda$ ) that satisfies one of the following:

- (1) Photon energy,  $h\nu$ , is greater than the switch material band-gap energy, i.e.,  $h\nu > E_g$
- (2) Photon energy is less than the band-gap energy, but greater than the energy difference between a suitable impurity level and the conduction band, i.e.,  $E_t \leq h\nu \leq E_g$
- (3) Photon energy is less than the band-gap energy and no suitable impurity levels exist, i.e.,  $E_g > h\nu$ .

The first absorption mechanism is referred to as intrinsic photon absorption [78]; a single photon has sufficient energy to promote a valence electron into the conduction band, thus generating an electron-hole pair in the PC switch. This is the most efficient absorption mechanism, and as a result, the absorption depth in the semiconductor is very shallow (the photon absorption coefficient,  $\alpha$ , varies exponentially with the distance from the surface). A PC switch using this absorption mechanism is usually fabricated with both contacts on the same semiconductor surface, and is thus referred to as a surface switch (since the conductive path is parallel to the switch surface).

Designs based on the second type of absorption mechanism rely on the presence of impurities within the semiconductor crystal; these impurities, and/or traps, mediate the absorption of the incident photons. Since the energy levels of these traps are within the semiconductor band-gap, the absorption is more uniformly distributed within the semiconductor bulk than was the case for intrinsic absorption. This absorption mechanism can result in fairly efficient photon to electron-hole pair conversion, depending on the extrinsic impurity, again since the absorption is more uniformly distributed through the bulk crystal. Thus, PC switches that rely on this absorption mechanism have contacts fabricated on opposing sides of the semiconductor crystal; this type of PC switch is referred to as a bulk PC switch. This absorption mechanism is usually referred to as extrinsic absorption [78].

The third type of absorption is referred to as two-photon absorption; the energy of a single photon is insufficient to promote electron transfer, and therefore two photons must use their combined energy to generate an electron-hole pair. The absorption of photons in this

case is non-linear (dependent on optical intensity squared) and is thus somewhat inefficient, especially for low-intensity lasers such as the semiconductor LD. PC switches using this technique are also called bulk switches since the photon absorption is also uniformly distributed in the semiconductor bulk.

Therefore, the relevant absorption mechanism is of fundamental importance, since both the switch and laser source chosen are determined by this factor. If intrinsic photon absorption (type 1) is used ( $h\nu > E_g$ ), then the depth at which the photons are absorbed by the material is very shallow. For pulsed-power applications, surface switches have demonstrated a minimum on-state resistance value of  $\geq 200 \Omega$  [79]. However, these are large devices (1- to 5-mm gap spacing); the lower resistance limit for surface switches with gap lengths on the order of microns may be much less.

Since the crystal structure in the bulk is generally superior to that of the surface (because of surface defects and recombination centers, which result in a lower surface mobility), bulk PC switches can, in principle, achieve much lower dynamic resistances, which may be as low as  $1 \Omega$  [36]. Since two-photon absorption (type 3) is inefficient, the most suitable bulk absorption mechanism for the optoelectronic attenuator is extrinsic absorption (type 2); i.e.,  $E_t \leq h\nu \leq E_g$ . This is especially true if the LD and PC switch are made from the same material ( $h\nu \approx E_g$ ). If a quantum well laser is used, then the laser energy can be designed to meet the laser energy conditions specified for both types 1 and 2.

Therefore, trap-mediated (extrinsic) absorption is believed to be the best choice for an all-GaAs optoelectronic attenuator, provided that a suitable trap in the bulk material is used. One likely candidate is the well-known EL2 trap in GaAs [80], with a corresponding  $\Delta E = 0.83$  eV ( $\Delta E = E_c - E_{trap}$ ). PC switches have been successfully fabricated with this trap [81], and since this level is always present in GaAs, no special doping of the substrate is required.

If the optoelectronic attenuator uses a silicon PC switch, then a surface PC switch (type 1) can be used, since the surface quality of passivated Si is much better than that of GaAs. In addition, the lower band-gap of Si ( $\approx 1.1$  eV) suggests that efficient surface switching is possible with an AlGaAs LD, since  $h\nu > E_g$ . One other reason to try using an Si PC switch in the attenuator is worth mentioning now.

A PC switch characteristic of importance is the PC carrier recombination lifetime,  $\tau_r$ . For GaAs,  $\tau_r$  is  $\approx 1$  to 5 ns [82], while in silicon the lifetime is  $\approx 1$  to 10  $\mu$ s [49]. This is an important material property because the lifetime determines how often the PC switch must re-

absorb photons for the laser to maintain a constant density of photocarriers,  $N$ , and it also determines the speed at which the switch can open. For example, a 100-ns optical pulse is incident on both a GaAs and Si PC switch. Every 1 to 5 ns, the GaAs PC switch loses  $1/e$  of its photocarriers to recombination; these carriers must be replenished by the laser to maintain a constant level of photoconductivity. On the other hand, the Si switch does not lose carriers as quickly, so additional carriers are continuously created, thus providing more photocarriers for conduction. This phenomenon is usually referred to as photoconductive gain [83], expressed as

$$G_{on} = \tau_r / \tau_t , \quad (19)$$

where  $\tau_r$  is the PC carrier lifetime and  $\tau_t$  is the carrier transit time;  $\tau_t = l_{gap}/(\mu E)$ , where  $\mu$  is the carrier mobility,  $E$  is the electric field ( $E = V/l_{gap}$ ), and  $l_{gap}$  is the PC switch gap. Thus, if the carrier transit time is shorter than the PC carrier lifetime (i.e.,  $\tau_t < \tau_r$ ), then  $G_{on}$  can exceed one, and the PC switch can be said to have an effective PC gain. For the Si:CPW-PCS, if  $\tau_r = 1 \mu\text{s}$ ,  $V = 1 \text{ V}$ ,  $\mu = 1400 \text{ cm}^2/\text{V}\cdot\text{s}$ , and  $l_{gap} = 10 \mu\text{m}$ , then  $G_{on} \approx 1400$ .

Therefore, although GaAs is the preferred material for the CPW-PCS because of its compatibility with standard microwave integrated circuits, silicon may be the best choice for demonstration of the opto-electronic attenuator concept. If this proves to be valid, then the lifetime in GaAs can be increased by techniques that use superlattice structures [84,85]. It was for these reasons that both GaAs and Si CPW-PCSs were fabricated and characterized during this research project.

## 4.2 Planar Microwave Transmission Lines

Photoconductivity can be thought of as the primary "intrinsic" characteristic of the PC medium, where as long as the medium is a photoconductor, one can expect the medium to behave as discussed: above  $E_g$  radiation yields intrinsic photon absorption, which in turn generates PC carriers in a shallow depth from the PC switch surface. Conversely, below  $E_g$  radiation yields absorption depths that may include the entire crystal thickness, and this type of absorption may be due to various extrinsic mechanisms, but impurity-level-mediated absorption is the usual situation.

The next issue is how to take such a medium and fabricate a practical PC switch. The most important element in such a device is the electrical contact structure. If two contacts are placed on the same semiconductor surface and a photocurrent is to flow between them,

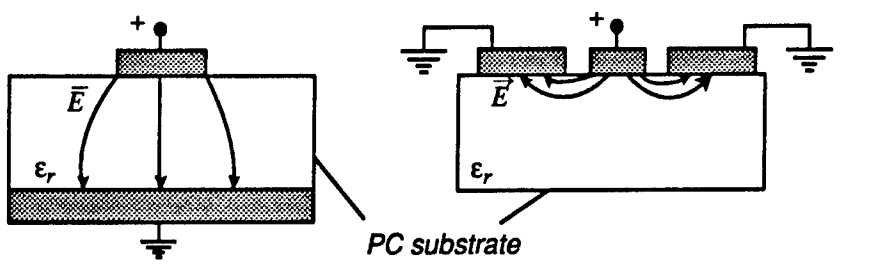
the laser chosen would typically emit radiation that is above  $E_g$ , since this would create PC carriers between the contacts. However, if the contacts are placed on opposite sides of a semiconductor crystal, then the laser chosen would emit radiation below  $E_g$  so that bulk PC carriers would be injected between the contacts. Of course, this is not always the case, since effects such as surface recombination may dictate that radiation below  $E_g$  should be used even for surface switches.

In addition to these considerations, the contact geometry dictates the type of application for which the PC switch can be used. The contact (or switch) gap,  $L$ , is also critical; if  $L$  is too small, then a large voltage cannot be "held off" by the PC switch, and if  $L$  is too big, then a large amount of optical energy is required to close the PC switch. This is perhaps the most important consideration in PC switch design; it is obvious what choice must be made for a particular application ("high-speed" implies a surface switch with a small gap, "high power" implies a bulk switch with a large gap, etc).

Since the objective of this research is to optically control a microwave signal with a laser light source, it is reasonable to assume that it is best to use a contact geometry that is compatible with microwave devices. Thus, any planar (i.e., parallel to the semiconductor surface) transmission-line geometry that can support traveling electromagnetic waves in the microwave portion of the frequency spectrum is acceptable. An excellent summary of the most technologically important planar microwave transmission lines is given by Rivera and Itoh [86]. An excellent compilation of the relevant planar transmission-line analyses has been edited by Itoh [87].

As an illustration of the importance of contact geometry and laser wavelength on a microwave PC switch design, figure 28 compares two microwave transmission line types that have been fabricated on a PC substrate, such as GaAs or Si. The figure shows the important differences as they affect microwave PC switch design: The micro-

**Figure 28. Comparison between microstrip line (left) and CPW (right). Electric field lines are as shown; wave propagation is perpendicular to page. Note that carriers travel through bulk in microstrip PC switch and on surface in CPW-PCS.**



$\epsilon_r$  = relative permittivity    $\blacksquare$  = metallization    $E$  denotes electric field lines

strip PC switch requires radiation below  $E_g$  so that carriers are generated between the center (i.e., top) conductor and the integral ground plane. The CPW-PCS requires radiation above  $E_g$  so that carriers are created on the surface between the coplanar strips.

Since our goal is to demonstrate a hybrid optoelectronic attenuator, meaning that discrete devices are to be configured with free-space and/or optical fiber components, then the CPW-PCS is naturally the best choice. There are other planar structures where both contacts reside on the surface, such as coplanar strip line and slot line, but these geometries are either more difficult to realize or provide less electromagnetic interference protection [88]. In addition, CPW can be operated at higher frequencies than these other structures [89].

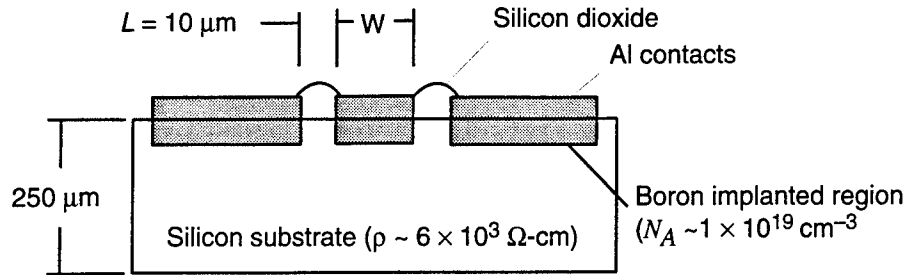
### 4.3 CPW-PCS Design, Fabrication, and Evaluation

The coplanar transmission-line geometry facilitates the use of broad-area LDs that can be easily focused onto the gap(s) between the coplanar conductors. Both Si and GaAs can be used as the substrate material, with the primary difference being the carrier recombination lifetime of 5 ns for GaAs and 10  $\mu$ s for Si. We designed a coplanar waveguide transmission line for high-speed applications using standard microwave design tools [90]. The characteristic impedance was designed to be 50  $\Omega$ , with the spacing between the center contact and the two outer contacts being 5, 10, or 20  $\mu$ m.

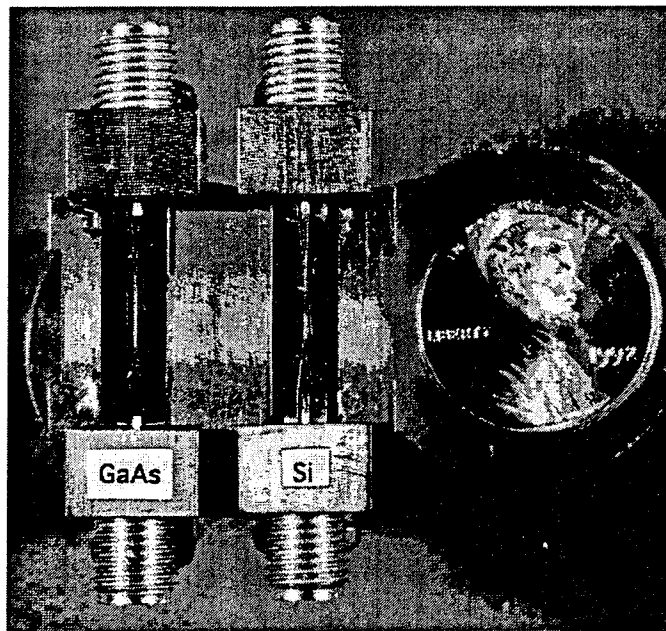
The GaAs:CPW-PCS design and fabrication has been reported separately [91]. Figure 29 shows a cross section of the Si:CPW-PCS that was used to form the hybrid attenuator circuit discussed in section 5. For ohmic contact to be achieved to the high resistivity substrate ( $\rho_{Si} \geq 6 \times 10^3 \Omega\text{-cm}$ ), the contact region was ion implanted with boron, which creates a P<sup>++</sup> region. Aluminum contacts were then deposited onto the ion-implanted regions to form the coplanar waveguide structure. Current-voltage measurements indicate that ohmic contact to the substrate was indeed achieved.

Figure 30 shows two mounted GaAs and Si:CPW-PCS devices. So that both the GaAs and Si:CPW-PCS would be properly connected into a hybrid attenuator circuit, the coplanar structure was flared to permit connection via an SMA connector. The W/L ratio was kept constant so that a 50- $\Omega$  characteristic impedance was maintained at the design frequency of 3 GHz. Consequently, the overall device length was 1.6 cm, resulting in a large parasitic center conductor resistance (~40 and ~60  $\Omega$  for the GaAs and Si devices, respectively). Fortunately this parasitic resistance would not be present in an operational device, since the device length need only be equal to the laser spot size.

**Figure 29. Schematic view of Si:CPW-PCS.** Total device length is 1.6 cm.  $R_{\text{dark}} \approx 13 \text{ k}\Omega$  achieved for  $L = 10 \mu\text{m}$ . Gap regions passivated with 4000 Å of  $\text{SiO}_2$ .



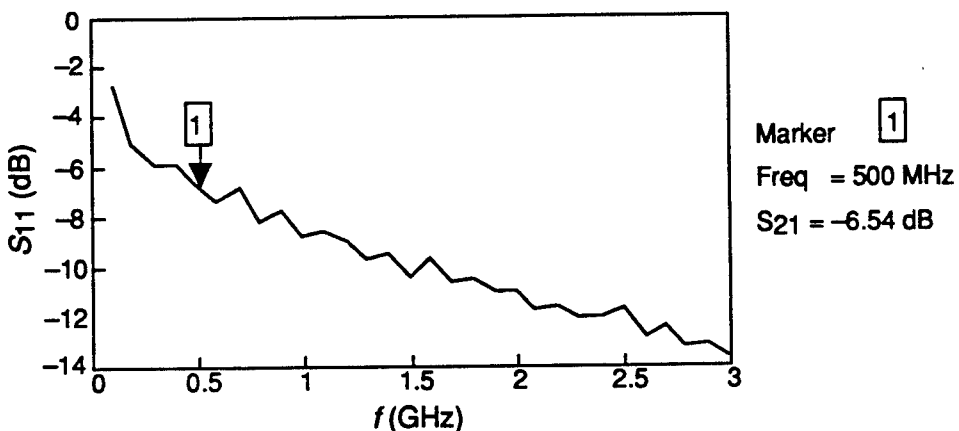
**Figure 30. Mounted GaAs (left) and Si (right) CPW-PCS devices.  $L = 50 \mu\text{m}$ , overall length = 1.6 cm.**



#### 4.4 CPW-PCS Electrical and Optical Characterization

The first step in the characterization of the CPW-PCS devices is to measure their microwave performance. A scalar network analyzer (SNA) was used to measure the insertion loss in the off-state (see fig. 31 for the Si:CPW-PCS) as a function of frequency. The Si:CPW-PCS displayed a high level of insertion loss (~6.5 dB at 500 MHz). The CPW-PCS design assumed a substrate thickness of 500  $\mu\text{m}$  and a dielectric constant of 13.1, which are both values used to design the GaAs:CPW-PCS [91]. Since the high-resistivity Si substrate was only 250  $\mu\text{m}$  thick, and Si has a lower dielectric constant (11.7), the increased insertion loss in the Si:CPW-PCS is not unexpected. Fortunately, all the optoelectronic attenuator experiments are unaffected by these values of insertion loss, since it is the relative increase in on-state attenuation that is important. In addition, when the high level of dc resistance is accounted for, the Si:CPW-PCS insertion loss is ~4 dB, which is acceptable for this investigation.

**Figure 31. Measured dark  $S_{21}$  of Si:CPW-PCS. Note that insertion loss is 6.5 dB at 500 MHz.**



One of the most important characterization measurements for PC switches is that of the PC carrier lifetime (which, of course, indicates whether the PC switch is functioning properly). This measurement can be done with the simple dc circuit shown in figure 32. In this circuit, the reference (or charging resistor, as it is referred to in the pulsed power community) is used to set a current reference across the oscilloscope load,  $R_S$ , which is  $50\ \Omega$ . A dc bias, typically a few volts, is applied to the circuit, and one measures the decrease in the voltage across the load that occurs when the PC switch is illuminated with laser energy. The recovery time of the voltage drop is used to determine the PC carrier lifetime.

The PC carrier lifetimes are shown in figure 33 for the Si:CPW-PCS, where this time only the PC response is shown. Part (a) of the figure shows the measured lifetime in the IR ( $\lambda = 1.054\ \mu\text{m}$ ) (a 500-MHz rf waveform was also propagating through the circuit—hence the broad line width) and in the red ( $\lambda = 0.797\ \mu\text{m}$ ). In this case, we can estimate the bulk and surface PC carrier recombination lifetimes to be  $\sim 2\ \mu\text{s}$  and  $350\ \text{ns}$ , respectively. These rather long lifetime values are consistent with the fact that the Si:CPW-PCS is fabricated on very pure silicon ( $\rho \sim 6 \times 10^3\ \Omega\cdot\text{cm}$ ). However, because of the indirect band-gap of Si, the  $\alpha$  for Si at these wavelengths is still an order of magnitude less than that for GaAs, even though this radiation is considered to be “above band-gap” [92].

#### 4.5 Summary

As this section shows, the high-speed microwave PC switches for the optoelectronic attenuator should be fabricated using a coplanar waveguide geometry. For surface switching, which is used in the hybrid optoelectronic attenuator, this geometry makes the most sense. For a monolithically integrated version of the attenuator, fabricating the high-speed PC switch with a microstrip transmission-line geometry would be more useful.

**Figure 32.**  
**Experimental setup**  
**used to measure**  
**CPW-PCS PC carrier**  
**lifetime,  $\tau_r$ .** Nd:glass  
**laser is shown as**  
**example; other lasers**  
**were used to measure**  
 **$\tau_r$  at various**  
**wavelengths.**

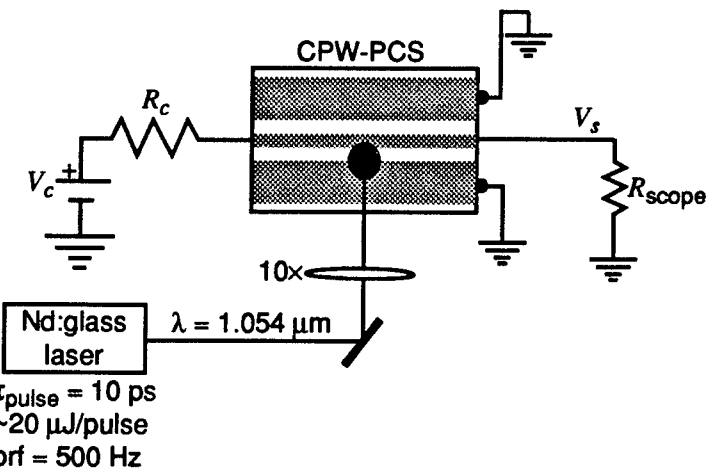
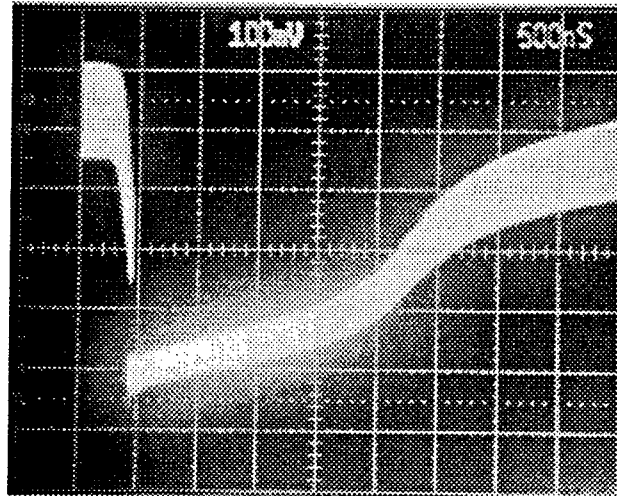
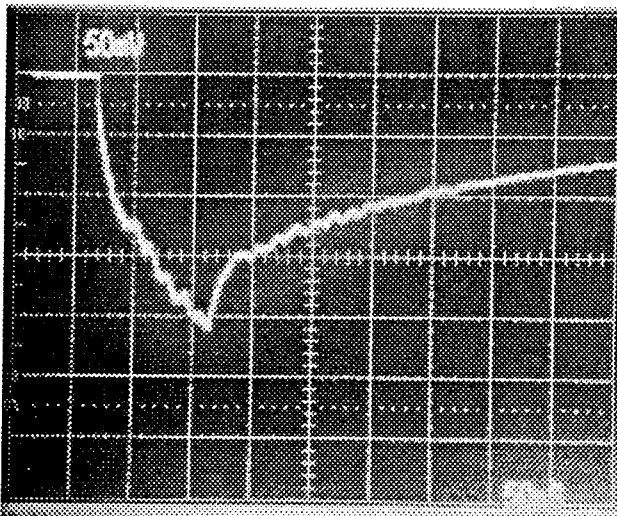


**Figure 33. Measured**  
**PC carrier lifetime,  $\tau_r$ ,**  
**of Si:CPW-PCS: (a)**  
**IR response (1.054  $\mu\text{m}$ ),**  
**where  $\tau_r, \text{bulk} \sim 2 \mu\text{s}$ ,**  
**and (b) red response**  
**(0.797  $\mu\text{m}$ ), where**  
 $\tau_r, \text{surface} \sim 350 \text{ ns}$ .



(a)



In this work, the optoelectronic attenuator was synthesized with what has been called the CPW-PCS, and this PC switch was fabricated on both GaAs and Si. The subsequent PC carrier lifetime measurements show why the CPW-PCS was fabricated on these materials: GaAs has a fast (~5 to 30 ns) response, while Si has a much slower (~350 ns to 2  $\mu$ s) response. GaAs is the preferred material since it is most compatible with microwave integrated circuits. However, Si is useful because it allows the laser power requirements to be lowered since the PC carriers are not lost to recombination as fast, and thus a higher level of PC conductivity can be maintained. Since GaAs NIPI structures can easily be grown by molecular beam epitaxy (MBE) techniques, the effective PC carrier recombination lifetime can be engineered to also be in the microsecond regime [93]. Thus the true rationale for the Si:CPW-PCS is clear: if this long-lifetime material can prove the feasibility of the optoelectronic attenuator concept, then further research can be conducted to get the GaAs:CPW-PCS to do the same.

Of course, the CPW-PCS must perform as a microwave transmission line in the off-state, and we have shown that this has been achieved. Unfortunately, there is a high level of insertion loss for the fabricated devices (~3 dB for the GaAs:CPW-PCS and ~6.5 dB for the Si:CPW-PCS). While this is a problem for integration of these devices into a real system, it does not affect the results presented in section 5, since all of the measurements in this work are relative ones, and therefore off-state parasitics are not a source of measurement error. In addition, improved fabrication techniques and/or electroplating will greatly reduce the off-state insertion loss. Finally, the device lengths are very long to permit ease of experimentation; thus, when all these factors are taken into account, we foresee no insertion loss problems for the optoelectronic attenuator.

## 5. Optoelectronic Attenuator Experiments

The use of optoelectronic techniques to control microwave circuits and systems continues to be an area of intense research and development [94–96]. Besides the inherent speed advantages of this approach, use of a laser to control multiple microwave circuits permits both a high degree of electrical isolation between the control signal and the microwave circuit, and timing precision that can easily be in the picosecond regime [3].

This section describes a hybrid optoelectronic attenuator scheme that is suitable for remotely controlling microwave integrated circuits. By optically illuminating the gap(s) between the center and outer conductor(s) of a coplanar microwave transmission line fabricated on a silicon substrate (i.e., the Si:CPW-PCS), we have demonstrated up to 45 dB of microwave attenuation at 1.7 GHz using only 143 mW of LD power. This is the highest level of attenuation reported to date for such an attenuator scheme [97,40,98]. Earlier work by Platte and Sauerer [98] used a similar technique with continuous wave (cw) optical illumination; however, they achieved a maximum attenuation of 1.8 dB.

How high-speed PC switches can be fabricated to support microwave signal propagation was discussed in section 4. Using the Si:CPW-PCS described in that section, we used a commercially available fiber-pigtailed LD to optically vary the attenuation of both rf and microwave signals through this high-speed PC switch. In section 2, two possible attenuation mechanisms were presented. The first was a reflective attenuation mechanism whereby the rf power is reflected by an optically induced impedance mismatch in the high-speed PC switch. The second was an absorptive attenuation mechanism whereby the rf signal is absorbed by a solid-state plasma that has also been optically created. Since either attenuation mechanism may be responsible for any observed rf attenuation, we conducted several experiments to determine which mechanism correctly accounts for any optically induced attenuation in the Si:CPW-PCS.

In addition, how well the optoelectronic attenuator performs, as a function of rf and/or microwave frequency, LD power, and LD beam profile, must also be determined so that the attenuator performance can be optimized; results of hybrid optoelectronic attenuator experiments performed with various laser diode sources, as a function of these control parameters, are presented in this section. The initial experiments were conducted with an rf generator operating at 500 MHz. We used several laser sources to attenuate the 500-MHz signal: a high-power mode-locked Nd:glass laser system

[99], the 300- $\mu$ m LD described in section 3 [91], a 1-cm linear AlGaAs LD array [94], and, finally, a fiber-pigtailed LD [100]. A maximum attenuation of the 500-MHz signal of 30 dB was achieved with the fiber-pigtailed laser for an optical power of 375 mW [43]. However, since we could measure only the signal attenuation through, and not the reflected power from, the Si:CPW-PCS, the exact nature of the absorption mechanism remained unclear.

Using a vector network analyzer (VNA) [101], we determined that the mechanism responsible for the attenuation of microwave signals in the optoelectronic attenuator was absorptive; up to 45 dB of attenuation was achieved with a fiber-pigtailed LD power of as little as 143 mW without an increase in the power reflected from the Si:CPW-PCS [102].

During the experiments involving the fiber-pigtailed LD, an important observation was made: the measured attenuation saturated at around 10 dB (at 500 MHz) when diffraction-limited spherical optics were used to focus the laser beam onto the PC switch gap. When the LD beam profile was expanded in one dimension (i.e., parallel to the Si:CPW-PCS structure), the level of attenuation increased by 20 dB above this saturated value [102]. The details of all these experiments are presented in this section. The first section discusses the mode-locked Nd:glass laser measurements, while the second section contains a description of the measured attenuation obtained with various LD sources. The 500-MHz pulsed rf attenuator data (measured with a high-speed analog oscilloscope), and cw microwave experimental results (measured with a VNA), both using the fiber-pigtailed LD, are given in the remaining two sections.

## 5.1 Nd:Glass Laser Measurements

We performed the first optoelectronic attenuator measurements using the same Nd:glass laser system [99] described in the literature to optically Q-switch a two-section broad-area LD [91], and in section 4.4 to measure the GaAs:CPW-PCS PC carrier lifetime. Figure 34 shows the experimental setup for the hybrid optoelectronic attenuator; the Nd:glass laser was operated at a 500-Hz pulse repetition rate with a pulse output energy of 20  $\mu$ J and an FWHM of 10 ps. A microscope objective 10 $\times$  was used to focus the Nd:glass laser beam onto the 10- $\mu$ m gap of the Si:CPW-PCS. The rf source frequency and power for these measurements were 500 MHz and +18 dBm, respectively.

Figure 35 shows a sample of the Si:CPW-PCS output waveform measured with a 1-GHz bandwidth oscilloscope (Tektronix 7104),

under these conditions. The attenuation,  $S_{21}$ , in decibels (dB), is defined in section 2, equation (3), for an arbitrary two-port network, as

$$S_{21}(dB) = 20\log_{10}\left(\frac{V_2}{V_1}\right) . \quad (20)$$

Here,  $V_2$  is the measured rf voltage when the switch is illuminated, and  $V_1$  is the rf voltage in the off-state. Using this relationship and the setup shown in figure 34, we found that the maximum measured attenuation of the 500-MHz signal in the Si:CPW-PCS was  $\sim -11$  dB.

Because of the rather short optical pulsewidth and long measurement time (10 ps compared with 1  $\mu$ s), the actual attenuation is most likely greater than this value. However, since our goal is to provide attenuation on longer time scales than 10 ps (i.e.,  $\sim 1$  ns), this result is not of much practical interest to us. In addition, since we wish to use LDs as the hybrid optoelectronic attenuator optical source (so that

**Figure 34.** Nd:glass laser experimental setup used to measure  $S_{21}$  of hybrid optoelectronic attenuator. Laser pulse energy = 20  $\mu$ J,  $f_{rf} = 500$  MHz at +18 dBm.

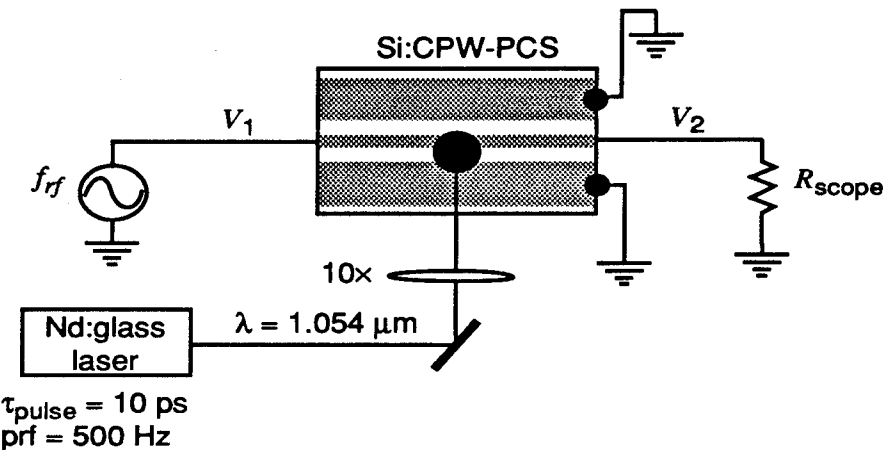
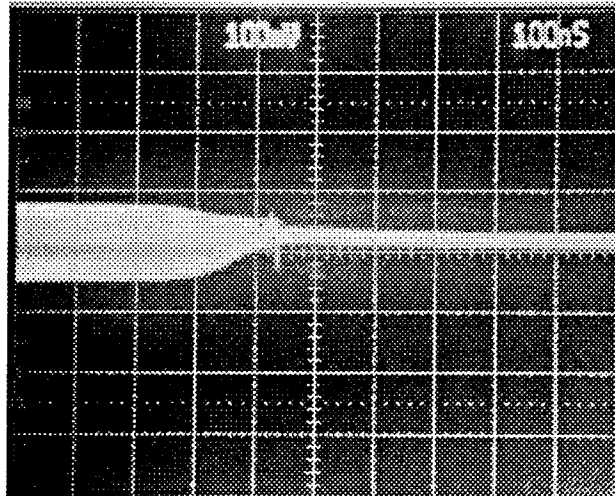


**Figure 35.** Optoelectronic attenuator data taken with Nd:glass laser system of figure 34,  $V_1 = 140$  mV,  $V_2 = 40$  mV,  $\Rightarrow |S_{21}| = 10.9$  dB.



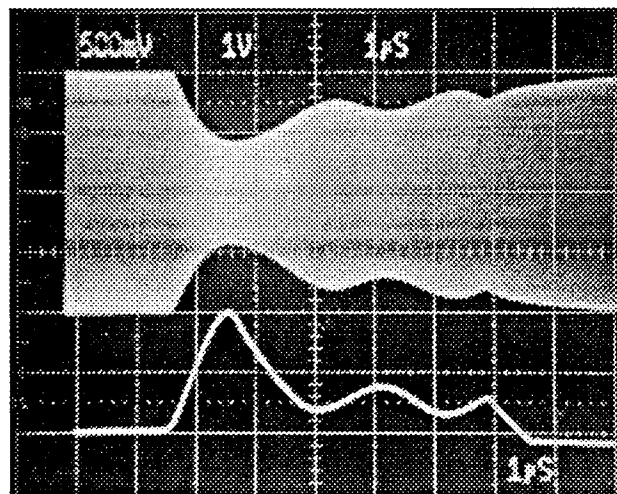
an all-semiconductor attenuator is demonstrated), the importance of this result is that it is the first step toward our goal of demonstrating an all semiconductor-based optoelectronic attenuator. The next section shows that this goal has been achieved with the 300- $\mu\text{m}$ -stripe broad-area LD described in the literature [91].

## 5.2 Broad-Area Laser Diode Measurements

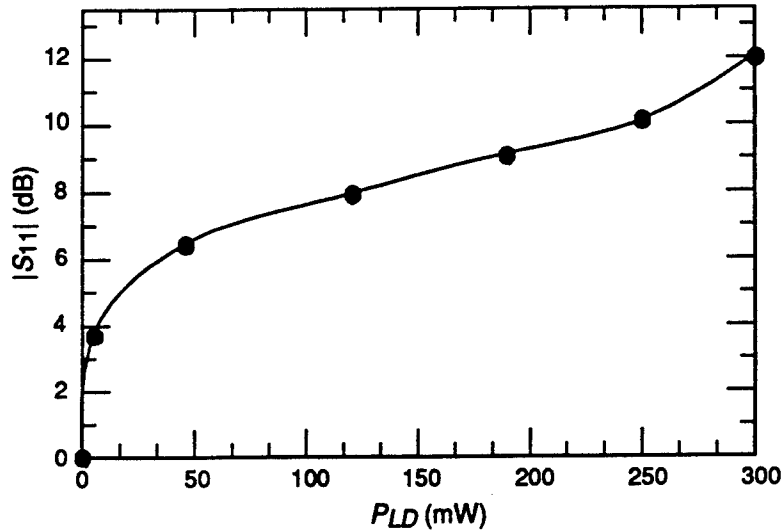
We measured the optoelectronic attenuator performance using the 300- $\mu\text{m}$ -stripe broad-area LD described earlier in section 3 (see fig. 29) [91] as the laser source in the hybrid optoelectronic attenuator (fig. 34). While we performed the same experiment described in the last section, the optically induced rf attenuation of a 500-MHz signal propagating through the Si:CPW-PCS was measured. A high-voltage 50- $\Omega$  pulser [103] was used to drive the 300- $\mu\text{m}$  LD. Figure 36 shows a typical example of the measured attenuation, where both the 500-MHz waveform (top trace) and corresponding LD current pulse (bottom trace) are displayed; an attenuation of 7.9 dB is shown. Note that the attenuator response roughly follows the LD pulse; thus, the Si:CPW-PCS may also be suitable as an optically controlled rf modulator.

Figure 37 shows the measured attenuation plotted as a function of LD peak power. Notice that the attenuation appears to level off at around 6 dB for a LD power near 50 mW. Unfortunately, the maximum attenuation measured with the LD was not much better than that measured with the Nd:glass laser system, which was around 10 dB; however, a significant reduction in the laser driver (in terms of cost, complexity, and size) has been achieved with the use of a single broad-area LD operating at modest output powers.

**Figure 36.**  
Optoelectronic attenuator data with 300- $\mu\text{m}$  broad-area LD. Top trace: 500-MHz signal envelope showing 7.9 dB of attenuation. Bottom trace: LD current pulse waveform. Note: response roughly follows laser pulse shape.



**Figure 37. Measured attenuation versus incident LD power using 300- $\mu\text{m}$  broad-area LD [91]. Note that attenuation levels off at  $\sim 11$  dB.**



Using the optical *Q*-switching technique described in the literature [47], we optically *Q*-switched the same 300- $\mu\text{m}$ , two-section LD in an attempt to increase the attenuation by increasing the LD output power. Unfortunately, the measured attenuation was less than 1 dB with this technique ( $|S_{21}| = 0.65$  dB). This poor result is, again, partly due to the short optical pulselength ( $\sim 60$  ps) compared with the long measurement time (1  $\mu\text{s}$ ), which is a difference of six orders of magnitude. Thus, the actual attenuation is most likely much larger than 0.65 dB. Although this result is unimpressive, it is the first reported PC switch measurement on such a *Q*-switched LD system. In an effort to improve this result, work is continuing in our laboratory to develop an all-electrical *Q*-switching scheme to improve this result for more general PC switching applications.

The next LD to be used in the optoelectronic attenuator was a 1-cm linear AlGaAs LD array provided by Arye Rosen of David Sarnoff Research Center, Princeton, NJ [94]. The array peak output power was 38 W at a wavelength of 804 nm. Unfortunately, the laser driver must deliver approximately 40 A of current to achieve this output power level. Using this LD array and a suitable voltage pulser [103] in place of the laser source of figure 34, we achieved 26 dB of rf (500 MHz) attenuation for an optical power of 5.35 W (see fig. 38). The LD pulselength for these measurements was 3  $\mu\text{s}$ . The measured attenuation as a function of LD array peak power is shown in figure 39. Again, the rf power and frequency were +18 dBm and 500 MHz, respectively. Notice that once again the measured attenuation appears to level off as the optical power is increased. Indeed, 20 dB of the maximum attenuation of 26 dB was achieved with approximately 1 W of LD power.

These results can be greatly improved since the spot size on the Si:CPW-PCS was approximately 100  $\mu\text{m} \times 1$  cm, and thus a signifi-

**Figure 38.** 1-cm LD array optoelectronic attenuator data showing 500-MHz signal envelope during laser activation. Data show an attenuation,  $|S_{21}|$ , of 26 dB.

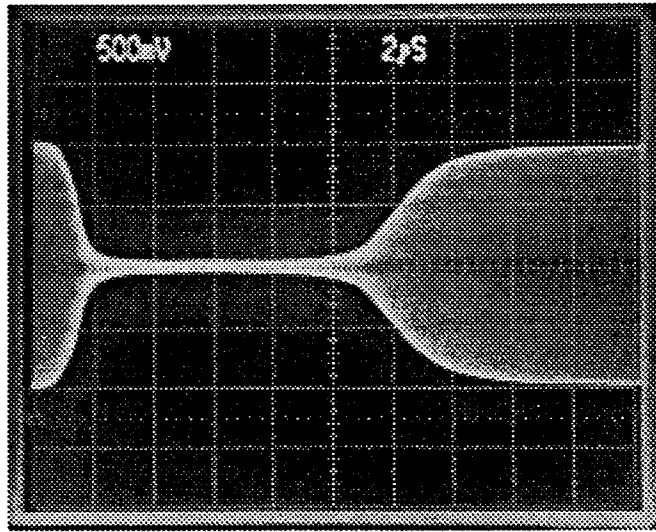
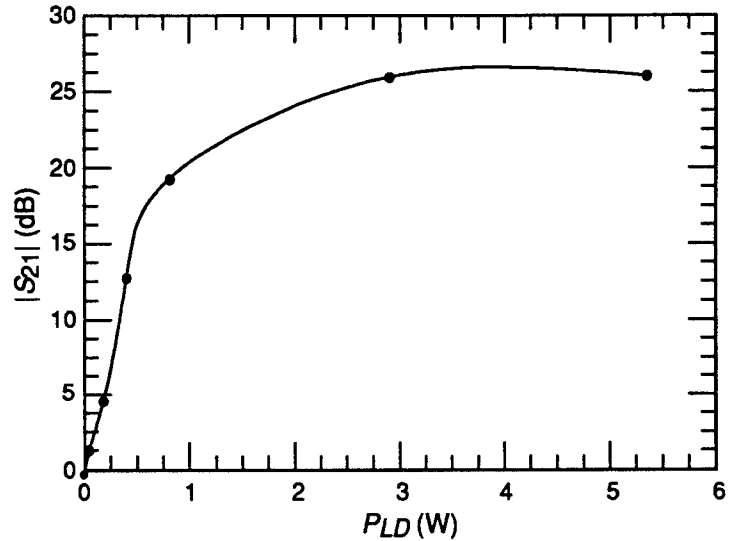


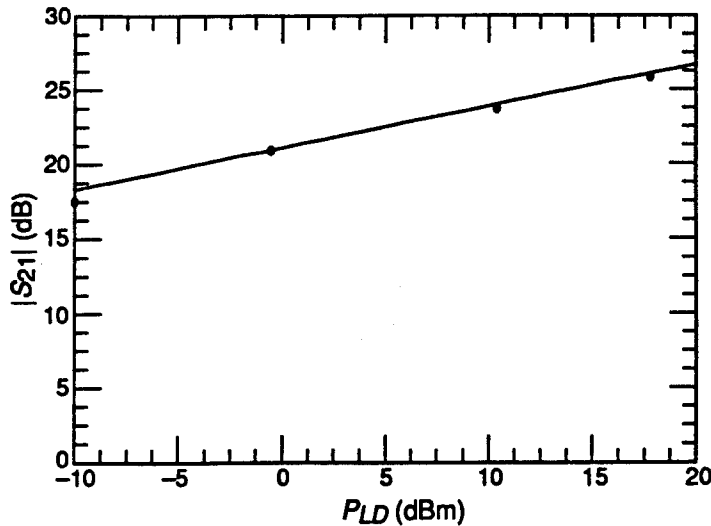
**Figure 39.** Measured attenuation versus incident LD power using 1-cm LD array. Note that attenuation levels off at  $\sim 26$  dB for  $\sim 5$  W of LD power; rf power = +18 dBm.



cant fraction of the laser power was wasted on both the switch contacts and on the substrate outside of the switching gap area. However, both gaps in the Si:CPW-PCS structure were illuminated with this LD array and, since these gaps are electrically connected in parallel, the effective on-state resistance may be quite low. Thus, this type of illumination may be the most suitable for the reflective attenuation scheme; however, uniform illumination of both PC switch gaps has been used by others [98] with rather disappointing results (less than 1.8 dB of attenuation was reported).

One important question remains: What contribution to the measured attenuation does the rf source power itself make? Figure 40 shows the optically induced attenuation for a fixed LD power of 5.35 W (i.e., maximum optical power of fig. 39) as a function of rf power. Note that the performance is roughly linear with a total variation of less than 7 dB for an rf power variation of three orders of

**Figure 40. Measured attenuation versus rf power using 1-cm LD array. Note that attenuation is approximately linear with rf power. Optical power = 5.35 W.**



magnitude. This shows that, although the rf power level affects the attenuator performance, the contribution is minimal compared with that of the laser source. In addition, for a microwave system operating with a decade variation in power, the optoelectronic attenuator performance variation with rf power would be less than 2 dB.

### 5.3 Fiber-Pigtailed LD Experiments—rf Voltage Measurements

In the last section we saw how semiconductor LDs can be used to optically induce 26 dB of rf attenuation with a laser peak power of ~5 W. As was observed, the 1-cm LD array output energy was spread over such a large area ( $100 \mu\text{m} \times 1 \text{ cm}$ ) that much of the available energy did not illuminate the PC switch gaps and thus was wasted. In the next two sections we show how a commercially available fiber-pigtailed LD can be used to greatly improve the hybrid attenuator performance while simultaneously reducing the LD peak power requirement from several watts to less than 150 mW. This section presents rf voltage measurements made with a 1-GHz bandwidth oscilloscope, which are identical measurements to those made earlier. In the next section, attenuator measurements made with a microwave VNA are described. Using the VNA, we determine the exact nature of the attenuation mechanism (either reflective, absorptive, or possibly a combination of both).

Figure 41 shows the experimental setup used to measure the Si:CPW-PCS hybrid optoelectronic attenuator performance with the fiber-pigtailed LD. A commercially available fiber-pigtailed LD [100] has replaced the other laser sources shown in figure 34 and described in section 4.2. For these rf voltage measurements, the LD was operated in pulsed mode with a pulselength and repetition frequency of  $200 \mu\text{s}$  and 500 Hz, respectively. Using a  $10\times$  micro-

scope objective to achieve a 10- $\mu\text{m}$  spot size on a single Si:CPW-PCS gap, we once again observed a leveling off of the attenuation as a function of LD power, as shown in figure 42. The rf source frequency and power were 500 MHz and +18 dBm, respectively.

Notice that the performance is still limited to about 10 dB even for this improved LD beam spot size, only this time we have reduced the required LD power to less than half a watt (375 mW). If the performance is effectively "saturating" because of the high optical intensity incident on the switch, then expansion of the beam with respect to the CPW-PCS geometry (i.e., lengthwise along the co-planar contacts) should show an increased level of attenuation.

A cylindrical lens was used to expand the beam to 10  $\mu\text{m} \times 2 \text{ mm}$ , and the resulting attenuation did in fact increase, as is also shown in

**Figure 41.** Fiber-pigtailed LD experimental setup used to measure  $S_{21}$  of hybrid optoelectronic attenuator; rf frequency = 500 MHz at +18 dBm.

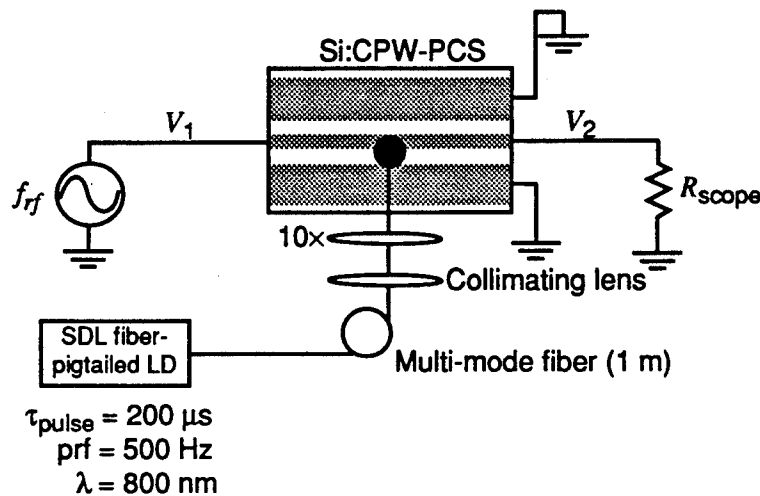


**Figure 42.** Measured attenuation versus incident LD power with fiber-pigtailed LD. Note:  $|S_{21}| = 10 \text{ dB}$  for  $A_{\text{spot}} = 10 \mu\text{m} \times 10 \mu\text{m}$ , and increases to 30 dB when spot is expanded to 10  $\mu\text{m} \times 2 \text{ mm}$ ;  $f_{rf} = 500 \text{ MHz}$ .

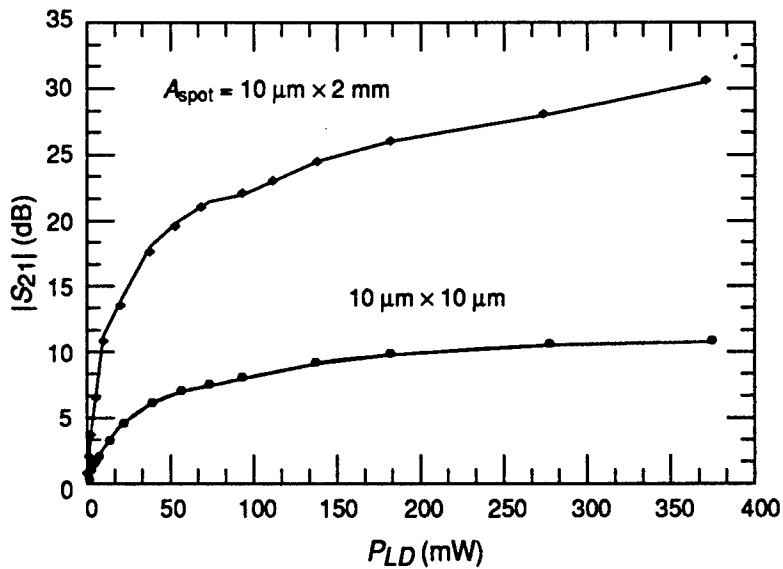


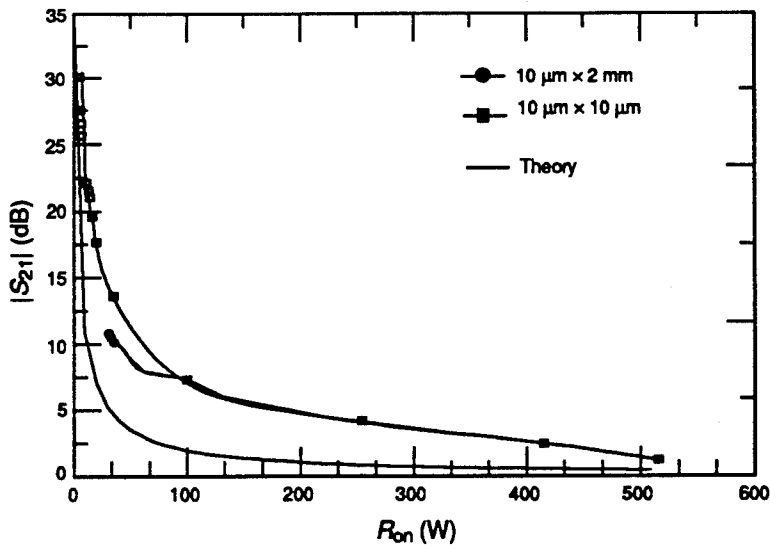
figure 42. The maximum attenuation for this optical arrangement was  $\sim 30$  dB, which is a 20-dB improvement over the case where only the microscope objective was used. Thus we have proven the opto-electronic attenuator concept using all semiconductor-based devices; it remains to see which attenuation mode is involved.

Before this point is discussed, the aforementioned saturation effect is worth commenting on. Since the rf frequency is 500 MHz, the guide wavelength  $\lambda_g$  ( $\lambda_g = \lambda/n$ , where  $n = 3.42$  is the refractive index of silicon) within the Si:CPW-PCS is approximately 17.5 cm. Since this is much larger than the Si:CPW-PCS itself (1.6 cm total length), it is hard to imagine that the increased attenuation measured with the expanded beam is due to any distributed resistance effects. If the correct attenuation mechanism is plasma absorption, then it is also difficult to see how increasing the plasma length while simultaneously drastically reducing the plasma density could yield an increase in  $S_{21}$  (the LD power was kept constant). One other possibility is a decrease in the photovoltaic response when the LD beam is expanded; although some evidence in the literature suggests that this may be a possibility for optically controlled MESFETs [44], we have not attempted to incorporate this effect into our device model. In addition, the lack of a reverse-biased junction in the Si:CPW-PCS (there is a slight  $p^{++}/p$  junction due to the ion-implanted region) implies that this saturation effect is most likely not due to photovoltaic effects.

It is obvious from equation (4) that the saturation behavior is most likely not a circuit effect; if  $R_{on}$  tends to zero,  $S_{21}$  goes to minus infinity. Clearly, this is not indicative of a saturation effect, which would cause  $S_{21}$  to approach a constant value. However, the Si:CPW-PCS has a finite value of contact resistance  $R_c$ , which would limit the minimum of  $R_{on}$  to  $R_c$ ; thus  $S_{21}$  would approach a constant value in this case and the observed saturation effect would be expected. Although measurements on a curve-tracer indicate that  $R_c$  is negligible, more accurate measurements must be performed to determine the actual value. It is therefore believed that the observed saturation effect is due to a limiting of the minimum permissible on-state resistance, or conductance, by the finite Si:CPW-PCS  $R_c$ .

Using the same laser setup as figure 41 and performing an identical measurement to those described in the literature to measure the GaAs:CPW-PCS on-state resistance  $R_{on}$ , we measured the variation of  $S_{21}$  as a function of  $R_{on}$ . Figure 43 compares the measured value of  $S_{21}$  versus  $R_{on}$ , along with the theoretical prediction described in section 2.2 for the reflective attenuator scheme. Notice that the measured attenuation is approximately 5 dB greater than the predicted

**Figure 43. Theoretical and experimental comparison for reflective attenuation mechanism. Note that measured  $|S_{21}| >$  prediction  $\Rightarrow$  reflection mode may be incorrect.**



value over most of the range of  $R_{on}$ . Clearly, either the reflective attenuator model is in need of some refinement, or the absorptive attenuator scheme is valid.

Since we could not measure the reflected power accurately to determine which mode of operation is correct, a VNA was used to do the measurements (as will be described in sect. 5.4). If the reflective attenuator scheme is the correct interpretation of the optoelectronic attenuator results presented in this section, then as the optically induced attenuation increases, the power reflected from the optoelectronic attenuator should also increase by roughly an equivalent amount; use of a VNA to simultaneously measure  $|S_{21}|$  and  $|S_{11}|$  should indicate if this interpretation is correct.

#### 5.4 Fiber-Pigtailed LD Experiments—VNA Measurements

The limits of the rf transmission measurements described in the previous section can be summarized with two observations: first, the attenuator was designed to operate at 3 GHz, not 500 MHz, and, second, the reflected power from the Si:CPW-PCS has yet to be accurately measured as a function of LD power. Using a VNA [101] loaned to us by Anritsu/Wiltron, Inc., we have characterized the performance of the optoelectronic attenuator. These measurements show, once and for all, that the correct attenuation mechanism to describe the optoelectronic attenuator is absorptive (i.e., the optically induced solid-state plasma attenuates the propagating microwave signal).

Figures 44 and 45 show the VNA data taken with the experimental setup of the last section (fig. 41) where the rf source and oscilloscope have been replaced with ports 1 and 2 of the VNA, respectively. The

10 $\times$  microscope objective was again used to form a 10- $\mu\text{m}$  laser spot on a single gap of the Si:CPW-PCS, as described in section 5.3. The fiber-pigtailed LD was again used as the optical source, only this time it was operated in cw mode to permit VNA measurements to be made. The first measurements showed, for identical LD peak powers, that the measured pulsed rf voltage and cw microwave values of  $S_{21}$ , both measured at 500 MHz, were identical. In addition, a spectrum analyzer was used to measure the level of attenuation, with the result also in agreement with the pulsed and cw  $S_{21}$  values. For comparison, a plot of the measured attenuation versus incident LD power, at 500 MHz and measured with the VNA, is shown in figure 46. Again, the LD spot was expanded by the cylindrical lens, and the observed attenuation increased as before.

Note that the measured attenuation of figure 44 is greater in the microwave frequency range ( $f > 1$  GHz) than it was in the vhf range (500 MHz). Indeed, 20.1 dB of attenuation was measured at the design frequency of 3 GHz with the 10 $\times$  microscope objective. More importantly, the measured reflected power,  $|S_{11}|$ , actually improves (becomes more negative) as the LD power is increased, as

**Figure 44.** VNA optoelectronic attenuator data with fiber-pigtailed LD (cw mode). A spot = 10  $\mu\text{m}$   $\times$  10  $\mu\text{m}$ , LD power as indicated. Note:  $S_{21}$  comparable to pulsed oscilloscope data. Maximum  $|S_{21}|$  = 21.1 dB at 3 GHz.

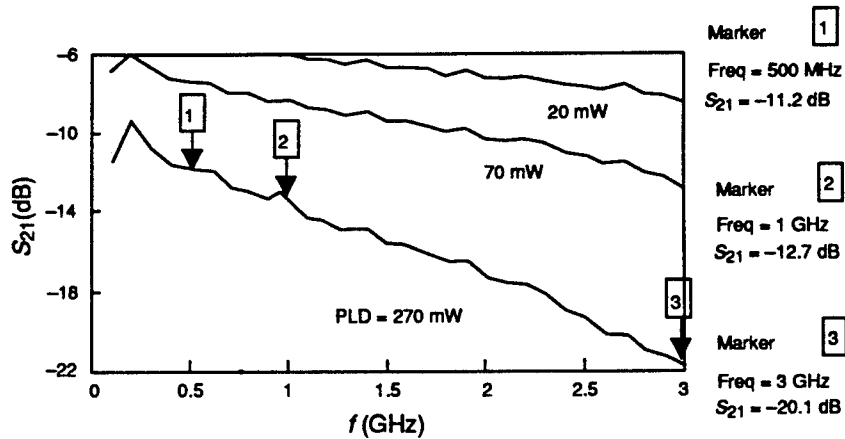
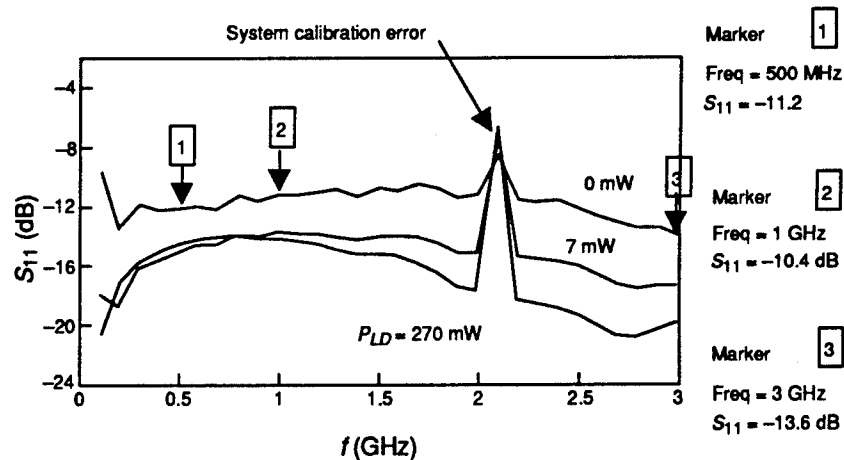


**Figure 45.** VNA optoelectronic attenuator data with fiber-pigtailed LD (cw mode). Measure of reflected power is  $S_{11}$ . Note:  $|S_{11}|$  = 10.4 dB at 1 GHz (dark value) and improves with increasing optical intensity. Spot size same as figure 40.



can be seen in figure 45. This tells us that the attenuation scheme is, in fact, absorptive, since an increase in the reflected power is not observed as the level of attenuation was increased.

As the beam was spread by the same cylindrical lens as before, two effects were observed. First, the attenuation, as with the rf voltage measurements made with the same laser in the pulsed mode, increased as the beam was expanded (see figs. 47 and 48). The second effect is that the attenuation becomes narrowband (i.e., peaks at a particular frequency), which is the expected result for an attenuation that is based on a plasma absorption mechanism [104,105]. This result occurs because the attenuation is maximum at the microwave frequency that is equal to the plasma frequency,  $\omega_p$ . Thus, we have a direct measure of  $\omega_p$  from our data. Since the peak in the absorption moves to lower frequencies as the LD power is increased (and hence the plasma density is increased), we can control the absorption level and maintain either a wideband attenuation characteristic or create a more narrowband response. It should be noted that a shift in the

**Figure 46.** VNA measured attenuation at 500 MHz versus incident LD power with fiber-pigtailed LD. Note:  $|S_{21}| = 10 \text{ dB}$  for  $10 \mu\text{m} \times 10 \mu\text{m}$  laser spot, and increases to 22 dB when spot is expanded to  $10 \mu\text{m} \times 3.5 \text{ mm}$ . Note data are similar to figure 41 and show that cw LD VNA measurement approximately equals pulsed LD rf voltage measurement.

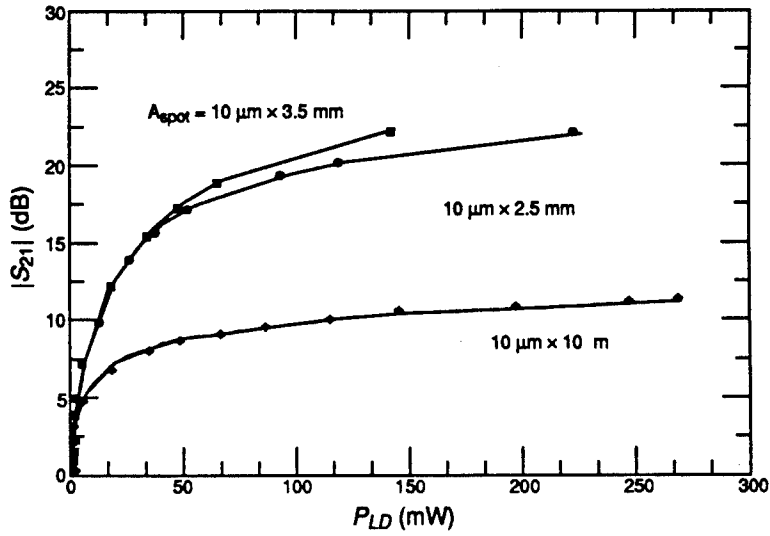
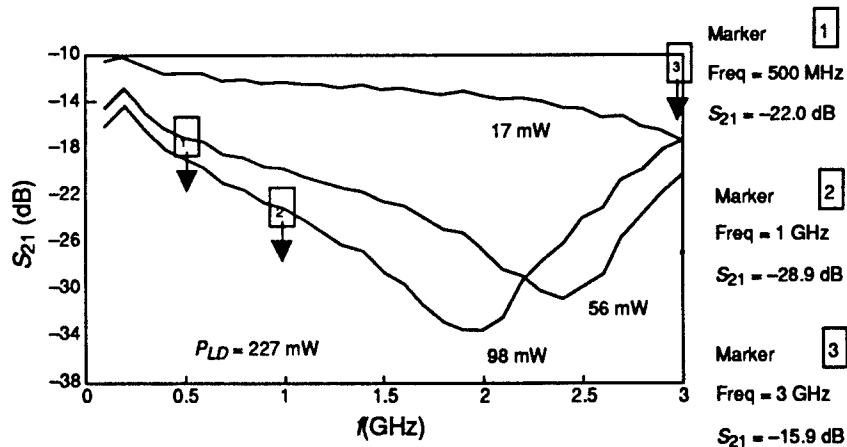


**Figure 47.** VNA optoelectronic attenuator data with fiber-pigtailed LD (cw mode).  $A_{\text{spot}} = 10 \mu\text{m} \times 2.5 \text{ mm}$ , LD power as indicated. Note:  $S_{21}$  has increased versus  $10 \times 10 \mu\text{m}$  spot. Maximum  $|S_{21}| = 28.9 \text{ dB}$  at 1 GHz.



absorption peak with plasma density is also expected [104,105] and is therefore not surprising.

In order to measure the maximum attenuation that could be achieved with the  $10 \mu\text{m} \times 3.5 \text{ mm}$  spot of figure 48, we increased the laser power to 143 mW and a peak attenuation of 45.6 dB was measured at 1.7 GHz (see fig. 49). These data show that we have truly demonstrated a very useful microwave control scheme during this research, especially since the attenuation is absorptive, so that matching schemes for limiting the deleterious effect of power reflections back to the source can be avoided.

What remains at this point is to rigorously model the VNA experimental results so that we can achieve a clear understanding of how the optoelectronic attenuator works. To date, only qualitative agreement with theory has been achieved (for example, see fig. 6); a more complete theoretical development is clearly required if the optoelectronic attenuator is to be improved and/or inserted into a microwave system.

**Figure 48.** VNA optoelectronic attenuator data with fiber-pigtailed LD (cw mode).  $A_{\text{spot}} = 10 \mu\text{m} \times 3.5 \text{ mm}$ , LD power as indicated. Note:  $|S_{21}|$  has increased further. Maximum  $|S_{21}| = 29.4 \text{ dB}$  at 1 GHz.

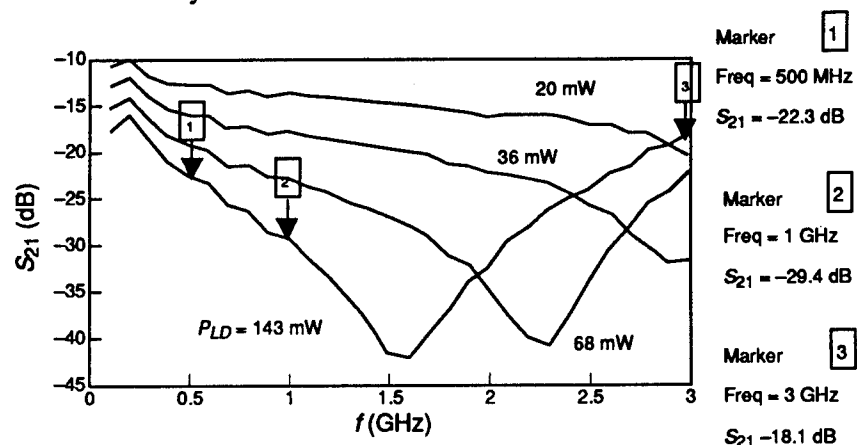
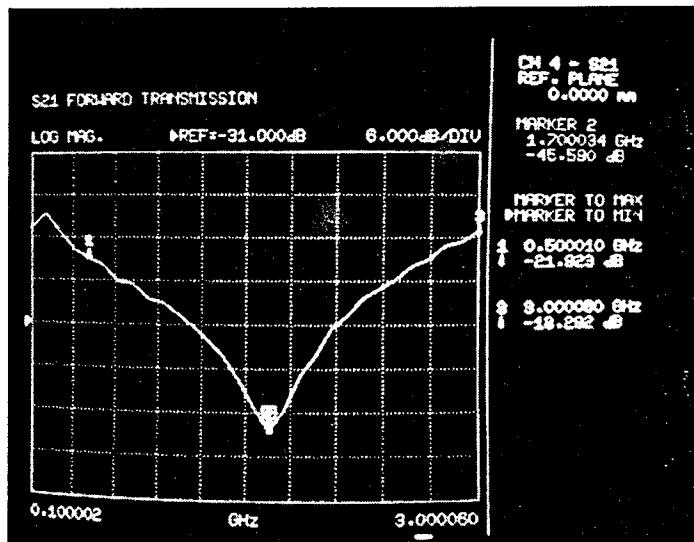


**Figure 49.** VNA optoelectronic attenuator data with fiber-pigtailed LD (cw mode).  $A_{\text{spot}} = 10 \mu\text{m} \times 3.5 \text{ mm}$ , LD power = 143 mW. Maximum  $|S_{21}| = 45.5 \text{ dB}$  at 1.7 GHz.



## 5.5 Summary

An optoelectronic technique suitable for the control of microwave integrated circuits has been demonstrated. Using a coplanar waveguide-photoconductive switch fabricated on silicon (Si:CPW-PCS), we have been able to vary the attenuation of microwave signals by up to 45 dB for a laser power of less than 150 mW. An observed saturation of the microwave attenuation, as a function of laser intensity, was observed. Proper LD beam profile matching, using optical beam expansion techniques, was successfully used to optimize the attenuator performance. In addition, a 300- $\mu$ m-stripe broad-area laser diode, fabricated in our laboratory and discussed by Saddow [91], was also used to successfully activate the attenuator; up to 10 dB of rf attenuation at 500 MHz was achieved.

Silicon was found to be the most suitable material for the optoelectronic attenuator because of its long PC carrier lifetime [49], which permits a PC gain [83] to be realized in this material, as described in section 4. For an all-GaAs-based optoelectronic attenuator, data in the literature [84,85] indicate that similar performance to the Si:CPW-PCS can be achieved with the GaAs:CPW-PCS by superlattice techniques.

## 6. Summary and Conclusions

During the course of this research project, most of the objectives were met. Attenuation levels exceeding 45 dB were achieved using less than 145 mW of power from a commercially available LD [102]; hence, an all-semiconductor optoelectronic attenuator that requires modest laser power levels has been successfully demonstrated. In section 1, two attenuation schemes are presented, along with estimates of their anticipated performance. High-speed PC switches, fabricated on both GaAs and Si, have been developed using a CPW contact geometry; suitable microwave performance has been achieved with these devices. The development of these high-speed CPW-PCSs is described in section 4, along with the relevant physics of such high-speed devices.

If the optoelectronic attenuator is to be realized, a suitable laser source must be developed; this laser must be a semiconductor device (i.e., laser diode) and must be triggerable in less than a nanosecond with picosecond timing jitter. This is a rather stringent design requirement, especially in light of the fact that considerable optical power is normally required for PC switching applications [94]. Consequently, in-depth research was performed to ensure that a suitable LD was available to meet the optoelectronic attenuator design requirements; Saddow [91] discusses the progress made in this area. In particular, we have achieved the highest reported broad-area LD output powers using an optical Q-switching scheme, where the LD output was increased to greater than 6 W from approximately 1 W, and the pulselwidth reduced from 100 ns to 60 ps. We have also used the optical Q-switching technique to better understand the LD dynamics so that further improvements can be made. Using a two-section broad-area LD, we demonstrated that such a device can be turned on in less than 500 ps; thus, subnanosecond operation of an optoelectronic attenuator seems feasible. Finally, the light output of a broad-area LD has been increased by greater than 37 percent using microwave matching techniques. Details of the LD development are given in section 3.

Since AlGaAs/GaAs LDs are to be used as the laser source, a detailed investigation of the interaction between a GaAs:CPW-PCS and the LD was performed [106]; a titanium sapphire (Ti:sapphire) laser was used to measure the PC switch performance as a function of laser photon energy. In order to improve the optoelectronic attenuator performance, the GaAs:CPW-PCS performance was simultaneously measured as a function of switch temperature and applied electric field. Our results show that an improvement of a factor of

three in the on-state resistance (and, conversely, conductance) can be achieved, for a fixed photon energy, by tuning the CPW-PCS temperature over a 20°C range. Comparable LD temperature tuning would cut this improvement factor in half. Details of this investigation are described in section 3.

Since the GaAs:CPW-PCS performance appeared to be poor due to the material's short (5 ns) PC carrier lifetime, the Si:CPW-PCS was used to set up the hybrid optoelectronic attenuator (the Si:CPW-PCS PC carrier lifetime was  $\approx 1 \mu\text{s}$ ). Optoelectronic attenuator experiments were performed in several ways; with pulsed optical illumination (measured on a 1 GHz bandwidth analog oscilloscope) to attenuate a 500-MHz rf waveform [97], and with cw illumination to attenuate cw waveforms from a VNA [102]. These experiments permitted us to finally assess the relevance of the two attenuation schemes presented in section 2; thus, the exact nature of the attenuation mechanism for such a device has been determined. These results are presented in section 5 where we see that the attenuator not only provides greater than 45 dB of microwave attenuation, but that this can be accomplished with less than 145 mW of optical power by properly matching the laser beam profile to the Si:CPW-PCS.

Although silicon is not the usual material of choice for MMICs due to lower carrier mobility and lack of semi-insulating behavior, considerable research and development has been conducted to develop silicon MMICs [107], especially at frequencies below X-band ( $\sim 10 \text{ GHz}$ ). In addition, superlattice structures can be employed in GaAs to increase the carrier lifetime into the microsecond regime [84]. Therefore, demonstration of a silicon-based optoelectronic attenuator is valid for MMIC applications; it can be directly used in silicon MMICs, and superlattices can be used to achieve similar performance in an all GaAs-based optoelectronic attenuators using a GaAs:CPW-PCS and AlGaAs/GaAs LD.

## Acknowledgements

The authors would first like to thank the High-Power Microwave Technology Management Office (HPM-TMO) for providing financial support for this research. In particular, we gratefully acknowledge the support of Dr. Roger Kaul and Louis J. Jasper, Jr., both of the RF Effects and Hardening Technology Branch, Army Research Laboratory. We thank Christopher Mermagen for his assistance in performing the laser diode matching work, and all of the members of the Ultrafast Optoelectronics Laboratory, University of Maryland, who were so helpful during the three plus years of this research.

## References

1. S. Jayaraman and C. H. Lee, "Observation of Two-Photon Conductivity in GaAs with Nanosecond and Picosecond Light Pulses," *Appl. Phys. Lett.* **20**, 392–394 (1972).
2. D. H. Auston, *Ultrashort Laser Pulses and Applications*, Springer-Verlag (1988).
3. C. H. Lee, "Picosecond Optics and Microwave Technology," *IEEE Trans. Microwave Theory Tech.* **38** (5), pp. 596–607 (May 1990).
4. N. B. Chaim, I. Ury, and A. Yariv, "Integrated Optoelectronics," *IEEE Spectrum* **19** (5), pp. 38–45 (May 1982).
5. S. R. Forrest, "Optical Detectors: Three Contenders," *IEEE Spectrum* **23**, (5), pp. 76–84 (May 1986).
6. R. A. Pucel (editor), *Monolithic Microwave Integrated Circuits*, IEEE Press, New York, NY (1985).
7. G. E. Brehm, "Multifunction MMIC History from a Process Technology Perspective," *IEEE Trans. Microwave Theory Tech.* **38** (9), pp. 1164–1170 (September 1990).
8. E. D. Cohen, "MMIC from the Department of Defense Perspective," *IEEE Trans. Microwave Theory Tech.* **38** (9), pp. 1171–1174 (September 1990).
9. P. R. Herczfeld (guest editor), *Special Issue on Applications of Lightwave Technology to Microwave Devices, Circuits, and Systems*, *IEEE Trans. Microwave Theory Tech.* **38** (5), special issue (May 1990).
10. R. N. Simons, *Optical Control of Microwave Devices*, Artech House, Boston, MA (1990), Chapter 1.
11. A. G. Stove, "Automobile Radar," *Appl. Microwave Magazine*, pp. 102–115, Spring 1993, and A. Kim, S. E. Saddow, R. Youmans, L. J. Jasper, M. Weiner, and C. H. Lee, "Photoconductive Monolithic Wideband Transmitter Characterization," *IEEE LEOS Summer Topicals: Optical-Microwave Interactions W1.4*, Conference Proceedings, Santa Barbara, CA (19 July 1993).
12. C. Y. Chen, A. Y. Cho, C. G. Bethea, P. A. Garbinski, Y. M. Pang, B. F. Levine, and K. Ogawa, "Ultrahigh Speed Modulation-Doped Heterostructure Field-Effect Photodetectors," *Appl. Phys. Lett.* **42** pp. 1040–1042 (June 1983).

13. T. Umeda, Y. Cho, and A. Shibatomi, "Picosecond HEMT Photodetector," *Japan J. Applied Physics* **25**, pp. L801–L803 (October 1986).
14. R. N. Simons, "Microwave Performance of an Optically Controlled AlGaAs/GaAs High Electron Mobility Transistor and GaAs MESFET," *IEEE Trans. Microwave Theory Tech.* **35** (12) (December 1987).
15. T. R. Chen, K. Utaka, Y. Zhuang, Y. Y. Liu, and A. Yariv, "A Vertical Monolithic Combination of an InGaAsP/InP Laser and a Heterostructure Bipolar Transistor," *IEEE J. Quantum Electron.* **23** (6) (June 1987).
16. A. Yariv, *Quantum Electronics*, Third Ed., John Wiley & Sons, New York, NY (1989).
17. I. Ury, K. Y. Lau, N. B. Chaim, and A. Yariv, "Very High Frequency GaAlAs Laser-Field Effect Transistor Monolithic-Integrated Circuit," *Appl. Phys. Lett.* **41** (2) (July 1982).
18. C. P. Lee, S. Margalit, I. Ury, and A. Yariv, "Integration of an Injection Laser with a Gunn Oscillator on a Semi-Insulating GaAs Substrate," *Appl. Phys. Lett.* **32** (12) (September 1987).
19. T. Sueta and M. Izutsu, "Integrated Optic Devices for Microwave Applications," *IEEE Trans. Microwave Theory Tech.* **38** (95), pp. 447–482 (May 1990).
20. K. Uomi, T. Mishima, and N. Chinone, "Ultrahigh Relaxation Oscillation Frequency (up to 30 GHz) of Highly p-doped GaAs/GaAlAs Multiple Quantum Well Lasers," *Appl. Phys. Lett.* **51** (2), pp. 78–80 (July 1987).
21. B. J. V. Zeghbroeck, W. Patrick, J. M. Halbout, and P. Vettinger, "105-GHz Bandwidth Metal-Semiconductor-Metal Photodiode," *IEEE Electron Dev. Lett.* **9**, (10), pp. 527–529 (October 1988).
22. R. G. Walker, "Broadband (6 GHz) GaAs/AlGaAs Electro-Optic Modulator with Low Drive Power," *Appl. Phys. Lett.* **54** (17), pp. 1613–1615 (April 1989).
23. S. Y. Yang, S. H. Lin, and Y. M. Houng, "GaAs Traveling-Wave Polarization Modulator with Bandwidth in Excess of 20 GHz at 1.3  $\mu$ m," *Appl. Phys. Lett.* **51** (2), pp. 83–85 (July 1987).
24. R. N. Simons, *Optical Control of Microwave Devices*, Artech House, Boston, MA, Chapter 5 (1990).

25. W. B. Scott, "Air Force Funding Joint Studies to Develop Smart Skin Avionics," *Aviation Week and Space Technology* 128 (16), pp. 65-69 (18 April 1988).
26. A. S. Daryoush, E. Ackerman, R. Saedi, R. Kunath, and K. Shalkhauser, "High-Speed Fiber-Optic Links for Distribution of Satellite Traffic," *IEEE Trans. Microwave Theory Tech.* 38 (5), pp. 510-517 (May 1990).
27. I. Bahl and P. Bhartia, *Microwave Solid State Circuit Design*, John Wiley & Sons, Inc., New York, NY, pp. 626-659 (1988) (see also ref. 85).
28. P. Bhartia and I. Bahl, *Millimeter Wave Engineering and Applications*, John Wiley & Sons, Inc., New York, NY, Chapter 1 (1984).
29. D. P. Neikirk, P. Cheung, M. S. Islam, and T. Itoh, "Optically-C Controlled Coplanar Waveguide Phase Shifters," *Microwave J.*, pp. 77-88 (December 1989).
30. J. L. Vorhaus et al, "Monolithic Dual-Gate FET Digital Phase Shifters," *IEEE Trans. Microwave Theory Tech.* 30, pp. 991-992 (1982).
31. I. Bahl and P. Bhartia, *Microwave Solid State Circuit Design*, John Wiley & Sons, Inc., New York, NY, pp. 604-625 (1988).
32. Hewlett-Packard, "An Attenuator Design Using p-i-n Diodes," Application Note No. 912.
33. Y. Tajima et al, "GaAs Monolithic Wideband (218 GHz) Variable Attenuators," *IEEE MTT-S Int. Microwave Symp. Digest*, pp. 479-481 (1982).
34. A. S. Daryoush, "Optical Synchronization of Millimeter-Wave Oscillators for Distributed Architectures," *IEEE Trans. Microwave Theory Tech.* 38, (5) (May 1990).
35. C. H. Lee, *Picosecond Optoelectronic Devices*, Academic Press, Inc., Chapter 5 (1984).
36. E. E. Funk, E. A. Chauchard, M. J. Rhee, and C. H. Lee, "80-kW Inductive Pulsed Power System with a Photoconductive Semiconductor Switch," *IEEE Photonics Technol. Lett.* 3 (6) (June 1991).
37. I. Bahl and P. Bhartia, *Microwave Solid State Circuit Design*, John Wiley & Sons, Inc., New York, NY, Chapter 12 (1988).
38. I. Bahl and P. Bhartia, *Microwave Solid State Circuit Design*, John Wiley & Sons, Inc., New York, NY, pp. 472-473 (1988).

39. E. A. Wolff and R. Kaul (eds), *Microwave Engineering and Systems Applications*, John Wiley & Sons, Inc., Chapter 6 (1988).
40. N. Weber, "New Reflection-Type Optoelectronic Microwave Switch for CW Applications," *IEEE Electron. Lett.* **26** (7), pp. 455–456.
41. E. A. Wolff and R. Kaul, *Microwave Engineering and Systems Applications*, John Wiley & Sons, Inc., Chapter 10 (1988).
42. L. M. Devlin, B. J. Buck, J. C. Clifton, A. W. Dean, and A. P. Long, "A 2.4 GHz Single Chip Transceiver," *IEEE Microwave and Millimeter-Wave Circuits Symp. Digest*, Atlanta, GA, pp. 23–26 (14–15 June 1993).
43. A. Kim, S. E. Sadow, R. Youmans, L. J. Jasper, M. Weiner, and C. H. Lee, "Photoconductive Monolithic Wideband Transmitter Characterization," *IEEE LEOS Summer Topicals: Optical-Microwave Interactions, W1.4*, Conference Proceedings, Santa Barbara, CA (19 July 1993).
44. A. Paoella, "Variations in the Gain and Bandwidth of the MESFET Photoresponse with Bias and Optical Intensity," *IEEE LEOS Summer Topicals: Optical-Microwave Interactions, M3.4*, Conference Proceedings, Santa Barbara, CA, pp. 25–26 (19 July 1993).
45. C. Hentschel, *Hewlett-Packard Fiber Optics Handbook*, Third Edition, Hewlett-Packard GmbH, Boeblingen Instruments Division, Germany, p. 24 (1989).
46. A. Yariv, *Quantum Electronics*, John Wiley & Sons, Inc., pp. 255–260 (1989).
47. S. H. Yang, B. J. Thedrez, S. E. Sadow, Y. Q. Liu, and C. H. Lee, "Experimental and Theoretical Investigation of Large Output Broad Area AlGaAs Semiconductor Laser Diodes," *IEEE Photonics Tech. Lett.* **5** (1), pp. 19–23 (January 1993).
48. S. Ramo, J. R. Whinnery, and T. van Duzer, *Fields and Waves in Communication Electronics*, John Wiley & Sons, Chapter 13 (1984).
49. R. S. Muller and T. I. Kamins, *Device Electronics for Integrated Circuits*, Second Edition, John Wiley & Sons, New York, NY, pp. 226–228 (1986).
50. J. D. Jackson, *Classical Electrodynamics*, John Wiley & Sons, Inc., New York, NY, Second Edition, Chapter 10 (1975).
51. S. M. Sze, *Physics of Semiconductor Devices*, John Wiley & Sons, Inc., New York, NY, Second Edition, p. 744–745 (1981).

52. M. A. Richardson, M. S. Mazzola, and S. Spence, "Design of Bulk Optically Controlled Semiconductor Switches for Microelectronic Applications," *IEEE International Conf. on Plasma Science ICOPS '93, Conf. Digest, Vancouver, B.C., Canada* 5C8, p. 195 (7–9 June 1993).
53. J. E. Bowers (guest editor), "Special Issue on Semiconductor Diode Lasers," *IEEE J. Quantum Electron.* 25 (6) (June 1989).
54. N. Moore and K. Y. Lau, "Ultrahigh Efficiency Microwave Signal Transmission Using Tandem-Contact Single Quantum Well GaAlAs Lasers," *Appl. Phys. Lett.* 55 (4) (September 1989).
55. Y. Arakawa, A. Larsson, J. Palaski, and A. Yariv, "Active Q-switching in a GaAs/AlGaAs Multiquantum Well Laser With an Intracavity Monolithic Loss Modulator," *Appl. Phys. Lett.* 48, pp. 561–563 (1986).
56. R. S. Tucker, "High-Speed Modulation of Semiconductor Lasers," (invited) *IEEE J. Lightwave Technol.* 3 (6) (December 1985).
57. B. J. Thedrez, S. E. Saddow, Y. Q. Liu and C. H. Lee, "Experimental and Theoretical Investigation of Large Output Broad Area AlGaAs Semiconductor Laser Diodes," *IEEE Photonics Tech. Lett.* 5 (1), pp. 19–23 (January 1993).
58. S. H. Yang, B. J. Thedrez, S. E. Saddow, Y. Q. Liu and C. H. Lee, "Cross-Correlation Measurement of the Turn-on Delay and Pulsewidth of a Q-switched Two-section Semiconductor Laser," *IEEE Photonics Tech. Lett.* 5 (12) (December 1993).
59. G. P. Agrawal and N. K. Dutta, *Long-Wavelength Semiconductor Lasers*, Van Nostrand Reinhold, New York, NY (1986).
60. H. C. Casey, Jr., and M. B. Panish, *Heterostructure Lasers*, Parts A and B, Academic Press, New York, NY (1978).
61. Y. Arakawa and A. Yariv, "Theory of Gain, Modulation Response, and Spectral Linewidth in AlGaAs Quantum Well Lasers," *IEEE J. Quantum Electron.* 21, pp. 1666–1674 (1985).
62. A. Paradisi and I. Montrosset, "Numerical Modeling of Bistable Laser Diodes with Saturable Absorbers," *IEEE J. Quantum Electron.* 27 (3), pp. 817–823 (1991).
63. B. J. Thedrez and C. H. Lee, "A Reassessment of Standard Rate Equations for Low Facet Reflectivity Semiconductor Lasers using Traveling Wave Rate Equations," *IEEE J. Quantum Electron.* 28 (12), pp. 2706–2713 (1992).

64. D. A. B. Miller, D. S. Chelma, T. C. Damen, A. C. Gossard, W. Wiegmann, T. H. Wood, and C. A. Burns, "Band-edge Electroabsorption in Quantum Well Structures: The Quantum Confined Stark Effect," *Phys. Rev. Lett.* **53**, pp. 2173–2176 (June 1984).
65. J. Berthold, A. F. J. Levi, T. Tanbun-Ek, R. A. Logan, and S. N. G. Chu, "Voltage-Controlled Q-switching in InGaAs/InP Single Quantum Well Lasers," *Appl. Phys. Lett.* **55** (19) (November 1989).
66. P. Vasil'ev, I. S. Goldobin, A. A. Didzhyul's, M. I. Efimchik, S. V. Efremov, B. I. Levitas, A. B. Sergeev, and E. V. Shatkovskii, "Formation of Electrical Pulses with a Rise Time Shorter Than 10 Ps by an Optoelectronic Switch Controlled by an Injection Laser," *Sov. Tech. Phys. Lett.* **14** (8) (1988).
67. P. Vasil'ev, "Picosecond Optoelectronics," *Sov. J. Quantum Electron.* **20** (3), pp. 209–227 (1990), and P. P. Vasil'ev, "Picosecond Injection Laser: A New Technique for Ultrafast Q-Switching," *IEEE J. Quantum Electron.* **24** (12) (December 1988).
68. J. O'Gorman, A. F. Levi, and W. S. Hobson, "High Power Switching of Multielectrode Broad Area Lasers," *Electron. Lett.* **27** (1), p. 13 (1991).
69. L. Yan, P. T. Ho, C. H. Lee, and G. L. Burdge, "Generation of Ultrashort Pulses from a Neodymium Glass Laser System," *IEEE J. Quantum Electron.* **25**, pp. 2431–2440 (1989).
70. A. F. Levi, J. O'Gorman, D. Dykaar, W. S. Hobson, T. Tanbun-Ek, and R. A. Logan, "Ultrashort Pulse Generation using Intracavity-Modulated Quantum-Well Lasers," Conf. on Lasers and Electro-Optics *CLEO '91*, CTuL1, Baltimore, MD (1991).
71. D. R. Dykaar, K. Berthold, A. F. J. Levi, T. Tanbun-Ek, and R. A. Logan, "Large-signal Picosecond Response of InGaAs/InP Quantum Well Lasers with an Intracavity Loss Modulator," *Appl. Phys. Lett.* **56**, pp. 1629–1631 (1990).
72. E. A. Wolff and R. Kaul, *Microwave Engineering and Systems Applications*, John Wiley & Sons, Inc., Chapter 5 (1988).
73. M. C. R. Carvalho and W. Margulis, "Laser Diode Pumping with a Transmission Line Transformer," *IEEE Microwave and Guided Wave Lett.* **1** (12) (1991).
74. M. C. R. Carvalho, W. Margulis, and J. R. Souza, "A New, Small-Sized Transmission Line Impedance Transformer, with Applications in High-Speed Optoelectronics," *IEEE Microwave and Guided Wave Lett.* **2** (11) (1992).

75. Academy® is a registered product of EEsorf, Inc.
76. Duroid 6010® is a registered trade name of Rogers Corp., Chandler, AZ.
77. N. G. Paulter, A. J. Gibbs, and D. N. Sinha, "Fabrication of High-Speed GaAs Photoconductive Pulse Generators and Sampling Gates by Ion Implantation," *IEEE Trans. on Electron Devices* 35 (12), pp. 2343–2348 (December 1988).
78. R. H. Bube, *Photoelectronic Properties of Semiconductors*, Cambridge University Press, Great Britain, Chapter 1 (1992).
79. E. A. Chauchard, C. C. Kung, C. H. Lee, M. J. Rhee, and V. Diadiuk, "A New Method to Generate Square Pulses: Optoelectronic Switching in a Current Charged Transmission Line," *IEEE Trans. Plasma Sci.* 15 (1) (February 1987).
80. G. M. Martin, A. Mitonneau, and A. Mircea, "Electron Traps in Bulk and Epitaxial GaAs Crystals," *Electronics Lett.* 13 (7), pp. 191–193 (March 1987).
81. R. A. Roush, D. C. Stoudt, and M. S. Mazzola, "Compensation of Shallow Silicon Donors by Deep Copper Acceptors in Gallium Arsenide," *Appl. Phys. Lett.* 62 (21), pp. 2670–2672 (24 May 1993).
82. H. A. Zarem et al, "Effect of Al Mole Fraction on Carrier Diffusion Lengths and Lifetimes in  $Al_xGa_{1-x}As$ ," *Appl. Phys. Lett.* 55 (25), pp. 2622–2624 (18 December 1989).
83. C. H. Lee, *Picosecond Optoelectronic Devices*, Academic Press, New York, NY, pp. 131–132 (1984).
84. R. K. Ahrenkiel, D. J. Dunlavy, B. Keyes, S. M. Vernon, T. M. Dixon, S. P. Tobin, K. L. Miller, and R. E. Hayes, "Ultralong Minority-Carrier Lifetime Epitaxial GaAs by Photon Recycling," *Appl. Phys. Lett.* 55 (11), pp. 1088–1090 (September 1989).
85. K. Seeger, *Semiconductor Physics: An Introduction*, Fourth Edition, Springer Series in Solid-State Sciences 40, Springer-Verlag, Berlin, pp. 416–424 (1988).
86. J. Rivera and T. Itoh, University of Texas Lab. Report 79-1 (August 1979). Also presented in *Microwave Engineering and Systems Applications*, by E. A. Wolff and R. Kaul, John Wiley & Sons, Inc., New York, NY, pp. 194–195 (1988).
87. T. Itoh (editor), *Planar Transmission Line Structures*, IEEE Press Books (1979).

88. I. Bahl and P. Bhartia, *Microwave Solid State Circuit Design*, John Wiley & Sons, New York, NY (1988), Chapter 2.
89. S. L. Huang, *On-Wafer Optoelectronic Techniques for MMIC Applications*, Ph.D. dissertation, University of Maryland (August 1993).
90. *EEsof Touchstone® User's Manual*, Pub. 1.4-01186 (January 1986).
91. S. E. Saddow, *Optical Control of Microwave Integrated Circuits using High-Speed Photoconductive Switches*, Ph.D. dissertation, University of Maryland, College Park, MD (December 1993).
92. S. M. Sze, *Physics of Semiconductor Devices*, John Wiley & Sons, Inc., New York, NY, second edition, p. 750 (1981).
93. L. West, T. C. Hasenberg, A. Kost, M. Matloubian, G. C. Valley, and J. O. White, "Modulation of Millimeter Waves by Optically Illuminating n-i-p-i Structures," *IEEE LEOS Summer Topicals: Optical-Microwave Interactions*, M4.4, Conference Proceedings, Santa Barbara, CA (19 July 1993).
94. A. Rosen, P. J. Stabile, D. W. Bechtle, W. Janton, A. M. Gombar, J. McShea, A. Rosenberg, P. R. Herczfeld, and A. Bahagadri, "Optically Achieved p-i-n Diode Switch Utilizing a Two-Dimensional Laser Array at 808 nm as an Optical Source, *IEEE Trans. Electron Devices* **26** (2), pp. 455–456 (February 1989).
95. A. J. Seeds and A.A.A. de Salles, "Optical Control of Microwave Semiconductor Devices," *IEEE Trans. Microwave Theory Tech.* **38** (5), pp. 577–585 (May 1990).
96. P. R. Herczfeld, A. S. Daryoush, A. Rosen, A. Sharma, and V. M. Contarino, "Indirect Subharmonic Optical Injection Locking of Millimeter Wave IMPATT Oscillator," *IEEE Trans. Microwave Theory Tech.* **34** (12), pp. 1371–1376 (December 1986).
97. S. E. Saddow, B. J. Thedrez, and C. H. Lee, "An Optoelectronic Attenuator for the Control of Microwave Circuits," *IEEE Microwave and Guided Wave Lett.* **3** (11), pp. 361–362 (October 1993).
98. W. Platte and B. Sauerer, "Optically CW-Induced Losses in Semiconductor Coplanar Waveguides," *IEEE Trans. Microwave Theory Tech.* **37** (1), pp. 139–149 (January 1989).
99. L. Yan, P. T. Ho, C. H. Lee, and G. L. Burdge, "Generation of Ultrashort Pulses from a Neodymium Glass Laser System," *IEEE J. Quantum Electron.* **25**, pp. 2431–2440 (1989).

100. Spectra Diode Labs No. SDL-2372-P3.
101. Wiltron Corp., *Model 360 Vector Network Analyzer*.
102. S. E. Saddow and C. H. Lee, "VNA Measurements on an Optoelectronic Attenuator for Microwave Circuit Control," *IEEE 1994 International Microwave Conference*, San Diego, CA, submitted for publication.
103. AVTECH Corp. Model AVL-2C High-Voltage Pulser.
104. A. M. Yurek, C. D. Striffler, and C. H. Lee, "Optoelectronic Devices for Millimeter Waves," in *Infrared and Millimeter Waves 14, Millimeter Components and Techniques*, K. J. Button, editor, Orlando, FL, Academic Press (1985).
105. A. M. Yurek, *Millimeter-Wave Technique for Characterizing the Behavior of Optically Induced Plasmas in Semiconductor Waveguides*, Ph.D. dissertation, University of Maryland (1984).
106. S. E. Saddow, B. J. Thedrez, S. L. Huang, T. J. Mermagen, and C. H. Lee, "An Investigation of the Temperature and Electric Field Dependence of a GaAs Microwave Photoconductive Switch," *SPIE-OE/LASE '93: Optically Activated Switching*, conference proceedings 1873-31, Los Angeles, CA (January 1993).
107. P. J. Stabile and A. Rosen, "A Silicon Technology for Millimeter-Wave Monolithic Circuits," *RCA Review* 45, pp. 587-605 (December 1984).

## Distribution

Admnstr Defns Techl Info Ctr Attn DTIC-DDA (2 copies) Cameron Sta Bldg 5 Alexandria VA 22304-6145	Ofc of the Assist Scy of the Army for Rsrch Dev & Acqstn (cont'd) Attn SARD-DOV LTC B Adams Rm 3E411 The Pentagon Washington DC 20310-0103
Advned Rsrch Proj Agcy Attn DSO B Hui 3701 N Fairfax Dr Arlington VA 22203	US Army ARDEC Attn SCMAR-FSP-M R T Kinasewitz Bldg 353N Picatinny Arsenal NJ 07806-5000
HQ Dfns Nuc Agcy Attn RAEE G Baker 6801 Telegraph Rd Alexandria VA 22310-3398	US Army CECOM Intllgnc/Elect Warfare Drctr Attn AMSEL-RD-IEW-SPO D Helm Vint Hill Farm Sta Warrenton VA 22186-5100
Ofc of the Secy of Defs Attn ODDRE/R & AT S Gontarek The Pentagon Washington DC 20301	Commandant US Army Infantry Schl Attn ATSH-CDM-E K Sines FT Benning GA 31905-5400
Army Matl Comnd Attn AMCRD-AR J Aveta Attn AMCDE-PQI J Kreck 5001 Eisenhower Ave Alexandria VA 22333-0001	US Army Mis Cmnd Attn AMSMI-RD-WS-UB D Holder Redstone Arsenal AL 35898-8000
Belvoir Rsrch Dev & Engrg Ctr Attn STRBE-NA S Schaedel FT Belvoir VA 22060-5606	US Army Prgm Mgr—Firefinder Attn SFAE-IEW-FF A Dirienzo FT Monmouth NJ 07703-5305
HQ, Dept of the Army Dep Chf of Staf Oprs & Plns Attn DAMO-FDI LTC R Morton Room 2C536 The Pentagon Washington DC 20310-0460	US Army Rsrch Lab Attn AMSRL-WT D Hisley Attn AMSRL-WT-PC A Barrows Aberdeen Proving Ground MD 21005-5066
Hdqtr US Army Cmmctn-Elect Cmnd RD&E Ctr Night Vsn & Elect Sensors Dirctr Attn AMSEL-RD-NV-ADS M Kovach FT Monmouth NJ 07703-5206	US Army Sp & Strtgc Dfse Comnd Attn CSSD-SL-S R Berg PO Box 1500 Huntsville AL 35807-3801
Ofc of the Assist Scy of the Army for Rsrch Dev & Acqstn Attn SARD-TT F Milton Rm 3E479 Attn SARD-TT C Nash Rm 3E479	Commander US Army TRADOC Attn ATCD-T J M Gray FT Monroe VA 23651

## Distribution

Nvl Rsrch Lab Attn Code 4650 T Wieting 4555 Overlook Avenue SW Washington DC 20375-5000	Mississippi State Univ Attn M Mazzola PO Drawer EE Mississippi State MS 39762
Sp & Nav Warfare Systs Comnd Attn SPAWAR 332 J Albertine 2451 Crystal Park Arlington VA 22245-5200	Univ of Maryland Electrcl Engrg Dept Attn C H Lee (10 copies) College Park MD 20742
Air Force Phillips Lab Attn PL/WSH H Dogliani Attn PL/WSM M Harrison Attn PL/WSH S Mason Attn PL/WSH W Snyder 3550 Aberdeen Ave SE Albuquerque NM 87109	Ball Systems Engrg Div Attn J E Vanderstar 2901 Juan Tabo NE Albuquerque NM 87124
Dept of the Air Force Attn AWP W Baker Attn PL/XPW P. Vail Kirtland NM 87117-6008	Consultant Attn V Van Lint 1032 Skylark Dr La Jolla CA 92037
Air Force Rome Air Dev Ctr Attn ERPT T Pesta Attn RADC J Rooks Griffiss AFB NY 13441	GE-CRD Attn M Ghezzo PO Box 8 Bldg KW RM B1309 Schenectady NY 12301
Commander Wright Rsrch Dev Ctr Attn WRDC/ELM T Kemerley Bldg 620 Area B Wright Patterson AFB OH 45433-7408	Jaycor Attn W Crevier 3944 State Stret Ste 360 Santa Barbara CA 93105
Los Alamos Natl Lab Attn K Callahan MS H851 Attn R Reinovsky PO Box 1663 Los Alamos NM 87545	Mssn Rsrch Corp Attn M Bollen Attn J McAdoo 8560 Cinderbed Rd Newington VA 22122
Sandia Natl Lab Attn Div 1248 L Bacon Attn Div 1235 J Hoffman PO Box 5800 Albuquerque NM 87185-5800	SPARTA Inc Attn R O'Connor 4901 Corporate Dr Ste 102 Huntsville AL 35805-6201
	SRI Intrntl Attn G August 333 Ravenswood Ave Menlo Park CA 94025

## Distribution

Westinghouse Electr Corp Elect Sys

Grp/BWI fcilty

Attn S Patel Mail Stop 3716

PO Box 1693

Baltimore MD 21203

Director

US Army Rsrch Lab

Attn AMSRL-WT I May

Aberdeen Proving Ground MD 21005-5000

US Army Rsrch Lab

Attn AMSRL-CP-PW L Weinberger

Attn AMSRL-CP-PW T White

Attn AMSRL-D-C Lgl Ofc

Attn AMSRL-DD-M J Scully

Attn AMSRL-DD-SE J Sczepanski

Attn AMSRL-OP-SD-TA Mail & Records

Mgmt

Attn AMSRL-OP-SD-TL Tech Library

(3 copies)

Attn AMSRL-OP-SD-TP Tech Pub

Attn AMSRL-SL-NB J Beilfuss

Attn AMSRL-SS J Sattler

Attn AMSRL-SS-SG J McCorkle

Attn AMSRL-WT-L G Roffman

US Army Rsrch Lab (cont'd)

Attn AMSRL-WT-NA H Brisker

Attn AMSRL-WT-NA R A Kehs

Attn AMSRL-WT-NB J Gwaltney

Attn AMSRL-WT-NF C Fazi

Attn AMSRL-WT-NF E Scannell

Attn AMSRL-WT-NF G Tran

Attn AMSRL-WT-NF J Tatum

Attn AMSRL-WT-NF L Jasper

Attn AMSRL-WT-NF M Berry

Attn AMSRL-WT-NF R Kaul

Attn AMSRL-WT-NF R Tan

Attn AMSRL-WT-NF S Kaplan

Attn AMSRL-WT-NF S Saddow

(20 copies)

Attn AMSRL-WT-NF T Turner

Attn AMSRL-WT-NG A Bromborsky

Attn AMSRL-WT-NH A Mark

Attn AMSRL-WT-NH G Huttlin

Attn AMSRL-WT-NH J Corrigan

Attn AMSRL-WT-NH L Libelo

Attn AMSRL-WT-NH S Hayes

Attn AMSRL-WT-NH T Bock

Attn AMSRL-WT-NH C Schlesiger